

Jordan Journal of P H Y S I C S

An International Peer-Reviewed Research Journal

Volume 10, No. 1, April 2017, Shaban 1438 H

Jordan Journal of Physics (JJP): An International Peer-Reviewed Research Journal funded by the Scientific Research Support Fund, Ministry of Higher Education and Scientific Research, Jordan, and published biannually by the Deanship of Research and Graduate Studies, Yarmouk University, Irbid, Jordan.

EDITOR-IN-CHIEF:

Ibrahim O. Abu Al-Jarayesh

Department of Physics, Yarmouk University, Irbid, Jordan.

ijaraysh@yu.edu.jo

EDITORIAL BOARD:

Dia-Eddin M. Arafah

President, AL- al Bait University, Mafrqa, Jordan.

darafah@ju.edu.jo

Nabil Y. Ayoub

President, American University of Madaba, Madaba, Jordan.

nabil.ayoub@gju.edu.jo

Jamil M. Khalifeh

Department of Physics, University of Jordan, Amman, Jordan.

jkalifa@ju.edu.jo

Sami H. Mahmood

Department of Physics, University of Jordan, Amman, Jordan.

s.mahmood@ju.edu.jo

Marwan S. Mousa

Department of Physics, Mu'tah University, Al-Karak, Jordan.

mmousa@mutah.edu.jo

Akram A. Rousan

Department of Applied Physical Sciences, Jordan University Of Science and Technology, Irbid, Jordan.

akram@just.edu.jo

Mohammad Al-Sugheir

Department of Physics, The Hashemite University, Zarqa, Jordan.

msugh@hu.edu.jo

EDITORIAL SECRETARY: Majdi Al-Shannaq.

Manuscripts should be submitted to:

Prof. Ibrahim O. Abu Al-Jarayesh
Editor-in-Chief, Jordan Journal of Physics
Deanship of Research and Graduate Studies
Yarmouk University-Irbid-Jordan
Tel. 00 962 2 7211111 Ext. 2075
E-mail: jjp@yu.edu.jo
Website: <http://Journals.yu.edu.jo/jjp>

Jordan Journal of PHYSICS

An International Peer-Reviewed Research Journal

Volume 10, No. 1, April 2017, Shaban 1438 H

INTERNATIONAL ADVISORY BOARD

Prof. Dr. Ahmad Saleh

Department of Physics, Yarmouk University, Irbid, Jordan.
salema@yu.edu.jo

Prof. Dr. Aurore Savoy-Navarro

LPNHE Université de Paris 6/IN2P3-CNRS, Tour 33, RdC 4,
Place Jussieu, F 75252, Paris Cedex 05, France.
auore@lfnhep.in2p3.fr

Prof. Dr. Bernard Barbara

Laboratoire Louis Neel, Salle/Room: D 108, 25, Avenue des
Martyrs BP 166, 38042-Grenoble Cedex 9, France.
Barbara@grenoble.cnrs.fr

Prof. Dr. Bruno Guiderdoni

Observatoire Astronomique de Lyon, g, avenue Ch. Antre-F-69561,
Saint Genis Laval Cedex, France.
Bruno.guiderdoni@olos.univ-lyon1.fr

Prof. Dr. Buford Price

Physics Department, University of California, Berkeley, CA 94720,
U. S. A.
bprice@berkeley.edu

Prof. Dr. Colin Cough

School of Physics and Astronomy, University of Birmingham, B15
2TT, U. K.
c.gough@bham.ac.uk

Prof. Dr. Desmond Cook

Department of Physics, Condensed Matter and Materials Physics
Research Group, Old Dominion University, Norfolk, Virginia
23529, U. S. A.
Dcook@physics.odu.edu

Prof. Dr. Evgeny Sheshin

MIPT, Institutskij per. 9, Dogoprudnyi 141700, Russia.
sheshin@lafaet.mipt.ru

Prof. Dr. Hans Ott

Laboratorium Fuer Festkorperphysik, ETH Honggerberg, CH-
8093 Zurich, Switzerland.
ott@solid.phys.ethz.ch

Prof. Dr. Herwig Schopper

President SESAME Council, Chairman Scientific Board UNESCO
IBSP Programme, CERN, 1211 Geneva, Switzerland.
Herwig.Schopper@cern.ch

Prof. Dr. Humam Ghassib

Department of Physics, The University of Jordan, Amman 11942,
Jordan.
humamg@ju.edu.jo

Prof. Dr. Ingo Hofmann

GSI Darmstadt, Planckstr. 1, 64291, Darmstadt, Germany.
i.hofmann@gsi.de

Prof. Dr. Jozef Lipka

Department of Nuclear Physics and Technology, Slovak University
of Technology, Bratislava, Ilkovicova 3, 812 19 Bratislava,
Slovakia.
Lipka@elf.stuba.sk

Prof. Dr. Khalid Touqan

Chairman of Jordan Atomic Energy Commission, Amman, Jordan.

Prof. Dr. Mark J. Hagmann

Desert Electronics Research Corporation, 762 Lacey Way, North
Salt Lake 84064, Utah, U. S. A.
MHagmann@NewPathResearch.Com

Prof. Dr. Nasr Zubeidey

President: Al-Zaytoonah University of Jordan, Amman, Jordan.
President@alzaytoonah.edu.jo

Prof. Dr. Patrick Roudeau

Laboratoire de l'Accelérateur, Lineaire (LAL), Université Paris-
Sud 11, Batiment 200, 91898 Orsay Cedex, France.
roudeau@mail.cern.ch

Prof. Dr. Paul Chu

Department of Physics, University of Houston, Houston, Texas
77204-5005, U. S. A.
Ching-Wu.Chu@mail.uh.edu

Prof. Dr. Peter Dowben

Nebraska Center for Materials and Nanoscience, Department of
Physics and Astronomy, 255 Behlen Laboratory (10th and R
Streets), 116 Brace Lab., P. O. Box 880111, Lincoln, NE 68588-
0111, U. S. A.
pdowben@unl.edu

Prof. Dr. Peter Mulser

Institute fuer Physik, T.U. Darmstadt, Hochschulstr. 4a, 64289
Darmstadt, Germany.
Peter.mulser@physik.tu-darmstadt.de

Prof. Dr. Rasheed Azzam

Department of Electrical Engineering, University of New Orleans
New Orleans, Louisiana 70148, U. S. A.
razzam@uno.edu

Dr. Richard G. Forbes

University of Surrey, FEPS (X1), Guildford, Surrey GU2 7XH,
U. K.
R.Forbes@surrey.ac.uk

Prof. Dr. Roy Chantrell

Physics Department, York University, York, YO10 5DD, U. K.
Rc502@york.ac.uk

Prof. Dr. Shawqi Al-Dallal

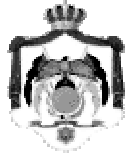
Department of Physics, Faculty of Science, University of Bahrain,
Manamah, Kingdom of Bahrain.

Prof. Dr. Susamu Taketomi

Matsumoto Yushi-Seiyaku Co. Ltd., Shibukawa-Cho, Yao City,
Osaka 581-0075, Japan.
taketomi@hotmail.com

Prof. Dr. Wolfgang Nolting

Institute of Physics / Chair: Solid State Theory, Humboldt-
University at Berlin, Newtonstr. 15 D-12489 Berlin, Germany
Wolfgang.nolting@physik.hu-berlin.de



The Hashemite Kingdom of Jordan



Yarmouk University

Jordan Journal of
PHYSICS

An International Peer-Reviewed Research Journal
Funded by the Scientific Research Support Fund

Volume 10, No. 1, April 2017, Shaban 1438 H

Instructions to Authors

Instructions to authors concerning manuscript organization and format apply to hardcopy submission by mail, and also to electronic online submission via the Journal homepage website (<http://jjp.yu.edu.jo>).

Manuscript Submission

1- **E-mail to :** jjp@yu.edu.jo

2- **Online:** Follow the instructions at the journal homepage website.

Original *Research Articles*, *Communications* and *Technical Notes* are subject to critical review by minimum of two competent referees. Authors are encouraged to suggest names of competent reviewers. *Feature Articles* in active Physics research fields, in which the author's own contribution and its relationship to other work in the field constitute the main body of the article, appear as a result of an invitation from the Editorial Board, and will be so designated. The author of a *Feature Article* will be asked to provide a clear, concise and critical status report of the field as an introduction to the article. *Review Articles* on active and rapidly changing Physics research fields will also be published. Authors of *Review Articles* are encouraged to submit two-page proposals to the Editor-in-Chief for approval. Manuscripts submitted in *Arabic* should be accompanied by an Abstract and Keywords in English.

Organization of the Manuscript

Manuscripts should be typed double spaced on one side of A4 sheets (21.6 x 27.9 cm) with 3.71 cm margins, using Microsoft Word 2000 or a later version thereof. The author should adhere to the following order of presentation: Article Title, Author(s), Full Address and E-mail, Abstract, PACS and Keywords, Main Text, Acknowledgment. Only the first letters of words in the Title, Headings and Subheadings are capitalized. Headings should be in **bold** while subheadings in *italic* fonts.

Title Page: Includes the title of the article, authors' first names, middle initials and surnames and affiliations. The affiliation should comprise the department, institution (university or company), city, zip code and state and should be typed as a footnote to the author's name. The name and complete mailing address, telephone and fax numbers, and e-mail address of the author responsible for correspondence (designated with an asterisk) should also be included for official use. The title should be carefully, concisely and clearly constructed to highlight the emphasis and content of the manuscript, which is very important for information retrieval.

Abstract: A one paragraph abstract not exceeding 200 words is required, which should be arranged to highlight the purpose, methods used, results and major findings.

Keywords: A list of 4-6 keywords, which expresses the precise content of the manuscript for indexing purposes, should follow the abstract.

PACS: Authors should supply one or more relevant PACS-2006 classification codes, (available at <http://www.aip.org/pacs/pacs06/pacs06-toc.html>)

Introduction: Should present the purpose of the submitted work and its relationship to earlier work in the field, but it should not be an extensive review of the literature (e.g., should not exceed 1 ½ typed pages).

Experimental Methods: Should be sufficiently informative to allow competent reproduction of the experimental procedures presented; yet concise enough not to be repetitive of earlier published procedures.

Results: should present the results clearly and concisely.

Discussion: Should be concise and focus on the interpretation of the results.

Conclusion: Should be a brief account of the major findings of the study not exceeding one typed page.

Acknowledgments: Including those for grant and financial support if any, should be typed in one paragraph directly preceding the References.

References: References should be typed double spaced and numbered sequentially in the order in which they are cited in the text. References should be cited in the text by the appropriate Arabic numerals, enclosed in square brackets. Titles of journals are abbreviated according to list of scientific periodicals. The style and punctuation should conform to the following examples:

1. Journal Article:

- a) Heisenberg, W., Z. Phys. 49 (1928) 619.
- b) Bednorz, J. G. and Müller, K. A., Z. Phys. B64 (1986) 189
- c) Bardeen, J., Cooper, L.N. and Schrieffer, J. R., Phys. Rev. 106 (1957) 162.
- d) Asad, J. H., Hijjawi, R. S., Sakaji, A. and Khalifeh, J. M., Int. J. Theor. Phys. 44(4) (2005), 3977.

2. Books with Authors, but no Editors:

- a) Kittel, C., "Introduction to Solid State Physics", 8th Ed. (John Wiley and Sons, New York, 2005), chapter 16.
- b) Chikazumi, S., C. D. Graham, JR, "Physics of Ferromagnetism", 2nd Ed. (Oxford University Press, Oxford, 1997).

3. Books with Authors and Editors:

- a) Allen, P. B. "Dynamical Properties of Solids", Ed. (1), G. K. Horton and A. A. Maradudin (North-Holland, Amsterdam, 1980), p137.
- b) Chantrell, R. W. and O'Grady, K., "Magnetic Properties of Fine Particles" Eds. J. L. Dormann and D. Fiorani (North-Holland, Amsterdam, 1992), p103.

4. Technical Report:

Purcell, J. "The Superconducting Magnet System for the 12-Foot Bubble Chamber", report ANL/HEP6813, Argonne Natl. Lab., Argonne, III, (1968).

5. Patent:

Bigham, C. B., Schneider, H. R., US patent 3 925 676 (1975).

6. Thesis:

Mahmood, S. H., Ph.D. Thesis, Michigan State University, (1986), USA (Unpublished).

7. Conference or Symposium Proceedings:

Blandin, A. and Lederer, P. Proc. Intern. Conf. on Magnetism, Nottingham (1964), P.71.

8. Internet Source:

Should include authors' names (if any), title, internet website, URL, and date of access.

9. Prepublication online articles (already accepted for publication):

Should include authors' names (if any), title of digital database, database website, URL, and date of access.

For other types of referenced works, provide sufficient information to enable readers to access them.

Tables: Tables should be numbered with Arabic numerals and referred to by number in the Text (e.g., Table 1). Each table should be typed on a separate page with the legend above the table, while explanatory footnotes, which are indicated by superscript lowercase letters, should be typed below the table.

Illustrations: Figures, drawings, diagrams, charts and photographs are to be numbered in a consecutive series of Arabic numerals in the order in which they are cited in the text. Computer-generated illustrations and good-quality digital photographic prints are accepted. They should be black and white originals (not photocopies) provided on separate pages and identified with their corresponding numbers. Actual size graphics should be provided, which need no further manipulation, with lettering (Arial or Helvetica) not smaller than 8 points, lines no thinner than 0.5 point, and each of uniform density. All colors should be removed from graphics except for those graphics to be considered for publication in color. If graphics are to be submitted digitally, they should conform to the following minimum resolution requirements: 1200 dpi for black and white line art, 600 dpi for grayscale art, and 300 dpi for color art. All graphic files must be saved as TIFF images, and all illustrations must be submitted in the actual size at which they should appear in the journal. Note that good quality hardcopy original illustrations are required for both online and mail submissions of manuscripts.

Text Footnotes: The use of text footnotes is to be avoided. When their use is absolutely necessary, they should be typed at the bottom of the page to which they refer, and should be cited in the text by a superscript asterisk or multiples thereof. Place a line above the footnote, so that it is set off from the text.

Supplementary Material: Authors are encouraged to provide all supplementary materials that may facilitate the review process, including any detailed mathematical derivations that may not appear in whole in the manuscript.

Revised Manuscript and Computer Disks

Following the acceptance of a manuscript for publication and the incorporation of all required revisions, authors should submit an original and one more copy of the final disk containing the complete manuscript typed double spaced in Microsoft Word for Windows 2000 or a later version thereof. All graphic files must be saved as PDF, JPG, or TIFF images.

Allen, P.B., “.....”, in: Horton, G.K., and Muradudin, A. A., (eds.), “Dynamical.....”, (North.....), pp....

Reprints

Twenty (20) reprints free of charge are provided to the corresponding author. For orders of more reprints, a reprint order form and prices will be sent with the article proofs, which should be returned directly to the Editor for processing.

Copyright

Submission is an admission by the authors that the manuscript has neither been previously published nor is being considered for publication elsewhere. A statement transferring copyright from the authors to Yarmouk University is required before the manuscript can be accepted for publication. The necessary form for such transfer is supplied by the Editor-in-Chief. Reproduction of any part of the contents of a published work is forbidden without a written permission by the Editor-in-Chief.

Disclaimer

Opinions expressed in this Journal are those of the authors and neither necessarily reflects the opinions of the Editorial Board or the University, nor the policy of the Higher Scientific Research Committee or the Ministry of Higher Education and Scientific Research. The publisher shoulders no responsibility or liability whatsoever for the use or misuse of the information published by JJP.

Indexing

JJP is currently indexing in:

- 1- **Emerging Sources Citation Index (ESCI)**



.

Jordan Journal of
P H Y S I C S

An International Peer-Reviewed Research Journal

Volume 10, No. 1, April 2017, Shaban 1438 H

Table of Contents:

English Articles	Pages
Calculation of Neutron Fluxes and Radiation Doses for Neutron Irradiator ^{226}Ra-Be Using the MCNP5 Code A. AlTaani, M. Nahili and A. Bitar	1-10
Analytic Approximate Solution of Blasius Equation Using Homotopy Perturbation Method (HPM) Hamza Berrehal and Abdelaziz Maougal	11-16
Free Breathing Abdominal Imaging with Fat-Water Separation Using 3D Radial Stack-of-Stars Trajectory Riad S. Ababneh	17-22
Assessment of Natural Radioactive Concentration Levels in the Oil Drilling Wells in Erbil Governorate Blocks Ahmed I. Samad, Ali H. Ahmed and Saman K. Ezzulddin	23-32
Optical and Structural Characterization of Dip Synthesized Al-B Co-doped ZnO Seeded Platforms for ZnO Nanostructures A. A. Ahmad, A. M. Alsaad, Q. M. Al-Bataineh, A. A. Bani-Salameh, H. M. Al-Khateeb and M. A. Al-Naafa	33-48
Size-Fractionated Number and Mass Concentrations in the Urban Background Atmosphere during Spring 2014 in Amman – Jordan Tareq Hussein and Ala'a Betar	49-58

Jordan Journal of Physics

ARTICLE

Calculation of Neutron Fluxes and Radiation Doses for Neutron Irradiator ^{226}Ra -Be Using the MCNP5 Code

A. AlTaani^a, M. Nahili^a and A. Bitar^b

^a Department of Physics, Faculty of Sciences, University of Damascus, Damascus, Syria.

^b Atomic Energy Commission, Damascus, Syria.

Received on: 20/7/2016;

Accepted on: 27/11/2016

Abstract: The irradiator ^{226}Ra -Be unit available at the Physics Department of the Sciences Faculty, Damascus University, was simulated by using the MCNP code. Calculations of neutron fluxes and radiation doses were carried out.

Simulation results showed that neutron fluxes, in the energy ranges: thermal (10^{-9} - 10^{-6} MeV), fast (0.11-12.0 MeV) and medium (10^{-5} - 10^{-1} MeV), had approximately the same magnitudes in some channels (See text for the definition of these channels), where the flux percent was about (thermal 70.0%, fast 18.0 % and medium 12.0%). On the other hand, the flux percent in one particular channel was about (thermal 40.0%, fast 39.0% and medium 21.0%) and in another one (thermal %60.0, fast %26.0 and medium %14.0) with the presence of a plate of Cadmium whose thickness is 2 mm.

Absorbed radiation doses, in two channels, were calculated by using MCNP5 code and then compared with those measured experimentally by using thermoluminescent dosimeters (TLD). A satisfactory agreement between calculated and measured results was found. The relative differences were about 3.8% and 7.2% in these two channels, respectively.

Keywords: Neutron irradiator, ^{226}Ra -Be, Thermoluminescent dosimeter, MCNP5 code.

Introduction

Neutron irradiation following $^9\text{Be}(\alpha, n)^{12}\text{C}$ reaction ($Q=5.7\text{MeV}$) is the most commonly used irradiation, as it gives the highest neutron yield. For many years, Radium 226, with its decay products, has been used as an alpha emitter when long-lived sources are needed. More recently, the availability of isotopes, such as ^{239}Pu , ^{227}Ac and ^{241}Am , has made it possible to produce neutron sources which have certain advantages, in particular a less intense gamma emission [1].

Radium 226 was the first alpha emitter used, because it was well studied as a radioactive source and it was relatively plentiful compared with other high energy alpha emitting isotopes. Polonium-210, which itself is a decay product of ^{226}Ra , was also used as an isotope in early neutron sources. Another early radioactive

material used in isotopic neutron sources was Actinium 227 (^{227}Ac), but because of its relative scarcity, this source was rarely used.

It was found that beryllium gave the best neutron yield of light elements; therefore, nearly all isotopic neutron sources after the 1950s were a combination of an alpha emitter and beryllium. However, some isotopic neutron sources used fluorine, boron or lithium instead of beryllium [2].

Neutron sources have been used in many areas, including research as well as nuclear and military industries, but the political situation and security concerns in recent years have led to the pursuit of reducing the use of neutron sources. Isotopic neutron sources have been replaced by sources of the type (d, t) and accelerators as sources of neutrons, but in spite of the benefits

of neutron sources of these two types, they are disadvantageous compared with isotopic neutron sources which give high-energy neutrons, in addition to large-scale electrical energy needed to operate neutron sources of the two mentioned neutron source types [1].

The aim of this work is to calculate the neutron fluxes in the channels of ^{226}Ra -Be irradiator unit by using MCNP5 code, as well as to calculate the radiation doses in channels 5 and 12 and compare the resulting values with the values measured by using a thermoluminescent dosimeter.

Materials and Methods

Description of ^{226}Ra -Be Irradiator Unit

The ^{226}Ra -Be irradiator unit (PHYWE-Bedienungsanleitung-neutronenquelle 3.5 mCi-09080.01) is available at the Physics Department

of the Sciences Faculty, Damascus University. It consists of:

The Container: It is made of steel (thickness = 4mm) in the form of a parallelepiped of dimensions $50\times 50\times 60\text{cm}^3$ and covered with a rectangular steel cover. The container contains a moderator of paraffin (density = 0.904 g/cm^3). There are ten cylindrical channels for irradiation (for each channel: thickness = 1mm, diameter = 2.2 cm). There is also a gap to insert a Cadmium plate, which is used as an absorber of thermal neutrons.

Five channels (4,5,6,7,8) are distributed on the circumference of a circle of 10 cm radius around the source (^{226}Ra -Be). The other five channels are located differently away from the source at 15 cm (channel 9), 20 cm (channels 11 and 12) and 25 cm (channels 10 and 13), as shown in Table 1 and Fig. 1 [3].

TABLE 1. Some general properties of ^{226}Ra -Be neutron irradiator

Name	Shape	Dimensions	Notices
Steel container	Cubic	$60\times 70\times 50\text{ cm}^3$	Contains paraffin moderator
Cadmium	Plate	$40\times 10\times 0.2\text{ cm}^3$	On axis Ox
^{226}Ra -Be source	Cylindrical tube	$7\times 2\text{ cm}^2$	-

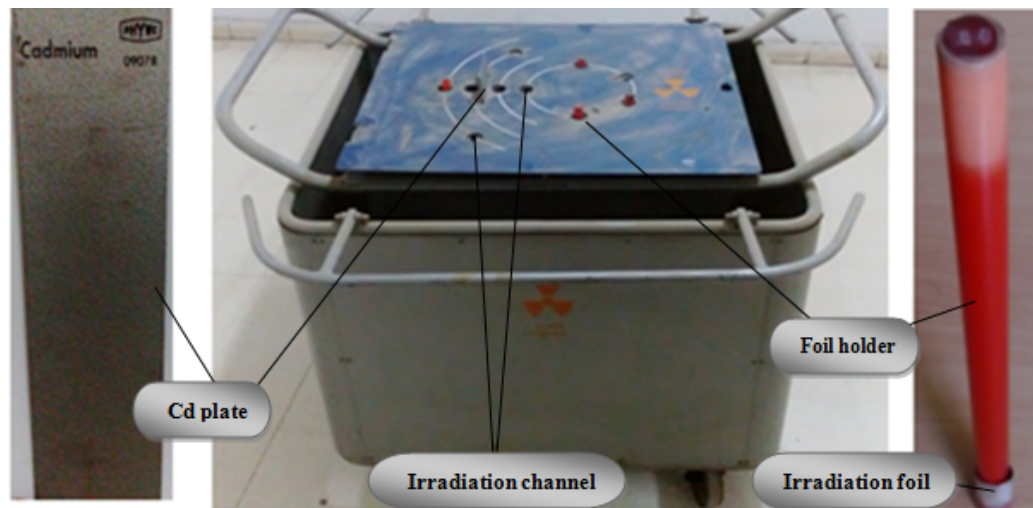


FIG. 1. Neutron irradiator (^{226}Ra - ^9Be) unit (PHYWE).

Radium-Beryllium Source: The ^{226}Ra -Be neutron source is a homogeneous mechanical mixture of an α -emitting nuclide ^{226}Ra with the light element ^9Be . The mixture ratio Be to Ra is 1:5. The mass of the mixture is 3.5 mg. It is enclosed in a two-wall cylindrical tube from nickel then from steel, with a length of 7 cm and an outer diameter of 2 cm. The two-wall cylinder is placed in a cylinder from lead with a length of 7 cm and a diameter of 4 cm. The flux rate of

this source is up to $9.09\times 10^4\text{ n/s}$, in view of the fact that the decay of ^{226}Ra leads to the alpha-emitting progeny ^{222}Rn and ^{210}Po , producing alpha particles which contribute to the total product of neutrons by a ratio of $6/7\approx 0.86$. The yield of the source ^{226}Ra -Be may reach $2.0\times 10^7\text{ n/s}$ for each 1 Ci from Radium. The source ^{226}Ra -Be can be distinguished by continuous spectra of neutrons with an average ranging from 4 to 5 MeV.

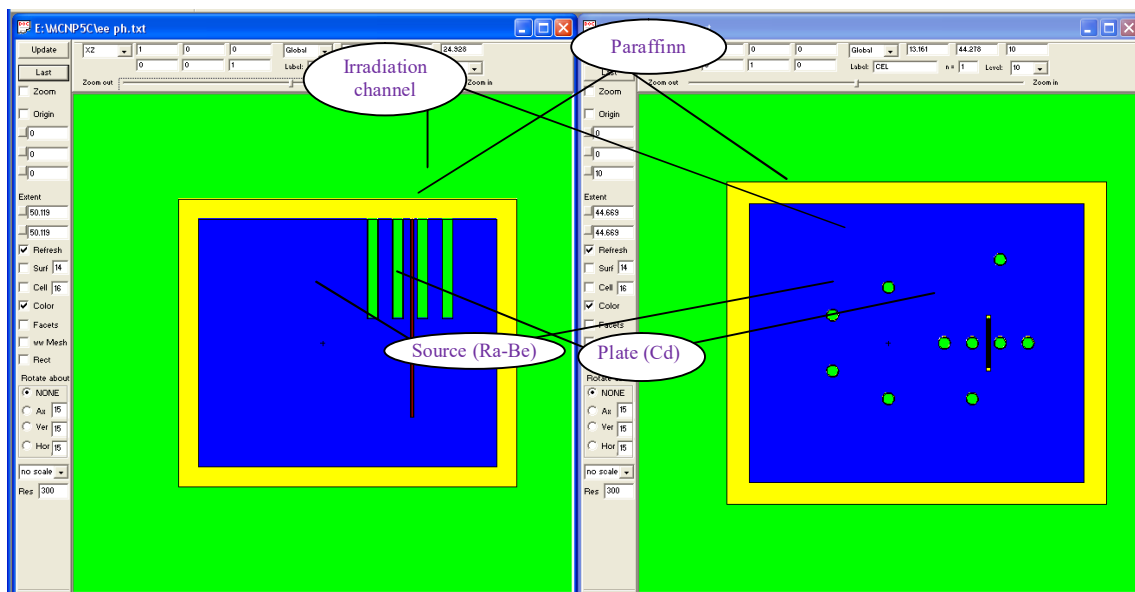
The relatively long-lived Radium 226, with its decay products, form a group of five α -emitting isotopes with energies ranging from 4.8 to 7.7 MeV and an average energy of 5.8 MeV. These energies are enough for surmounting the potential barrier of a beryllium nucleus which is approximately 4.0 MeV. However, alpha particles interact with the atomic electrons of beryllium, so that they lose a part of their energy and slow down to below 4.0 MeV. Therefore, not all alpha particles can excite the nuclear interaction (α, n) in beryllium; only $(1-1.5) \times 10^4$ particles can penetrate beryllium nuclei [4].

Simulation of $^{226}\text{Ra-Be}$ Unit Using MCNP Code

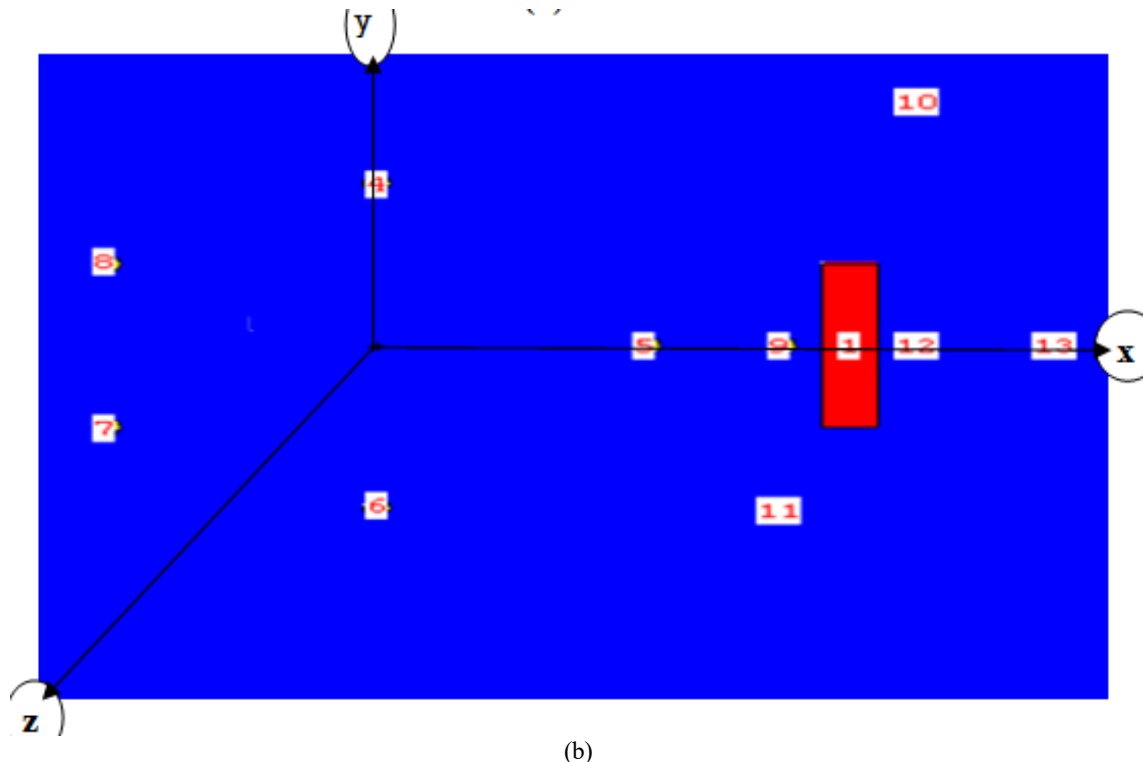
MCNP5 is a general-purpose Monte Carlo N-Particle code that can be used for neutron, photon, electron or coupled neutron, photon and electron transport. It can also be used for three-dimensional, time-dependent general geometry. This code is widely used around the world for

many radiation protection and shielding applications [5]. MCNP, V5 has various new user features. These include: improved photon physics, neutral particle radiography, enhancements and additions to variance reduction methods, new source options, improved parallelism support (PVM, MPI, Open MP) and new nuclear and atomic data libraries [6].

The neutron source $^{226}\text{Ra-Be}$ was simulated as a point source located at the center of coordinates (0,0,0). The source definition card (SDEF) was used to describe the source $^{226}\text{Ra-Be}$. The neutron spectrum of $^{226}\text{Ra-Be}$ was used from literature [1]. The container, around the source, was filled with paraffin except in the defined channels (Fig. 2). In addition, Table 2 shows the physical properties of the irradiator as used in the simulation by MCNP5 code.



(a)



(b)
FIG. 2. a) Diagram for the ^{226}Ra -Be irradiator unit using Vized program. b) Irradiation channels and Cadmium plate [3].

TABLE 2. Physical properties of irradiator as used in the simulation by MCNP5 code

Name	Shape	Position relative to ^{226}Ra -Be (cm)	Notice
Channel number	Irradiator channel with a diameter of 2cm (according to its number in the simulation)		
4	Cylinder	10	On axis Oy
5	Cylinder	10	On axis Ox
6	Cylinder	-10	On axis Oy
7	Cylinder	-10	On axis xOy
8	Cylinder	-10	On axis xOy
9	Cylinder	15	On axis Ox
10	Cylinder	25	In plane xOy
11	Cylinder	20	In plane xOy
12	Cylinder	20	On axis Ox
13	Cylinder	25	On axis Ox
Material carrier	Cylinder	radius (0.5 cm) and length (30 cm)	The length inside paraffin = 20 cm
Source ^{226}Ra -Be			
^{226}Ra -Be Mixture	Cylinder	The mixture is in a pair-wall cylindrical tube from nickel then from steel, length = 7 cm and diameter = 2 cm. Ratio of ^{226}Ra to ^9Be = 1/5, mass= 3.5 mg	
Cylinder of steel	Cylinder	Length = 7 cm, diameter = 2 cm	
Source carrier	Cylinder	Length = 18 cm, diameter = 4 cm	

Results and Discussion

Calculation of the Neutron Flux inside the Irradiator Channels

Using the F4 (flux averaged over a cell (particles/cm²)) card in MCNP5, the neutron flux was calculated in different channels, where the neutron flux is proportional to path grand total K with a length L_k for neutrons with energy E_j across the channel volume as illustrated in Eq. (1):

$$\Phi_j \propto \frac{1}{V} \sum_{k=1}^K L_k(E_j). \quad (1)$$

The neutron flux $\Phi_j(\text{cm}^{-2})$ is expressed using F4 card, as in Eq. (2) [5]:

$$F_4 = \int_V \int_t \int_E \Phi(\vec{r}, E, t) dE dt \frac{dV}{V}. \quad (2)$$

Fig. 3 shows the composition of the neutron flux (thermal, medium and fast) at the channels of the irradiator unit as obtained from MCNP5 code. Obviously, the neutron flux decreases away from the source. In addition, the thermal neutron flux dominates at all channels, except for those which contain Cadmium plates.

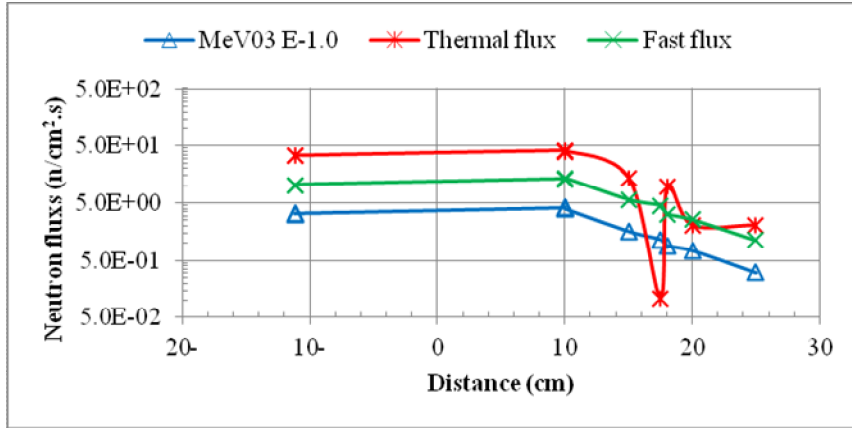


FIG. 3. Neutron flux at irradiator channels according to their distance from the source.

The ratio “thermal to fast”:

- equals, in average, 3.17 ± 0.03 at channels 4,5,6,7 and 8;
- decreases to 0.024 ± 0.01 at Cadmium plate;
- decreases to 0.8 ± 0.02 and 1.83 ± 0.01 in channels 12 and 13, respectively, as these

channels are located behind the Cadmium plate,

- equals 2.41 ± 0.03 , 3.01 ± 0.04 and 2.95 ± 0.02 at channels 9,10 and 11, respectively.

Figs. 4 to 8 show the changes of neutron flux versus the neutron energy at the channels and the Cadmium plate.

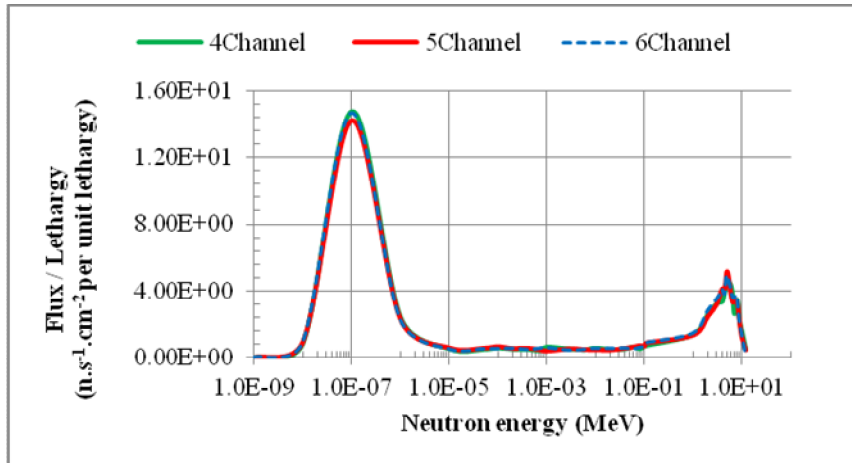


FIG. 4. Neutron flux vs. neutron energy at channels 4, 5 and 6.

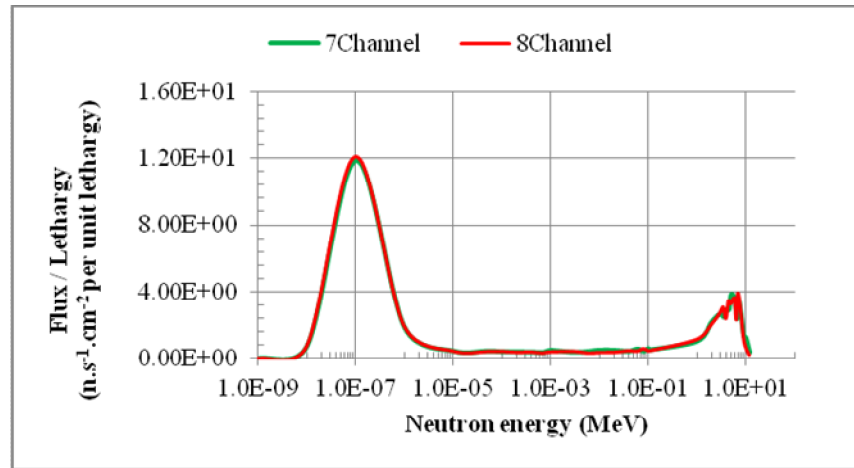


FIG. 5. Neutron flux vs. neutron energy at channels 7 and 8.

TABLE 3. The neutron flux (thermal, medium, and fast) at channels 4, 5, 6, 7 and 8.

Channel number	(10^{-9} to 10^{-6}) MeV	(10^{-5} to 10^{-1}) MeV	(0.11 to 12) MeV
4, 5, 6	71.0%	10.7%	18.3%
7, 8	72.4%	10.4%	17.9%

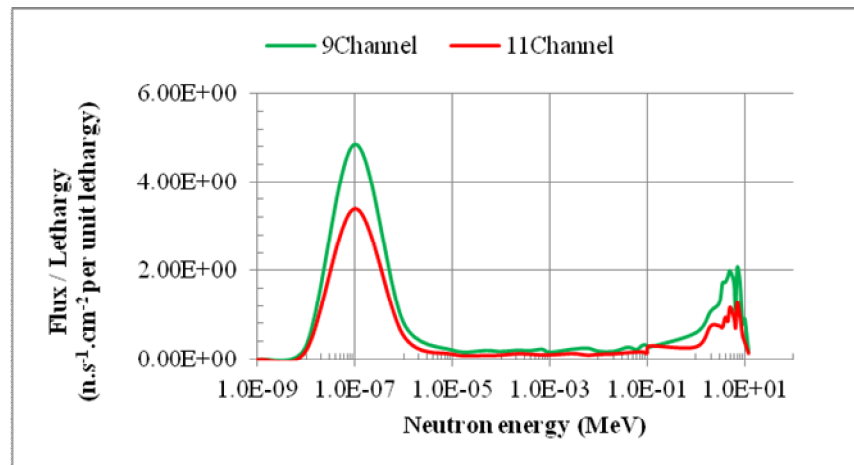


FIG. 6. Neutron flux vs. neutron energy at channels 9 and 11.

TABLE 4. The neutron flux (thermal, medium and fast) at channels 9 and 11.

Channel number	(10^{-9} to 10^{-6}) MeV	(10^{-5} to 10^{-1}) MeV	(0.11 to 12) MeV
9	66.1%	12.1%	21.8%
11	70.4%	10.8%	18.8%

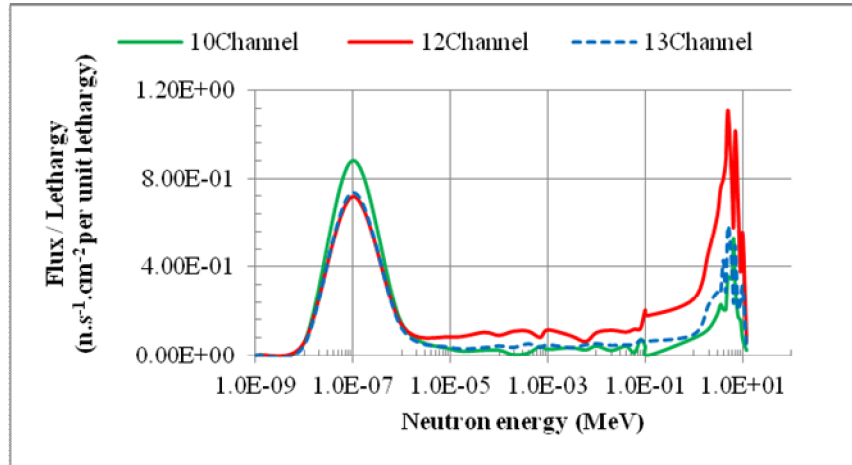


FIG. 7. Neutron flux vs. neutron energy at channels 10, 12 and 13.

TABLE 5. The neutron flux (thermal, medium and fast) at channels 10, 12 and 13.

Channel number	$(10^{-9}$ to $10^{-6})$ MeV	$(10^{-5}$ to $10^{-1})$ MeV	(0.11 to 12) MeV
10	72.0%	10.0%	18.0%
12	40.0%	21.0%	39.0%
13	60.0%	14.0%	26.0%

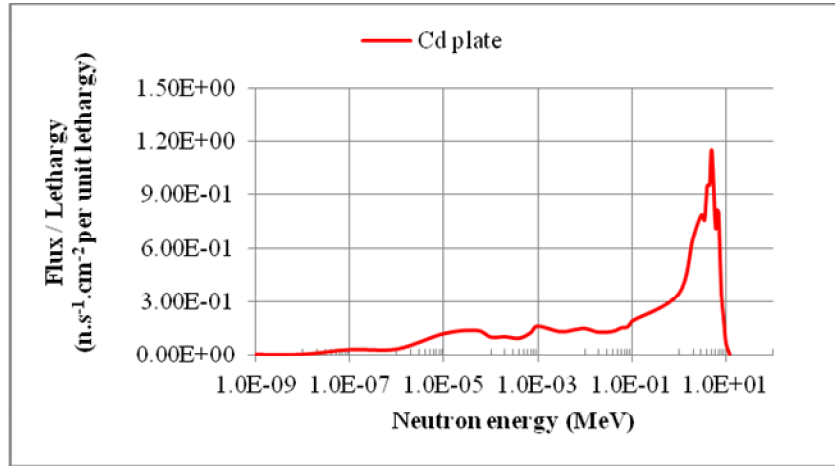


FIG. 8. Neutron flux vs. neutron energy at Cadmium plate.

Fig. 8 shows that the neutron flux at the Cadmium plate is composed generally from fast neutrons in the range (0.11-12.0) MeV with a ratio of 63.0% and in the energy range $(10^{-9} - 10^{-6})$ MeV with a ratio of 3.0%, while a ratio of 34.0% is formed by neutrons in the energy range $(10^{-5} - 10^{-1})$ MeV.

As shown in Figs. (9, 10 and 11), the Cadmium plate plays an effective role in reducing the total neutron flux from the Ra-Be source at channels 12 and 13 with a ratio of

40.0% and 17.0%, respectively. On the other hand, the absence of the Cadmium plate will lead to increase the thermal neutron flux ratio to 64.0% and 66.0% (in channels 12 and 13, respectively) and reduce the fast neutron flux to 24.0% and 22.0% (in channels 12 and 13, respectively). Also, the short distance between the source and some channels and the absorption in the moderator reduce the neutron flux in close channels.

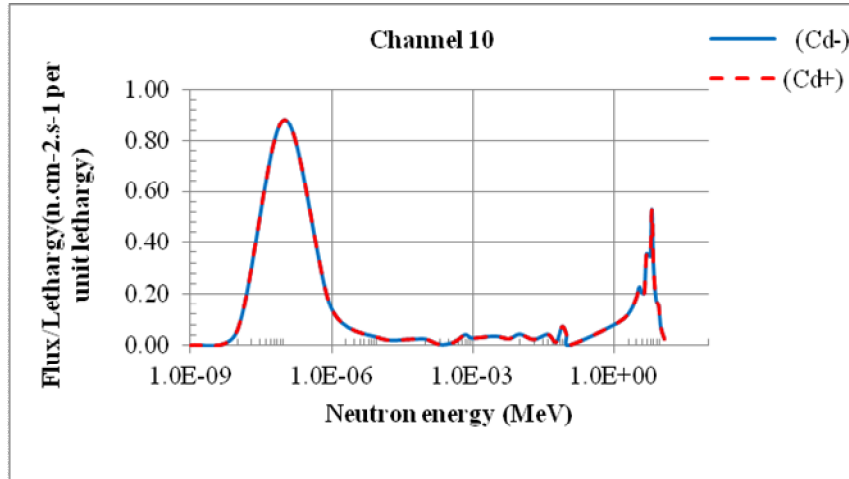


FIG. 9. Neutron flux vs. neutron energy at channel 10 with and without Cadmium plate.

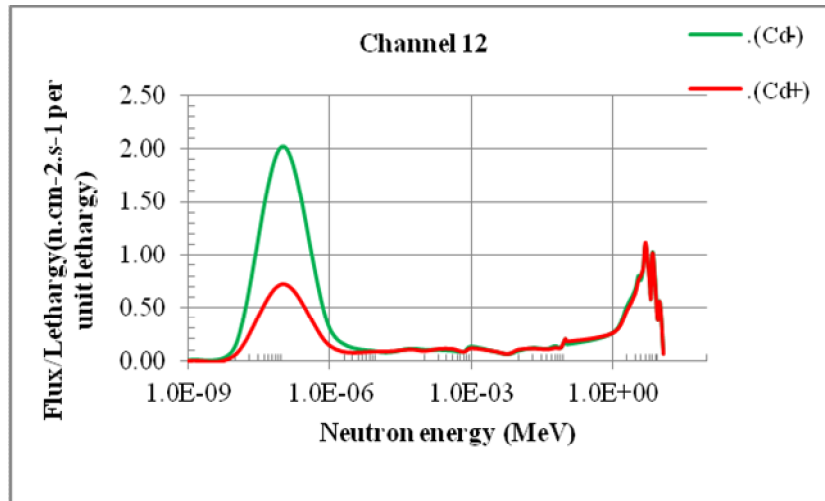


FIG. 10. Neutron flux vs. neutron energy at channel 12 with and without Cadmium plate.

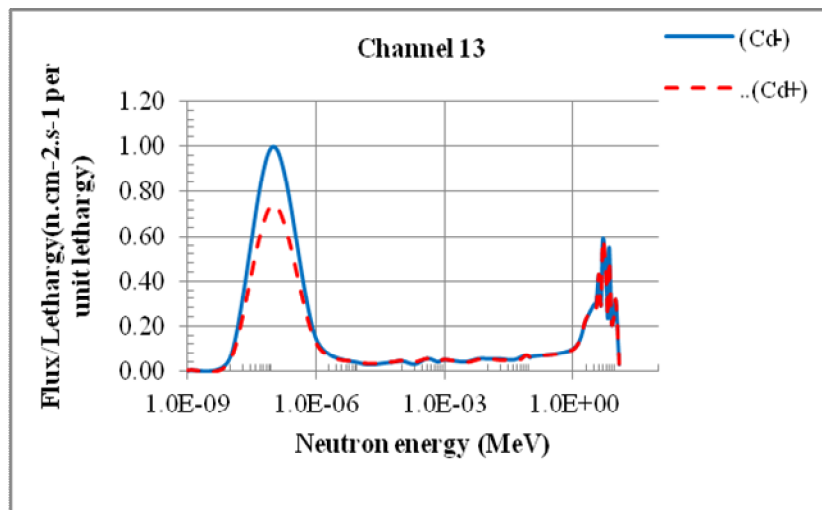


FIG. 11. Neutron flux vs. neutron energy at channel 13 with and without Cadmium plate.

Calculation of the Dose at the Surface

The card F5 (flux at a point or ring detector (particles/cm²)) was used to calculate the neutron and photon doses at points located on the upper surface of the irradiator unit. Fig. 12 shows the dose values at points located on the irradiator. It can be noticed that both neutron and photon

doses have a maximum value near the point $x=0$ on axis Ox, then the dose decreases as the neutron flux decreases away from the source. The asymmetry of the dose distribution is due to the fact that the source is not in the center of the container.

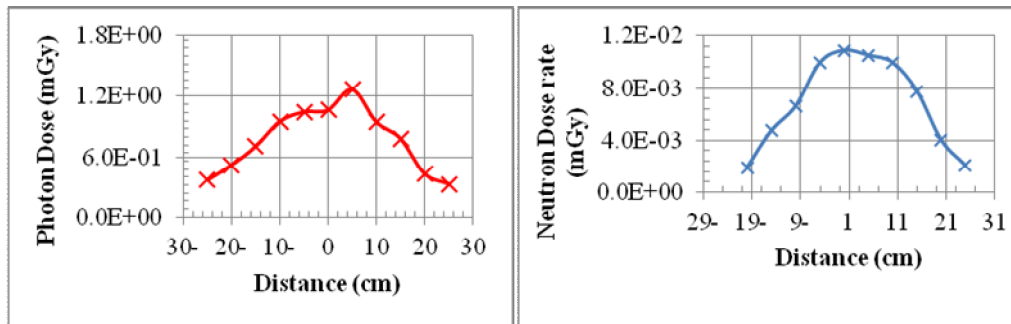


FIG. 12. Neutron and photon dose at points located on the irradiator unit.

The radiation (neutron and photon) dose on the surface of the irradiator unit was calculated by using MCNP5 code for radiation protection purposes. The results (Table 6) revealed that the

dose received by workers, from this unit, is very low in comparison with the recommended annual dose limit for radiation workers (20 mSv/y).

TABLE 6. Neutron and photon doses on the upper surface of the irradiator (^{226}Ra -Be) unit by using MCNP5 code.

Particles	Effective dose (μSv)
Neutrons	$3.43 \times 10^{-7} \text{ Rem/h} = 0.03 \text{ mSv} = 30 \mu\text{Sv}$
Photons	$1.64 \times 10^{-5} \text{ Rem/h} = 0.6 \text{ mSv} = 60 \mu\text{Sv}$

Calculation of the Dose at Channels 5 and 12

It was supposed that the total radiation dose is composed of a neutron dose (scattering of fast neutrons on material moderator) and a photon dose (resulting from the absorption of thermal neutrons in hydrogen nuclei).

The card F6 (energy deposition averaged over a cell (MeV/g)) was used for the calculation of radiation doses at channels 5 and 12 only. Table 7 shows the calculated radiation doses at channels 5 and 12 by using MCNP5 code.

TABLE 7. Radiation doses at channels 5 and 12 calculated by using MCNP5 code.

Channel number	Neutron dose		Photon dose		Sum (mGy)
	J/kg	mGy	J/kg	mGy	
5	1.67×10^{-3}	23.31 ± 0.01	1.90×10^{-3}	16.14 ± 0.02	39.45
12	1.15×10^{-4}	2.66 ± 0.03	3.33×10^{-4}	4.66 ± 0.01	7.32

Measurement of the Radiation Dose at Channels 5 and 12 Using Thermoluminescent Dosimeters (TLDs)

Thermoluminescent dosimeters, TLD-700 type, were used to measure the absorbed dose in channels 5 and 12. Four dosimeters were placed inside each channel, on a cylindrical plastic carrier, for one month. Two dosimeters were

placed outside the irradiator to measure the background.

The calibration of TLD chips was carried out using a ^{137}Cs source. The chips were read using Harshaw reader, Model 4500 [7]. The results at channels 5 and 12 are given in Table 8 to compare with those from simulation. As shown, there is a good agreement between both measured and simulated results.

TABLE 8. Measured radiation doses at channels 5 and 12 by using MCNP5 code and TLDs.

Channel number	Total dose by TLD (mGy)	Total dose by MCNP(mGy)	Difference percentage
5	41.00±0.05	39.45±0.02	3.8%
12	7.87±0.8	7.32±0.03	7.2%

Conclusions

The results presented in this work show that the calculation of neutron fluxes in ^{226}Ra -Be unit is very important and useful to understand the neutron flux in each channel for neutron activation analysis. Also, the calculated doses on the surface of the irradiator unit prove that it is

safe from the radiation protection point of view. The simulated radiation dose results were validated by carrying out measurements with TLDs, where good agreement was found between the measured and the simulated values for channels 5 and 12.

References

- [1] Geiger, K.W., Hum, R. and Jarvis, C.J.D., Canadian Journal of Physics, 42 (1964) 1099.
- [2] Bechtel, R.D., Thesis Presented to the Faculty of Graduate Studies, Georgia Institute of Technology, (2007).
- [3] AlTaani, A. and Nahili, M., Journal of Damascus University for Basic Sciences, (2015).
- [4] Livin, V.E., "Nuclear Physics and Nuclear Reactors", (Moscow, 1981).
- [5] X-5 Monte Carlo Team. Diagnostics Application Group. Los Alamos National Laboratory. MCNP-A General Monte Carlo, N-Particle Transport Code, VERSION 5. (2003).
- [6] Brown, F.B., Barrett, R.F., Booth, T.E., Bull, J.S., Cox, L.J., Forster, R.A., Goorley, T.J., Mosteller, R.D., Post, S.E., Prael, R.E., Selcow, E.C., Sood, A. and Sweezy, J., Nuclear Instruments and Methods in Physics Research, Section B, Beam Interactions with Materials and Atoms, 213(1) (2004) 82.
- [7] Boyd, W.L., UNLV Theses, Dissertations, Professional Papers and Capstones. (2009) 1203.

Jordan Journal of Physics

ARTICLE

Analytic Approximate Solution of Blasius Equation Using Homotopy Perturbation Method (HPM)

Hamza Berrehal and Abdelaziz Maougal

Energy Physics Laboratory, University of Brothers Mentouri Constantine, Algeria.

Received on: 7/8/2016;

Accepted on: 10/11/2016

Abstract: In this paper, an incompressible viscous fluid flow over a flat plate is presented. The homotopy perturbation method (HPM) is employed to solve the well-known nonlinear Blasius differential equation. We used this new analytic approximated technique, which gave us a very close result to the exact solution. The obtained results have been compared with numerical and exact solutions of Blasius equation, showing the high accuracy of the results obtained in our study.

Keywords: Homotopy perturbation method (HPM), Nonlinear differential equation.

Notation:

HPM - Homotopy perturbation method
 NM - Numerical method
 p - Homotopy parameter
 Re - Reynold's number
 u - Velocity component in x direction
 v - Velocity component in y direction
 x - Dimensional horizontal coordinate
 y - Dimensional vertical coordinate
 η - Dimensionless similarity variable

Introduction

The homotopy perturbation method (HPM) provides an approximate analytical solution in a series form. This method was introduced by He [6-17] in 1998. It has been widely successfully used by numerous researchers for different physical systems, such as: reaction-diffusion equation and heat radiation equation [4, 5], MHD Jeffery-Hamel problem [18], bifurcation, asymptology, nonlinear wave equation, oscillators with discontinuities and bifurcation [11, 12, 13 and 14]. In this paper, we will apply homotopy perturbation method to the problem of boundary layer flow over a flat plate.

Blasius equation is one of the fundamental and basic fluid dynamics equations. It describes the non-dimensional velocity distribution in the laminar boundary layer over a flat plate. It describes the fluid flow's viscous effect [1, 3]. Boundary layer flow over a flat plate is governed

by the continuity and the momentum equations. For a two dimensional steady state, incompressible fluid flow with zero pressure gradient over a flat plate, governing equations are simplified to:

$$\frac{\partial u}{\partial x} + \frac{\partial v}{\partial y} = 0, \quad (1)$$

$$u \frac{\partial u}{\partial x} + v \frac{\partial u}{\partial y} = \nu \frac{\partial^2 u}{\partial y^2}. \quad (2)$$

With boundary conditions:

$$y = 0, u = 0, \quad (3)$$

$$y = \infty, u = U_{\infty}, \frac{\partial u}{\partial y} = 0. \quad (4)$$

By applying a dimensionless variable (η) defined as:

$$\eta = \frac{y}{\sqrt{x}} Re^{1/2} \quad (5)$$

'Re' is Reynolds number, defined as: $Re = \frac{u_\infty x}{\nu}$, the governing Eqs. (1) and (2) can be reduced to the well-known Blasius equation, where Y depends on the similarity variable (η):

$$Y'''(\eta) + \frac{1}{2}Y(\eta)Y''(\eta) = 0. \quad (6)$$

With boundary conditions:

$$\eta = 0, Y = 0, \frac{\partial Y}{\partial \eta} = 0, \quad (7)$$

$$\eta = \infty, \frac{\partial Y}{\partial \eta} = 1, \quad (8)$$

where Y is related to u (velocity) by $\frac{u}{u_\infty} = Y'(\eta)$ and the «prime» denotes the derivatives with respect to η .

Basic Idea of Homotopy Perturbation Method

The homotopy perturbation method is a combination of the classical perturbation technique and homotopy technique. To explain the basic idea of the HPM for solving nonlinear differential equations, we consider the following nonlinear differential equation:

$$A(s) - f(r) = 0, r \in \Omega. \quad (9)$$

Subject to boundary condition:

$$B\left(s, \frac{\partial s}{\partial n}\right) = 0, r \in \Gamma \quad (10)$$

where A is a general differential operator, B is a boundary operator, $f(r)$ is a known analytical function, Γ is the boundary of domain Ω and $(\partial s / \partial n)$ denotes differentiation along the normal drawn outwards from Ω .

The operator A can, generally speaking, be divided into two parts: a linear part 'L' and a nonlinear part 'N'. Eq. (9), therefore, can be rewritten as follows:

$$L(s) + N(s) - f(r) = 0. \quad (11)$$

By the homotopy technique (1), (2), we construct a homotopy $v(r, p): \Omega \times [0, 1] \rightarrow R$ which satisfies:

$$H(v, p) = (1 - p)[L(v) - L(v_0)] + p[A(v) - f(r)] = 0,$$

$$p \in [0, 1], r \in \Omega. \quad (12)$$

Or

$$H(v, p) = L(v) - L(s_0) + pL(s_0) + p[N(v) - f(r)] = 0, \quad (13)$$

where $p \in [0, 1]$ is an embedding parameter. s_0 is an initial approximation of Eq. (9) which satisfies the boundary conditions. Obviously from Eqs. (12) and (13), we have:

$$H(v, 0) = L(v) - L(s_0) = 0, \quad (14)$$

$$H(v, 1) = A(v) - f(r) = 0. \quad (15)$$

The changing process of p from zero to unity is just that of $v(r, p)$ from $s_0(r)$ to $s(r)$. In topology, this is called deformation and $L(v) - L(s_0)$, $A(v) - f(r)$ are called homotopic.

In this paper, the authors will first use the imbedding parameter p as a "small parameter" and assume that the solution of Eqs. (12) and (13) can be written as a power series in p :

$$v = v_0 + pv_1 + p^2v_2 + p^3v_3 + \dots \quad (16)$$

Setting $p = 1$ results in the approximate solution of Eq. (9):

$$s = \lim_{p \rightarrow 1} v = v_0 + v_1 + v_2 + v_3 + \dots \quad (17)$$

The coupling of the perturbation method and the homotopy method is called the homotopy perturbation method, which has eliminated limitations of the traditional perturbation methods. On the other hand, the proposed technique can take full advantage of the traditional perturbation techniques.

Applied Homotopy Perturbation Method

According to Eq. (12) and Eq. (6):

$$(1 - p)(Y''' - Y_0''') + p\left(Y''' + \frac{1}{2}YY''\right) = 0. \quad (18)$$

We consider Y as follows:

$$Y = Y_0 + pY_1 + p^2Y_2 + p^3Y_3 + \dots \quad (19)$$

Assuming $Y_0''' = 0$ and substituting Y from Eq. (19) into Eq. (18) with simplification and rearranging based on powers of p -terms, we have:

$$p^0: \begin{cases} Y_0''' = 0, \\ Y_0(0) = 0, Y_0'(0) = 0, Y_0'(\infty) = 1, \end{cases} \quad (20)$$

$$p^1: \begin{cases} Y_1''' = -\frac{1}{2}Y_0Y_0'', \\ Y_1(0) = 0, Y_1'(0) = 0, Y_1'(\infty) = 0, \end{cases} \quad (21)$$

$$p^2: \begin{cases} Y_2''' = -\frac{1}{2}(Y_1Y_0'' + Y_0Y_1''), \\ Y_2(0) = 0, Y_2'(0) = 0, Y_2'(\infty) = 0, \end{cases} \quad (22)$$

$$p^3: \begin{cases} Y_3''' = -\frac{1}{2}(Y_2Y_0'' + Y_1Y_1'' + Y_0Y_2''), \\ Y_3(0) = 0, Y_3'(0) = 0, Y_3'(\infty) = 0, \end{cases} \quad (23)$$

$$p^4: \left\{ \begin{array}{l} Y_4''' = -\frac{1}{2} \left(\begin{array}{l} Y_3 Y_0'' + Y_1 Y_2'' \\ + Y_2 Y_1'' + Y_0 Y_3'' \end{array} \right), \\ Y_4(0) = 0, Y_4'(0) = 0, Y_4'(\infty) = 0, \end{array} \right\} \quad (24)$$

$$p^5: \left\{ \begin{array}{l} Y_5''' = -\frac{1}{2} \left(\begin{array}{l} Y_4 Y_0'' + Y_1 Y_3'' + Y_2 Y_2'' \\ + Y_3 Y_1'' + Y_0 Y_4'' \end{array} \right), \\ Y_5(0) = 0, Y_5'(0) = 0, Y_5'(\infty) = 0, \end{array} \right\} \quad (25)$$

$$p^6: \left\{ \begin{array}{l} Y_6''' = -\frac{1}{2} \left(\begin{array}{l} Y_5 Y_0'' + Y_1 Y_4'' + Y_2 Y_3'' \\ + Y_3 Y_2'' + Y_4 Y_1'' + Y_0 Y_5'' \end{array} \right), \\ Y_6(0) = 0, Y_6'(0) = 0, Y_6'(\infty) = 0, \end{array} \right\} \quad (26)$$

$$p^7: \left\{ \begin{array}{l} Y_7''' = -\frac{1}{2} \left(\begin{array}{l} Y_6 Y_0'' + Y_1 Y_5'' + Y_2 Y_4'' \\ + Y_3 Y_3'' + Y_4 Y_2'' \\ + Y_5 Y_1'' + Y_0 Y_6'' \end{array} \right), \\ Y_7(0) = 0, Y_7'(0) = 0, Y_7'(\infty) = 0, \end{array} \right\} \quad (27)$$

$$p^8: \left\{ \begin{array}{l} Y_8''' = -\frac{1}{2} \left(\begin{array}{l} Y_7 Y_0'' + Y_1 Y_6'' + Y_2 Y_5'' \\ + Y_3 Y_4'' + Y_4 Y_3'' + Y_5 Y_2'' \\ + Y_6 Y_1'' + Y_0 Y_7'' \end{array} \right), \\ Y_8(0) = 0, Y_8'(0) = 0, Y_8'(\infty) = 0, \end{array} \right\} \quad (28)$$

$$p^9: \left\{ \begin{array}{l} Y_9''' = -\frac{1}{2} \left(\begin{array}{l} Y_8 Y_0'' + Y_1 Y_7'' + Y_2 Y_6'' \\ + Y_3 Y_5'' + Y_4 Y_4'' + Y_5 Y_3'' \\ + Y_6 Y_2'' + Y_7 Y_1'' + Y_0 Y_8'' \end{array} \right), \\ Y_9(0) = 0, Y_9'(0) = 0, Y_9'(\infty) = 0, \end{array} \right\} \quad (29)$$

$$p^{10}: \left\{ \begin{array}{l} Y_{10}''' = -\frac{1}{2} \left(\begin{array}{l} Y_9 Y_0'' + Y_1 Y_8'' + Y_2 Y_7'' \\ + Y_3 Y_6'' + Y_4 Y_5'' + Y_5 Y_4'' \\ + Y_6 Y_3'' + Y_7 Y_2'' \\ + Y_8 Y_1'' + Y_0 Y_9'' \end{array} \right), \\ Y_{10}(0) = 0, Y_{10}'(0) = 0, Y_{10}'(\infty) = 0, \end{array} \right\} \quad (30)$$

$$Y_0 = 0.1000000000\eta^2 \quad (31)$$

$$Y_1 = -0.00016666666667\eta^5 + 0.052083333333\eta^2 \quad (32)$$

$$Y_2 = 5.456349206 \cdot 10^{-7}\eta^8 - 0.00017361111111\eta^5 + 0.02015128968\eta^2 \quad (33)$$

According to Eq. (19) and the assumption $p = 1$, we get:

$$Y(\eta) = 0.1671626869\eta^2 - 0.0004628220598\eta^5 + 0.000002467370720\eta^8 - 1.423254413 \cdot 10^{-8}\eta^{11} + 8.778652458 \cdot 10^{-11}\eta^{14} - 4.975492933 \cdot 10^{-13}\eta^{17} + 2.172575632 \cdot 10^{-15}\eta^{20} - 6.641569482 \cdot 10^{-18}\eta^{23} + 1.328726161 \cdot 10^{-20}\eta^{26} - 1.564862171 \cdot 10^{-23}\eta^{29} + 8.247729923 \cdot 10^{-27}\eta^{32} \quad (34)$$

Since Eq. (20), the analytical solution is hard; it is therefore solved here by homotopy perturbation method using MAPLE software. The results of homotopy perturbation method and numerical method are given in Table1. Tables 2 and 3 are made to compare the present results with those given by Blasius [2]. In Figs. 1 and 2, we can also see the comparison between the obtained results (present method) and the numerical solution.

Solving Eqs. (20 – 30) with boundary condition, we obtain:

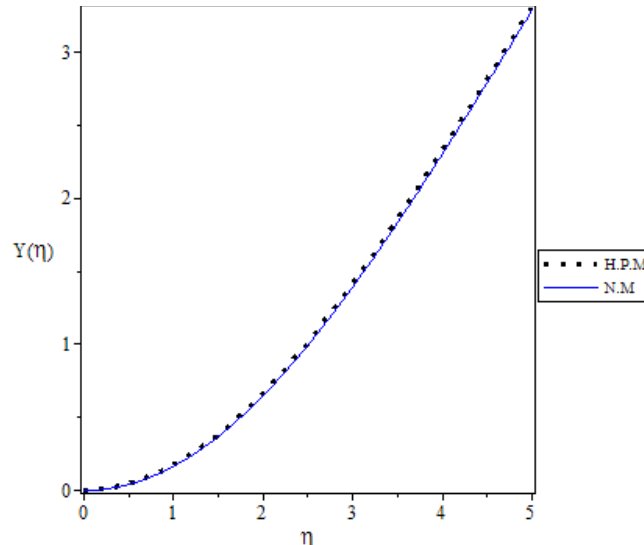


FIG. 1. Comparison of answers obtained by H.P.M. and N.M. results for $Y(\eta)$.

TABLE 1. The results of H.P.M. and N.M. methods.

η	$Y(\eta)$		$Y'(\eta)$	
	H.P.M. (p=10)	N.M.	H.P.M. (p=10)	N.M.
0	0	0	0	0
0.4	0.026741292	0.026887377	0.133670940	0.134400700
0.8	0.106832875	0.107414939	0.266516562	0.267961973
1.2	0.239573124	0.240869221	0.396461681	0.398574578
1.6	0.423186968	0.425446810	0.520268033	0.522954471
2	0.654444316	0.657872167	0.634000791	0.637131917
2.4	0.928520792	0.933268983	0.733763027	0.737217411
2.8	1.239185206	1.245369509	0.816560319	0.820286959
3.2	1.579318691	1.587055035	0.881050260	0.885097710
3.6	1.941669782	1.951099322	0.927940394	0.932352513
4	2.319673271	2.330906305	0.959892824	0.964408547
4.4	2.708117939	2.721040628	0.980851449	0.984576798
4.8	3.103424210	3.117446609	0.994783348	0.996320878
4.99	3.292920198	3.307099328	0.999762196	0.999843011
5	3.302919009	3.317098554	0.999999998	0.999999999

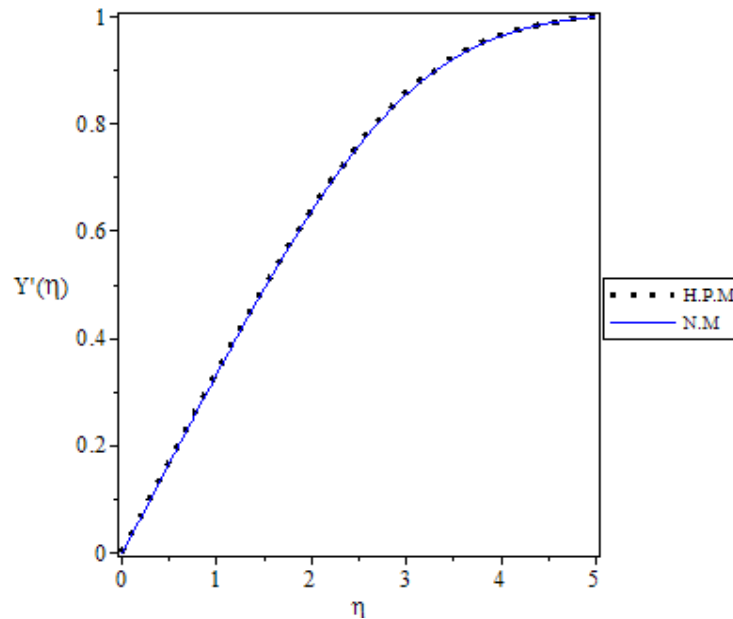


FIG. 2. Comparison of answers obtained by H.P.M. and N.M. results for $Y'(\eta)$.

TABLE 2. Obtained results by H.P.M. for $Y(\eta)$ and $Y'(\eta)$ in comparison with Blasius's results.

η	$Y(\eta)$				$Y'(\eta)$			
	H.P.M. (p=5)	H.P.M. (p=7)	H.P.M. (p=10)	Blasius	H.P.M. (p=5)	H.P.M. (p=7)	H.P.M. (p=10)	Blasius
0	0	0	0	0	0	0	0	0
0.5	0.0414	0.0415	0.0418	0.0415	0.1654	0.1657	0.1670	0.1659
1	0.1651	0.1654	0.1667	0.1656	0.3288	0.3295	0.3320	0.3298
1.5	0.3690	0.3699	0.3727	0.3701	0.4848	0.4866	0.4901	0.4868
2	0.6474	0.6497	0.6544	0.6500	0.6260	0.6299	0.6340	0.6298
2.5	0.9912	0.9963	1.0030	0.9963	0.7446	0.7524	0.7561	0.7513
3	1.3875	1.3978	1.4060	1.3968	0.8360	0.8494	0.8511	0.8460
3.5	1.8228	1.8413	1.8494	1.8377	0.9010	0.9199	0.9176	0.9130
4	2.2852	2.3137	2.3197	2.3057	0.9460	0.9660	0.9599	0.9555
4.5	2.7667	2.8038	2.8064	2.7901	0.9783	0.9910	0.9846	0.9795
5	3.2618	3.3021	3.3029	3.2833	1	1	0.9999	0.9915

TABLE 3. Obtained results for $Y''(0)$ in comparison with order (HPM) approximants and Blasius's results.

$Y''_{\text{Blasius}}(0) = 0.3321$					
Order H.P.M. Approximants	$Y''(0)$	Relative Error %	Order H.P.M. Approximants	$Y''(0)$	Relative Error %
1	0.3445	3.73	6	0.3294	0.81
2	0.3445	3.73	7	0.3318	0.09
3	0.3485	4.94	8	0.3344	0.69
4	0.3401	2.41	9	0.3352	0.93
5	0.3312	0.27	10	0.3343	0.66

Conclusion

In this article, we have studied the Blasius equation and solved it using a new technique called homotopy perturbation method (HPM). The results show that this perturbation scheme provides an excellent approximation to the

nonlinear equation's solution with high accuracy. We found that this method is more accurate for higher orders of the embedding parameter p and this method doesn't require any discretization or small perturbation parameter.

References

- [1] Belhachmi, Z., Bright, B. and Taous, K., Acta Mat. Univ. Comenianae LXIX, 2 (2000) 199.
- [2] Blasius, H., Zeitschrift für Mathematik und Physik, 56(1) (1908) 1; English translation available as NACATM1256, February (1950).
- [3] Datta, B.K., Indian J. Pure Appl. Math., 2 (2003) 237.
- [4] Ganji, D.D. and Rajabi, A., Int. J. Commun. Heat Mass Transfer, 33 (2006) 391.
- [5] Ganji, D.D. and Sadighi, A., Int. J. Nonlinear Sci. Numer. Simul., 7(4) (2006) 411.
- [6] He, J.H., Commun. Nonlinear Sci. Numer. Simul., 4 (1998) 260.
- [7] He, J.H., Computer Methods in Applied Mechanics and Engineering, 178 (1999) 257.
- [8] He, J.H., International Journal of Non-Linear Mechanics, 35(1) (2000) 37.
- [9] He, J.H., Appl. Math. Comput., 114 (2000) 115.
- [10] He, J.H., Applied Mathematics and Computation, 156 (2004) 527.
- [11] He, J.H., Appl. Math. Comput., 156 (3) (2004) 591.

- [12] He, J.H., *Appl. Math. Comput.*, 151 (2004) 287.
- [13] He, J.H., *Chaos Solution Fractals*, 26 (2005) 695.
- [14] He, J.H., *Int. J. Non-linear Sci. Numer. Simul.*, 8 (2005) 207.
- [15] He, J.H., *Phys. Lett. A*, 350 (2006) 87.
- [16] He, J.H., "Non-perturbation Method for Strongly Nonlinear Problems". (Berlin, Dissertation, De-Verlagim Interet. Grmb, 2006).
- [17] He, J.H., *Int. J. Mod. Phys.*, 20(10) (2006) 1141.
- [18] Moghimi, S.M., Ganji, D.D. Baramia, H., Hosseini, M. and Jalaal, M., *Comput. Math. App.*, 61 (2011) 2213.

Jordan Journal of Physics

ARTICLE

Free Breathing Abdominal Imaging with Fat-Water Separation Using 3D Radial Stack-of-Stars Trajectory

Riad S. Ababneh

Physics Department, Yarmouk University, Irbid: 21163, Jordan.

Received on: 21/8/2016;

Accepted on: 3/1/2017

Abstract: In earlier studies of fat-water separation using dynamic imaging applications, the three-dimensional (3D) MRI failed to provide high spatial and temporal resolution. This work proposes a fat-water separation strategy in the abdomen during free breathing using the 3D stack-of-stars (SOS) radial sampling technique. Radial trajectories are less sensitive to motion and have a higher sampling density for the central k-space, allowing for better performance in capturing dynamic information. To this end, a 3D radial TrueFISP sequence was modified to enable the echo time TE to change from projection to projection, where all z-phase encoding was acquired at a single projection angle before switching to the next projection angle. As a result, the fat signal is forced to behave in a specific and easily recognizable fashion over time. Using temporal processing, temporal variations imposed on fat signals can be recognized and fat signals can be separated from water signals.

Keywords: Fat-water separation, TrueFISP, Stack-of-stars, Free breathing.

Introduction

Using the 3D MRI to perform dynamic imaging of the abdomen is difficult due to the inevitable trade-off between temporal and spatial resolution and total acquisition time. Several methods have been proposed to improve temporal resolution and spatial resolution. Examples include view sharing [1], keyhole imaging [2] and the 3D TRICKS [3] method.

A non-Cartesian acquisition of k-space was widely accepted as a potentially superior alternative to the 3D MRI, due to its efficient use of MR gradient hardware and the fact that it is less affected by motion. The most prominent examples are radial trajectories and spiral trajectories. It is considerably more difficult to reconstruct [4] images of non-Cartesian trajectories, because the data points do not fall on a grid in k-space. There are many techniques for reconstructing the non-Cartesian data; for example, using the regularization and estimation theory [5], sampling density compensation in the

MRI [6] and applying the non-uniform fast Fourier transformation (NUFFT) [7] (which is used in this manuscript to reconstruct the data).

Recently, the 3D radial stack-of-stars concept was introduced to reduce the total amount of sampled space and to provide short data acquisition times with high quality images [22]. The 3D k-space with a radial trajectory (using cylindrical sampling) is under-sampled in Fourier space. This trajectory (Fig. 1) is used for dynamic and motion sensitive imaging.

The magnetic resonance signals from fat and water differ slightly in frequency, making it possible to generate images of the places where these two types of tissues separate [8-10]. In applications where fat tends to obscure the pathology or where the disease itself has to do with adipose tissues, this ability can prove very valuable. These approaches, however, are ill-adapted to dynamic applications where temporal resolution is important, because they typically

require lengthy acquisition of three or more separate images with different imaging parameters to allow robust fat-water separation in the presence of magnetic field inhomogeneities.

Radial MRI techniques have gained increasing attention in dynamic imaging and have been successfully used in many applications, such as cardiac imaging [11-14] and abdominal imaging [15-16]. Radial MRI data is sampled using the golden-angle scheme, where the angle of the radial lines is increased continuously by 111.25° , giving a higher sampling density for the central k-space and higher spatial and temporal resolutions. The basic property of this angle is that each successive view divides the largest remaining angular gap and this process continues *ad infinitum*. As a result, the k-space will be approximately uniformly sampled for any number of views chosen for reconstruction. The radial MRI does not detect object motion during data acquisition [17-18], which improves its ability to capture dynamic information. Consequently, more 3D gradient sequences have been developed (radial TrueFISP) that use the stack-of-stars technique to acquire volumetric k-space data. Images acquired during free breathing examinations using the stack-of-stars radial TrueFISP sequence are often of a higher quality than those acquired during conventional

examinations where the patient holds his/her breath [19-21].

This project focused on robust volumetric fat-water separation in the presence of respiratory motion using a 3D radial imaging technique. Existing methodology cannot achieve high-resolution volumetric fat-water separation during a breath-hold exam. While a single volume can be acquired in one held breath, the need to acquire three images for each volume hampers fat-water separation in the abdomen. Therefore, this project was targeted towards developing strategies for the acquisition of 3D volumes to allow robust fat-water separation in the presence of respiratory motion; thus, the stack-of-stars concept has the potential to improve temporal resolution. This approach was implemented and both phantom and volunteer results are presented in the findings.

Materials and Methods

The 3D radial TrueFISP pulse sequence was modified to include radial stack-of-stars k-space sampling in the xy-plane and Cartesian encoding in the z direction. In this sequence, all partitions corresponding to the first radial angle were acquired sequentially before moving to the next angle (see Fig. 1). For angular ordering, the sequence used the golden-angle scheme, where the angle is increased each time by $G_\phi=111.25^\circ$, which corresponds to 180° multiplied by the golden ratio [23].

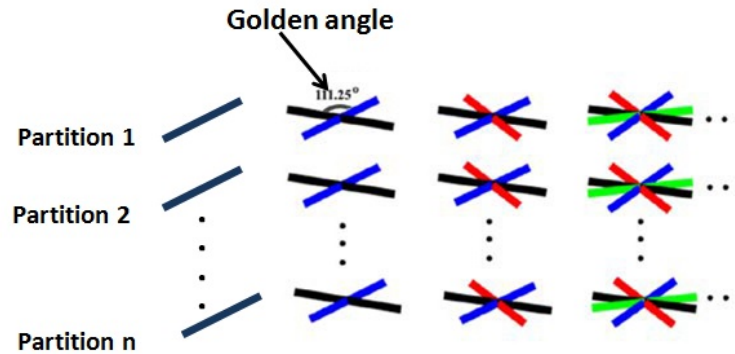


FIG. 1. The stack-of-stars sampling.

The sequence developments were done on IDEA (the SIEMENS sequence development software) and implemented on a clinical 3.0T MRI scanner (SIEMENS Magnetom SKYRA). The development started with the 2D radial bSSFP (Balanced Steady-state free precession) sequence. To that end, a standard Cartesian

Gradient Echo (GE) sequence was modified to build a bSSFP sequence by refocusing all imaging gradients between subsequent excitation radio frequency pulses. A variable delay was inserted before and after each excitation pulse to allow for variable echo times (TE) at constant repetition times (TR). In addition, the frequency

response function was shifted to on-resonance frequency by applying alternating RF-pulse phases (0° - 180°). In the last step, a flip angle ramp and dummy pulses were added to the sequence to minimize oscillations and allow the magnetization to reach steady state. The sequence was extended to allow for a radial acquisition scheme following a quasi-random order of the radial projections. The single-slice sequence described above was extended to allow for volumetric acquisition and respiratory self-gating, by implementing 3D encoding gradient tables and a DC navigator signal after refocusing all imaging gradients. The sequence was validated and tested on phantoms containing different tubes filled with water and oil.

Fig. 2. shows the schematic of the modified sequence allowing for variable echo times (TE) at constant repetition time (TR). In this sequence, TE was made to vary between

subsequent spokes. Specifically, a series of 3 TEs was employed and periodically repeated following a radial golden angle projection order, thereby distributing the acquired fat signal over the temporal frequency domain. The 3D sequence allows for in-plane radial sampling with arbitrary sampling orders. Fig. 2B illustrates the stack-of-stars trajectory, where the angles of the radial spokes are ordered using the golden-angle scheme. The k_x - k_y plane was acquired along radial spokes and with Cartesian sampling along the k_z plane. The sequence was implemented in standard mode – where the echo-time is shifted from image to image – and in interleaved mode – where echo time is varied from line to line (i.e., projection to projection). In addition, a DC navigator signal is acquired after balancing all imaging gradients. This signal can be used for respiratory gating.

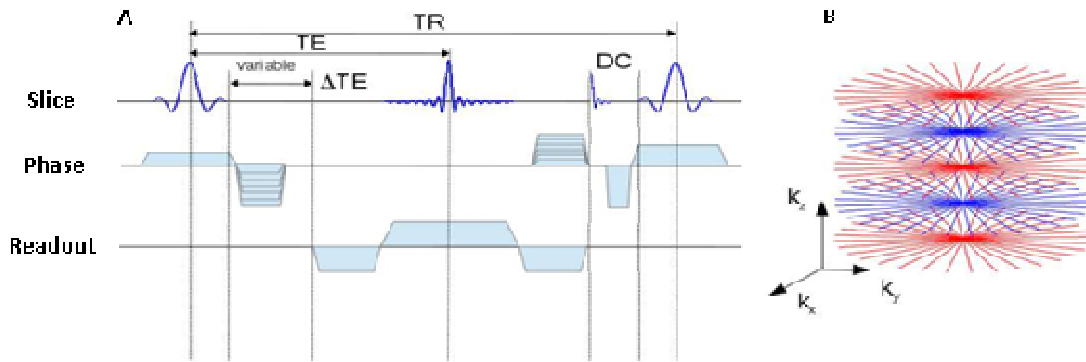


FIG. 2. (A) Schematic of the modified bSSFP sequence allowing for variable echo times (TE) at constant repetition time (TR). The 3D sequence allows for in-plane radial sampling with arbitrary sampling orders. The sequence has been implemented in standard mode, where the echo-time is shifted from image to image and in interleaved mode, where echo time is varied from line to line (i.e., projection to projection). In addition, a DC navigator signal is acquired after balancing all imaging gradients. This signal can be used for respiratory gating. (B) The k -space trajectory following a stack-of-stars trajectory.

The data is acquired by sampling all lines for the first golden angle in all partitions (all phase-encoding steps along the SLICE direction), then sampling all lines with the second golden angle (Fig. 1). This technique preserved the motion robustness of radial sampling and reduced the motion sensitivity, which leads to high data consistency within the spoke stacks.

Experiments were carried out on a 3.0T clinical scanner using the following imaging parameters: Number of projections =1500, number of partition = 28, TR = 4.0 ms, flip angle = 40° , FOV= 400×400 mm², radial readout points = 256 and TEs of $TE_1 = 1.6$, $TE_2 = 2.0$

and $TE_3 = 2.4$ ms. Signals within each partition were used to generate images at different TEs using non-uniform fast Fourier transform (NUFFT) gridding [7]. Finally, according to Ababneh et al. [22], fat-water separation was captured frame-by-frame and separation was achieved for all reconstructed partitions. All the acquired data was reconstructed offline using a MatLab software package (Math Works, Natick, MA). In this work, we integrated the fat-water separation method used in [22] with the 3D radial stack-of-stars technique during free-breathing abdominal imaging. Results were obtained *in-vivo* at 3T for the abdomen.

Results

The experiments were performed on a 3.0T clinical MRI scanner (Siemens, Erlangen, Germany) using a 32 spinal coil positioned around the mid-portion of the body and body array, by employing the modified 3D radial TrueFISP pulse sequence. Fig. 1 shows the stack-of-stars sampling pattern, where data is acquired by sampling all lines for the first golden angle in all partitions, then the second lines, ... and so on. The spokes are approximately uniformly distributed and each spoke represents one readout.

Fig. 2A is the schematic diagram of the modified sequence used in this work and Fig. 2B illustrates all of the partitions in the stack-of-stars technique.

Phantoms are simple tools used to evaluate imaging experiments. They are important, because they provide reproducible and accurate results and offer a convenient test bed for developments related to *in-vivo* imaging. The phantom contains two tubes with water and oil to provide a fat signal. Fig. 3 depicts a single time frame on a 3T clinical MRI scanner acquired with the static phantom containing water and oil (fat). Calculated water and fat images are also shown.

Fig. 4 shows one image acquired at 3T with a healthy volunteer, where both fat and water are clear before the separation process. Fig. 5 shows calculated fat and water data acquired for one partition on a healthy volunteer. Water-only and fat-only results from one phase (out of 4) are shown in (a) and (b), respectively.

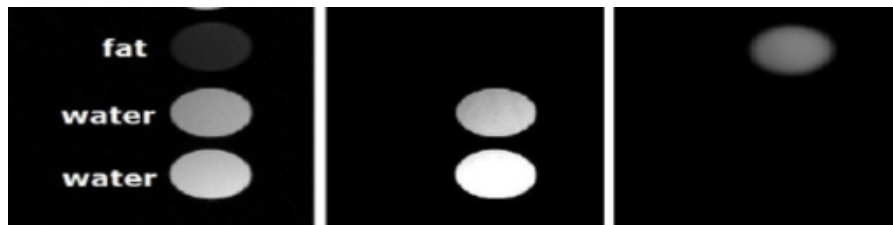


FIG. 3. Phantom experiments. Separation of multiple species (water and fat) out of one experiment with dynamic change of echo time from projection to projection. The method allows for perfect discrimination of the two species.

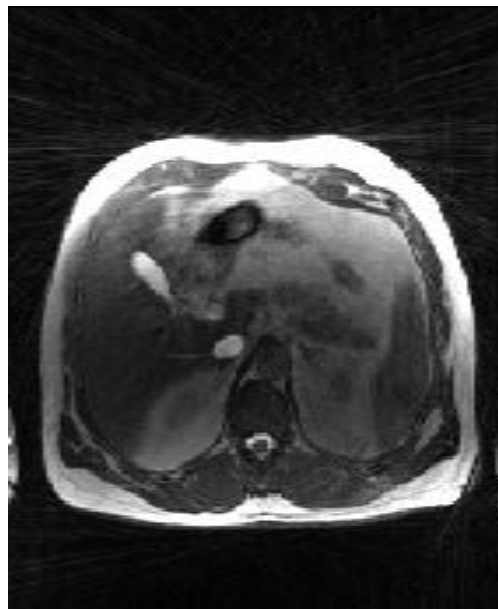


FIG. 4. One image acquired at 3T with a healthy volunteer, showing both fat and water before the separation process.

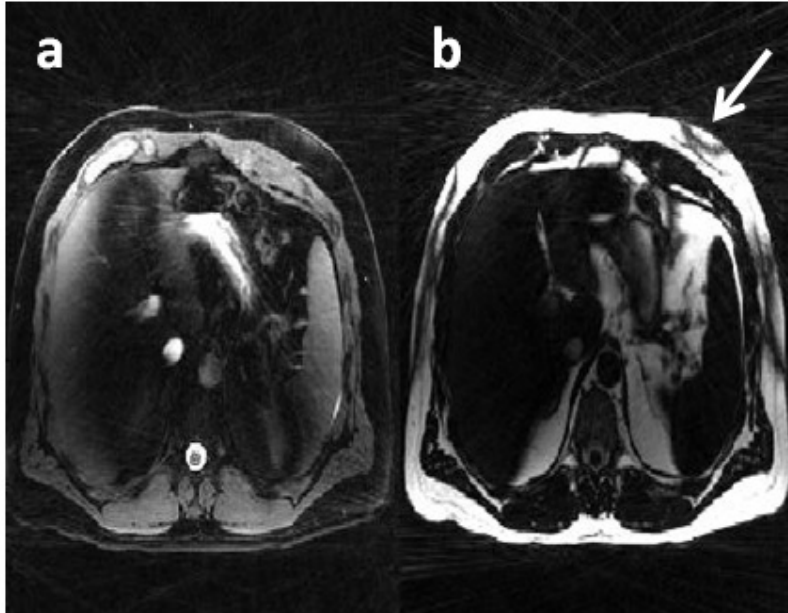


FIG. 5. The calculated water (a) and fat (b).

Discussion and Conclusion

This study presented a robust approach to separate fat and water signals using stack-of-stars 3D radial acquisition combined with non-uniform fast Fourier transform (NUFFT) gridding of different respiratory phases in free breathing. This technique reduces blurring artifacts caused by respiratory motion and enhances the image resolution. Compared to a 3D Cartesian acquisition and Dixon-RAVE [25-27], fat-water separation for free breathing abdominal imaging using 3D SOS has given promising results. Also, to show the advantage of this approach, abdominal imaging was performed in a healthy volunteer while the motion artifacts are inherently reduced. In terms of volume coverage, using the three-dimensional (3D) stack-of-stars trajectory might be advantageous compared to 2D techniques.

Phantom experiments were used, especially at the beginning of the project, to confirm a successful pulse sequence development and to validate the method used to separate fat and water. The images in Fig. 3 show an excellent separation of the two components in the static water-oil phantom.

This paper demonstrated the feasibility of 3D free breathing abdominal imaging using stack-of-stars trajectory. The phantom studies were performed to show that execution of the sequence is a function of golden angle and to evaluate imaging experiments.

The images suffer from banding artifacts due to off-resonance effects, which could be minimized through the use of one of the known methods. Our study results indicate that 3D TrueFISP with radial acquisition during free breathing is feasible for abdominal MRI studies. The results also demonstrate that even small variations in TE (0.4 ms) were sufficient to separate fat and water in dynamic objects. In conclusion, the approach was tested in time-resolved abdominal imaging. Good separation without streaking artifacts or blurring due to respiratory motion was obtained in all studied cases. The concept has been demonstrated in 3D. The 3D radial stack-of-stars TrueFISP sequence was modified by changing the echo time TE from projection to projection, to force fat signals to behave in a conspicuous manner over time, so that they can be detected and separated from water signals through temporal processing.

The radial stack-of-stars k-space trajectory is ideally suited for free breathing imaging, because it can tolerate motion better than conventional Cartesian trajectories. A major pitfall of 3D radial stack-of-stars TrueFISP imaging is its high sensitivity to magnetic field inhomogeneities (off-resonances). This could potentially lead to signal voids and unsuccessful fat-water separation. In 2D techniques, these artifacts can be minimized or avoided by appropriate shimming of the magnetic field

within the slice of interest. However, appropriate shimming of a larger volume (such as in 3D) is much more difficult to achieve. The resulting banding artifacts are clearly visible in all slices and are indicated by the white arrow in Fig. 3.

In conclusion, this study demonstrated that the 3D radial stack-of-stars TrueFISP imaging approach can be used to obtain high spatial and temporal resolutions for free breathing abdominal imaging. Moreover, it could be a promising approach for clinical imaging applications that require fat-water separation of different respiratory phases in free breathing. Future work will focus on applying the method

to self-gated 3D radial imaging for robust fat-water separation in the abdomen.

Acknowledgements

Thanks are due to the Deutsche Forschungsgemeinschaft DFG BR 4356/2-1 for funding, as well as to SIEMENS, Healthcare Sector, Erlangen, Germany.

Fat-water-separated DCE imaging with high temporal and spatial resolution is possible with DCE-Dixon-RAVE. The Dixon-RAVE framework promises high value for clinical imaging applications that require fat/water separation.

References:

- [1] Riederer, S.J., Tasciyan, T., Farzaneh, F., Lee, J.N., Wright, R.C. and Herfkens, R.J., *Magn. Reson. Med.*, 8 (1988) 1.
- [2] Vaals, J.J., Brummer, M.E., Dixon, W.T. et al., *J. Magn. Reson. Imaging*, 3 (1993) 671.
- [3] Glover et al., *MRM*, 18 (1991) 371.
- [4] Seiberlich, N., Ehses, P., Duerk, J., Gilkeson, R. and Griswold, M., *Magn. Reson. Med.*, 65(2) (2011) 492.
- [5] Rosenfeld, D., *Magn. Reson. Med.*, 48(1) (2002) 193.
- [6] Pipe, J.G. and Menon, P., *Magn. Reson. Med.*, 41(1) (1999) 179.
- [7] Fessler, J., *IEEE Trans. Med.*, 51(2) (2003) 560.
- [8] Xiang et al., *JMRI*, 7 (1997) 1002.
- [9] Reeder et al., *MRM*, 51 (2004) 35.
- [10] Glover, G.H. and Schneider, E., *Magn. Reson. Med.*, 18 (1991) 371.
- [11] Larson, A.C. and Simonetti, O.P., *Magn. Reson. Med.*, 46 (2001) 1059.
- [12] Schaeffter, R., Weiss, S., Eggers, H. and Rasche, V., *Magn. Reson. Med.*, 46 (2001) 1238.
- [13] Peters, D.C., Epstein, F.H. and McVeigh, E.R., *Magn. Reson. Med.*, 45 (2001) 562.
- [14] Barger, A.V., Grist, R.M., Block, W.F. and Mistretta, C.A., *Magn. Reson. Med.*, 44 (2000) 821.
- [15] Glover, G.H. and Pauly, J.M., *Magn. Reson. Med.*, 28 (1992) 275.
- [16] Altbach, M.I., Outwater, E.K., Trouard, T.P., Krupinski, E.A., Theilmann, R.J., Stopeck, A.T., Kono, M. and Gmitro, A.F., *J. Magn. Reson. Imaging*, 16 (2002) 179.
- [17] Katoh, M., Spuentrup, E., Buecker, A., Manning, W.J., Guenther, R.W. and Botnar, R.M., *J. Magn. Reson. Imaging*, 23 (2006) 757.
- [18] Trouard, T.P., Sabharwal, Y., Altbach, M.I. and Gmitro, A.F., *J. Magn. Reson. Imaging*, 6 (1996) 925.
- [19] Chandarana, H., Block, T.K., Rosenkrantz, A.B. et al., *Invest. Radiol.*, 46 (2011) 648.
- [20] Azevedo, R.M., de Campos, R.O., Ramalho, M. et al., *AJR Am. J. Roentgenol.*, 197 (2011) 650.
- [21] Chen, L., Adluru, G., Schabel, M.C., McGann, C.J. and Dibella, E.V., *Med. Phys.*, 39(8) (2012) 5204.
- [22] Ababneh, R.S., Madore, B. and Jing, *JMRI*, 32 (2010) 962.
- [23] Winkelmann, S., Schaeffter, T., Koehler, T., Eggers, H. and Doessel, O., *IEEE T. Med. Imaging*, 26 (2007) 68.
- [24] Kai, T.B., Hersh, C., Sarah, M., Mary, B., Tom, M., Girish, F., Mari, H., Robert, G., Christian, G., Berthold, K. and Daniel K., *JKSMRM*, 18(2) (2014) 87.
- [25] Thomas, B., Li, F., Daniel, K.S., Hersh, C. and Kai, T., *Magn. Reson. Med.*, 76(3) (2016) 1522.
- [26] Ababneh, R.S., Benkertb, T. and Breuerb, F., *Jordan J. Phys.*, 9(2) (2016) 103.
- [27] Chen, L., Adluru, G., Edward, M. and Dibella, V., *Med. Phys.*, 39(8) (2012) 5204.

Jordan Journal of Physics

ARTICLE

Assessment of Natural Radioactive Concentration Levels in the Oil Drilling Wells in Erbil Governorate Blocks

Ahmed I. Samad^a, Ali H. Ahmed^a and Saman K. Ezzulddin^b

^a Department of Physics, Faculty of Science, Salahaddin University, Erbil, Iraq.

^b Department of Environmental Science, Faculty of Science, Salahaddin University, Erbil, Iraq.

Received on: 7/10/2016;

Accepted on: 24/1/2017

Abstract: The activity concentrations of ²²⁶Ra, ²³²Th and ⁴⁰K in the core samples obtained from Erbil oil blocks have been measured by using NaI(Tl) gamma ray spectrometry. Radiological hazard indices were evaluated from the activity concentrations of these radionuclides in order to estimate health effects of the exposure of the public to radiation at the studied area. The calculated Radium equivalent activity (Ra_{eq}) varied from (33.48) to (321.13) Bq.kg⁻¹ with a mean value of (127.50) Bq.kg⁻¹. The values of annual gonadal equivalent doses (AGED) indicated 57.89% exceeding the limit of the maximum contamination level. The measured absorbed dose rate (D) values ranged from (16.17) to (140.43) nGy/h, with a mean value of (56.95) nGy/h in the oil field, which were 36.8 % higher than the international recommended value of 60 nGy/h [11]. Representative level index, I_r , for all the samples varied from (0.25 to 2.23), with a mean value of (0.90). The external hazard index (H_{ex}) varied from (0.09 to 0.87) with a mean value of (0.34) and the internal hazard index (H_{in}) ranged from (0.18 to 2.17), with a mean value of (0.91). The calculated annual effective dose equivalent values were 42% higher than the recommended value of (0.29). On the other hand, the values of ELCR in all the samples were higher than the maximum contamination level of (0.29). The measured values of outdoor and indoor AEDE varied from (0.02 to 0.18) mSv/y and from (0.05 to 0.69) mSv/y, with mean values of (0.07) and (0.28) mSv/y for outdoor and indoor effective doses, respectively, which were all below the maximum contamination level of (1) mSv/y.

Keywords: Radioactivity, Hazard indices, NaI(Tl) detector, Oil field.

Introduction

Human beings and their surroundings are continuously exposed to different types of ionizing radiation from naturally occurring radioactive materials (NORM), mainly Uranium U, Thorium Th, Potassium ⁴⁰K and radionuclides produced by human activities [1]. The natural sources of radiation are commonly distributed in all places of the earth crust. On the other hand, man-made sources are generally regional and influence just a small portion of the people [2].

In the petroleum industry, naturally occurring radioactive materials can be generated along their production. NORM may be observed in

several geological structures and can be delivered to the earth surface when oil/gas wells are drilled and constructed. Later, these materials may accumulate at the surface in the form of scales and sludge as well as inside equipment used for processing and drilling wells. In addition, they may accumulate in salt wells and sediments inside tanks or basins.

It is lately understood that more than 109 tons of naturally occurring radioactive material (NORM) wastes are produced from different sources all over the world each year. The value of NORM wastes collected during the years is

higher than (1011 tons.m^{-3}). About (1.8 tons.m^{-3}) of NORM wastes are formed by oil and gas industry alone. There are appraisals that only one well can produce about (2.3 tons.m^{-3}) of sludge, mud and scales every year [3].

Gas and oil production is an important industry in Iraq in terms of economy. Important basins in the world contain different types of rock. The northern part of Iraq is characterized by containing more than one bed rock type, including: Kurra Chine, Najmah, Singar, Sargelu, Butmah, Balambo, Naokelekn, Qamchaqa and Sarmord [3]. These bedrocks belong to the Cretaceous-Tertiary sources [1, 2]. Gas and oil basins are distributed between Cretaceous and Tertiary bedrocks [4].

The aim of this paper is the measurement of natural radioactivity level in Erbil oil field as a part of North Iraq. This will confirm a baseline map of natural radioactivity concentration levels in Erbil oil field and determine the absorbed dose rate (D), the radium equivalent activity (R_{acq}), the external hazard index (H_{ex}), the internal hazard index (H_{in}), the annual effective dose rate (AEDE) and Gamma radiation index

(I_{γ}) for workers who live inside the limits of the Erbil oil field (Oryx Oil Company).

Area of Study

Area of study is located between latitudes $36^{\circ} 02'$ and $36^{\circ} 25'$ N and longitudes $43^{\circ} 27'$ and $43^{\circ} 49'$ E as shown in Fig. 1.

It is situated within the foothill zone of the zagros fold and thrust belt. Tectonically, it was generated and progressed between the Eurasian and Arabian plates as a consequence of various stages of collision. The main geological structure of this area varies spanning from Bakhtiary (Tertiary), Adaiyah, Alan Halite, Baluti (Triassic), ... etc. formations, as shown in Table 1 [6]. The major river running to the area of study is the Grater Zap as shown in Fig. 2.

Generally, the climate of the area extends comparable to some other parts of Iraqi Kurdistan region, being semi-arid with obvious influence of the Mediterranean Sea climate on the northeastern and northern parts, which is characterized by dry and hot summer season and cold and wet winter season with rainfall of about 200mm per annum and relative humidity ranging from (46 %) to (48%) [7].

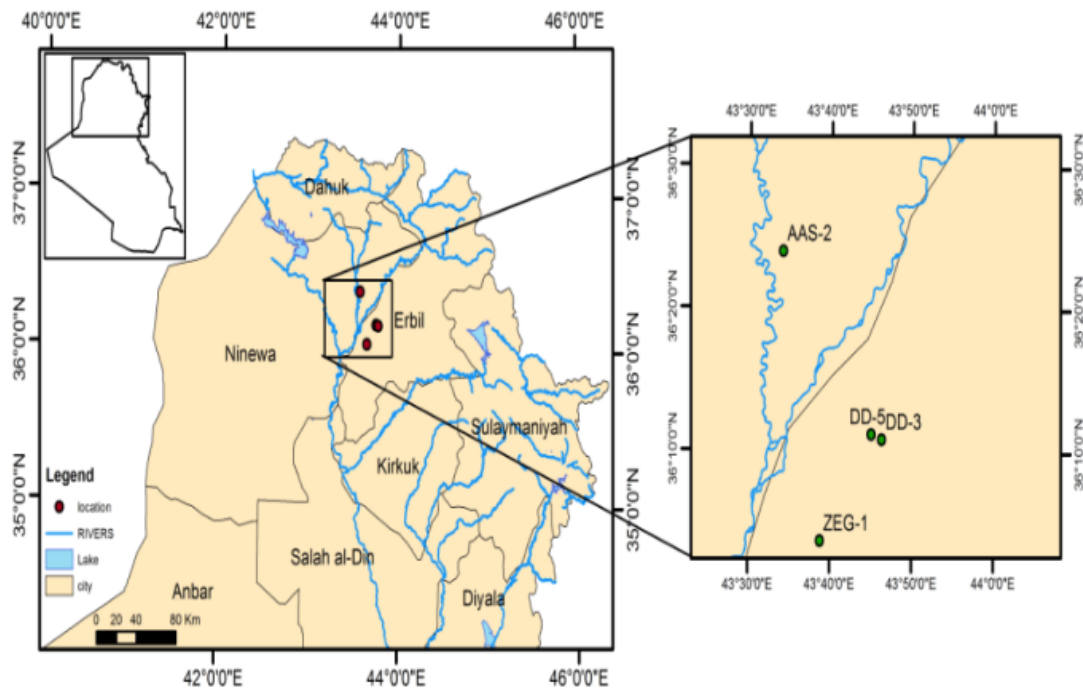


FIG. 1. Map of sample side.

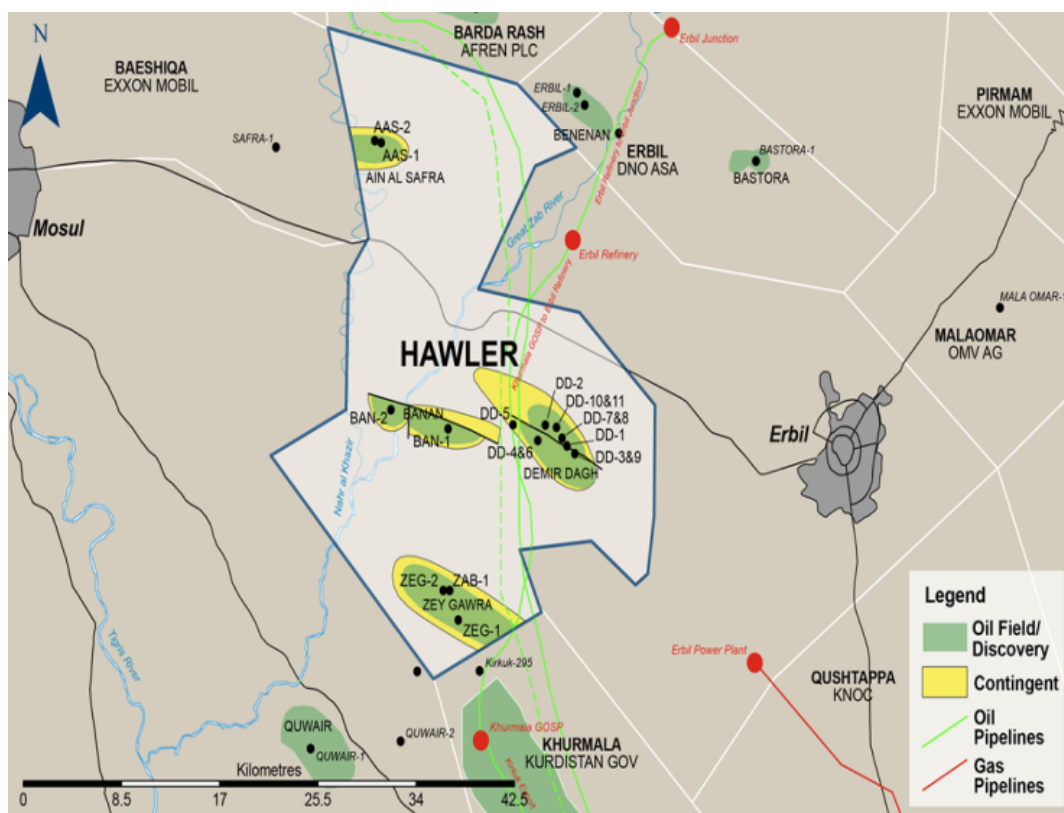


FIG. 2. Map of the oil field.

 TABLE 1. Activity concentrations of ^{226}Ra , ^{232}Th and ^{40}K in samples collected from four sites: DD-3, DD-5, AAS-2 and ZEG-1 in Erbil oil fields.

Sample name	Sample Code	Depth/ m	C ^{226}Ra (Bq.kg $^{-1}$)	C ^{232}Th (Bq.kg $^{-1}$)	C ^{40}K (Bq.kg $^{-1}$)
Adaiyah	S1	2795-3785	37.21	48.99	42.65
Alan Halite	S2	2360-3635	18.67	33.67	45.76
Bakhtiary	S3	65-230	26.63	62.42	447.6
Baluti	S4	3115-4180	38.91	62.55	450.7
Butmah	S5	2990-3920	39.48	67.28	502.3
Geraus	S6	670-1150	24.02	36.5	56.11
Kolosh	S7	1090-1480	12.35	5.75	167.50
Kometan	S8	1320-1810	78.96	118.90	33.33
Kurra Chine	S9	3200-4390	39.06	63.03	316.70
lower Fars	S10	460-890	13.03	28.65	238.40
Sarmord	S11	1480-2115	30.35	44.77	238.80
Mus	S12	2710-3670	35.51	33.36	292.70
Najmah	S13	2030-2690	17.74	15.59	44.38
Naokelekn	S14	2500-3190	72.71	116.4	73.60
Pilaspi	S15	550-1040	28	49.36	3.71
Qamchaqa	S16	1400-2080	22.78	41.22	44.69
Shiranish	S17	1270-1745	11.77	7.72	247.10
Singar	S18	825-1245	40.74	42.06	99.56
Surgelu	S19	2555-3240	91.31	153.8	128.4
Range			11.77-91.31	5.75-153.80	3.71-502.30
Mean			35.75	54.32	182.84
S.D.			22.50	38.47	158.73
World Standard			35	30	400

Materials and Methods

Sampling

In order to assess the natural radioactivity levels, about 20 core samples with cylindrical shape from four different drilling wells in the Erbil oil field have been collected, including (DD-3 and DD-5) originating from Demir Dagh block, (ZEG-1) originating from Zey Gawra block and (AAS-2) originating from Ain Al

Safra block south of Erbil Governorate in Iraq according to the geological formations with different depths ranging from (65) to (4180) m as shown in Fig. 3. For each oil well, 20 samples were taken from different formations as shown in Table 1.

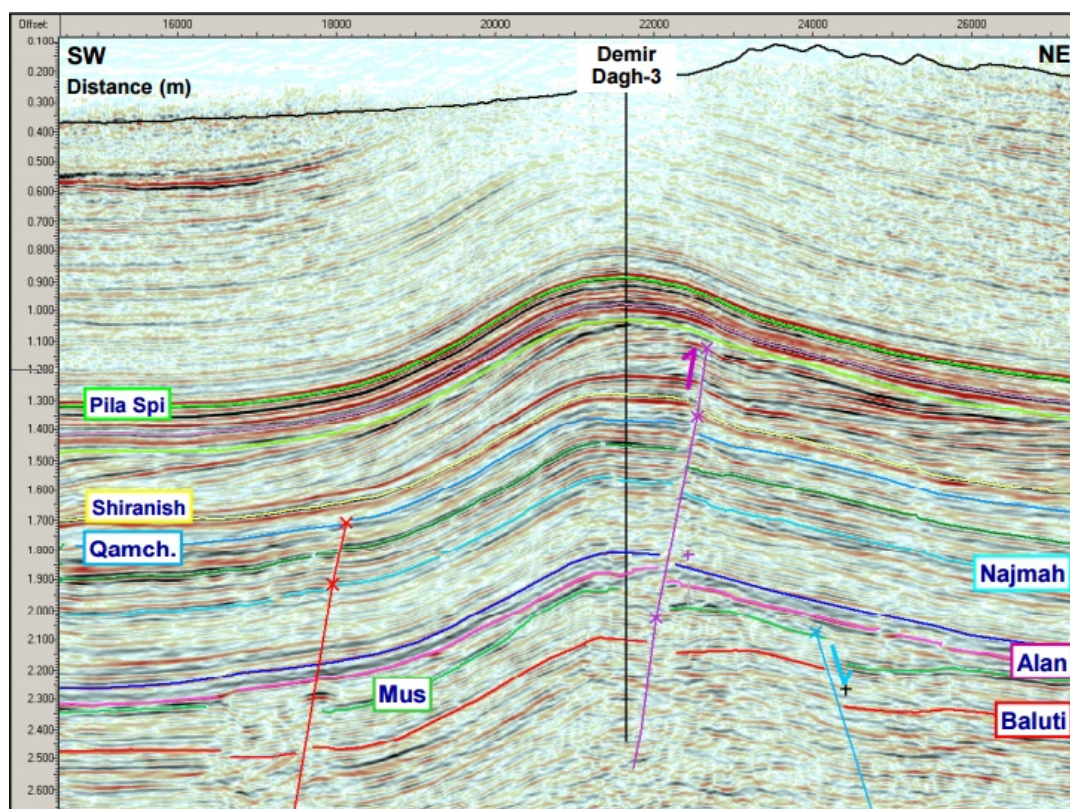


FIG. 3. Seismic section across Demir Dagh structure showing drilling oil well (DD3). (Oryx Oil Company).

The samples were crushed, dried for 24 hours in an oven at 110°C until going up to constant weight. In order to get homogenized samples, they were ground and passed through a mesh with a size of 2mm. The crushed and meshed samples were poured into a Marinelli beaker, sealed well to block radon gas leakage and stored for one month to ensure that radon and its daughters achieve a secular equilibrium before counting with NaI(Tl) scintillation detector [5].

Counting and Spectra

The activity concentrations of ^{226}Ra , ^{232}Th and ^{40}K radionuclides in the samples were measured by a gamma ray spectrometer, SILENA (Model No. 3S3). This system had an NaI(Tl) detector of

(3×3) inch, connected to a multi-channel analyzer (512 channels) and analytical CASSY software. To reduce background radiation, the detector was surrounded by a cylindrical lead shield.

The measuring time for each sample was 21600 s. Energy calibration of the detector was performed by using ^{226}Ra standard source. The efficiency calibration was performed using ^{152}Eu , ^{137}Cs and ^{60}Co standard sources. The energy resolution of the detector is 7.4% for ^{137}Cs , at the energy of 662 keV. For the detection of ^{226}Ra , ^{232}Th and ^{40}K radionuclides, we used the line energy of 352keV, 583keV and 1461keV, respectively, as shown in Fig. 4.

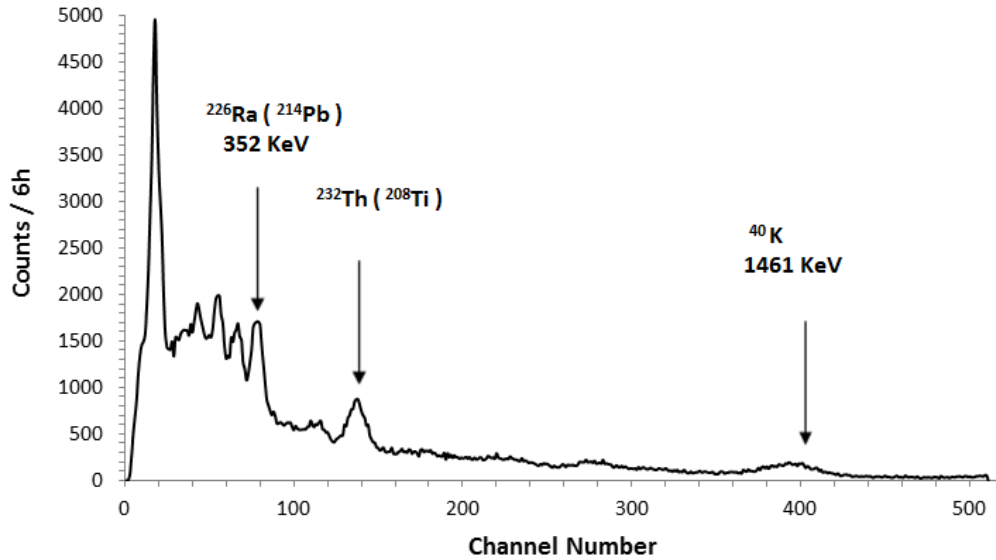


FIG. 4. The net gamma ray spectrum of Surgelu sample.

Activity Concentrations

The activity concentrations of the radionuclides in the samples were calculated using the following equation [8]:

$$A = \frac{C}{m_s \cdot \varepsilon \cdot p_\gamma} \quad (1)$$

where: $A(\text{Bq} \cdot \text{kg}^{-1})$ is the specific activity of each radionuclide, C is the net count rate of the nuclide ($\text{counts} \cdot \text{s}^{-1}$), ε is the detector efficiency of the specific γ -ray, P_γ is the absolute transition probability of the specific γ -ray and m_s is the mass of the sample (kg).

Estimation of the Radiological Hazard Indices

The activity concentrations of ^{226}Ra , ^{232}Th and ^{40}K were used to measure the radiological hazard indices concerning the radiation exposure originating from the regional environment.

Radium Equivalent Index

Radium equivalent (Ra_{eq}) index in $\text{Bq} \cdot \text{kg}^{-1}$ is a suitable index to match the specific activities of samples consisting of different concentrations of ^{226}Ra , ^{232}Th and ^{40}K . It was defined with the assumption that 10 Bq/kg of ^{226}Ra , 7 Bq/kg of ^{232}Th and 130 Bq/kg of ^{40}K produce the same gamma dose rate. It was measured by using the following relation [9]:

$$\text{Ra}_{\text{eq}} = C_{\text{Ra}} + 1.43C_{\text{Th}} + 0.077C_{\text{K}} \quad (2)$$

where C_{Ra} , C_{Th} and C_{K} are the activity concentrations of ^{226}Ra , ^{232}Th and ^{40}K , respectively.

Annual Gonadal Equivalent Dose (AGED)

Annual Gonadal Equivalent Dose (AGED) is a measure of the hazard to sensitive cells, like bone marrow, surface cells and gonads due to exposure to a certain level of radiation for particular activity concentrations of ^{226}Ra , ^{232}Th and ^{40}K . AGED is measured by using the following equation [10]:

$$\text{AGED}(\text{Sv/y}) = 3.09C_{\text{Ra}} + 4.18C_{\text{Th}} + 0.314C_{\text{K}} \quad (3)$$

Absorbed Dose Rate (D)

The dose rate due to the concentrations of the radionuclides in the samples was used to measure the radiological risk originating from external exposure to radiation arising from naturally occurring radionuclides in the human environment. It was calculated by using the following equation [11]:

$$D(\text{nGy/h}) = 0.462C_{\text{Ra}} + 0.604C_{\text{Th}} + 0.0417C_{\text{K}} \quad (4)$$

External Hazard Index (H_{ex})

The external hazard index, H_{ex} , was widely used to estimate the indoor radiation dose rate due to external exposure to gamma radiation arising from natural occurring radioactive substances in the oil field by using the following equation [12]:

$$H_{\text{ex}} = C_{\text{Ra}}/370 + C_{\text{Th}}/259 + C_{\text{K}}/4810 \quad (5)$$

Internal Hazard Index (H_{in})

The internal hazard index, (H_{in}), was commonly used to assess the internal radiation exposure of humans due to ^{222}Rn and its progenies. It is given by using the following expression [13]:

$$H_{in} = C_{\text{Ra}}/185 + C_{\text{Th}}/259 + C_{\text{K}}/4810 \quad (6)$$

Gamma Radiation Representative Level Index (I_{γ})

Representative level index is used to assess gamma radiation related with the natural radionuclides in the samples. The value of (I_{γ}) must be smaller than unity with respect to the insignificant radiation risk. It was measured by using the following equation [14]:

$$(I_{\gamma}) = C_{\text{Ra}}/150 + C_{\text{Th}}/100 + C_{\text{K}}/1500 \quad (7)$$

Annual Effective Dose Equivalent (AEDE)

Annual effective dose equivalent is the gamma dose rate received by people (adults) living in the surveyed houses in their environment. Outdoor and indoor AEDE can be calculated by using the following relations [15]:

$$\text{AEDE}_{\text{Out}}(\text{mSv/y}) = D(\text{nGy/h}) \times 8760(\text{h/y}) \times 0.7(\text{Sv/Gy}) \times 0.2 \times 10^{-6} \quad (8)$$

$$\text{AEDE}_{\text{In}}(\text{mSv/y}) = D(\text{nGy/h}) \times 8760(\text{h/y}) \times 0.7(\text{Sv/Gy}) \times 0.8 \times 10^{-6} \quad (9)$$

The conversion coefficient is 0.7 Sv/Gy from absorbed dose in air to effective dose received by adults, 0.2 for the outdoor occupancy factor and 0.8 for the indoor occupancy factor.

Excess Lifetime Cancer Risk (ELCR)

ELCR is a measure of the potential carcinogenic effects that are characterized by estimating the probability of cancer incidence in individuals for a specific lifetime from projected intakes and exposures. It was calculated by using the following equation:

$$\text{ELCR} = \text{AEDE} \times \text{DL} \times \text{RF} \quad (10)$$

where DL is the average life time (70 years) and RF is the risk factor (Sv^{-1}). ICRP 103 suggested the value of RF to be 0.06 for the public exposure (ICRP, 2007).

Results and Discussion

In this study, three naturally occurring radionuclides (^{226}Ra , ^{232}Th and ^{40}K) in Erbil oil blocks core samples have been studied by using NaI(Tl) gamma spectroscopy system. Table 1 shows the results of activity concentrations of Radium-226 ranging from (11.77 Bq.kg^{-1} in Shiranish to 91.31 Bq.kg^{-1} in Surgelu formation with a mean value of 35.75 Bq.kg^{-1} , while Th-232 ranged from 5.75 Bq.kg^{-1} in Kolosh to $153.80 \text{ Bq.kg}^{-1}$ in Surgelu formation with a mean value of 54.32 Bq.kg^{-1} and ^{40}K ranged from 3.71 Bq.kg^{-1} in Pilaspi to $502.30 \text{ Bq.kg}^{-1}$ in Butmah Formation with a mean value of $182.84 \text{ Bq.kg}^{-1}$. The activity concentration values of ^{226}Ra indicate an excess of 47% over the world standard of (35 Bq.kg^{-1}) as shown in Fig. 5. The value of activity concentration of ^{232}Th was higher by 78.9% than the world standard of (30 Bq.kg^{-1}) as shown in Fig.(5). Also, ^{40}K indicated 15.7% excess as compared to the world standard value of (400 Bq.kg^{-1}). But, the mean values for all samples were lower than the maximum contamination levels as shown in Fig. 5.

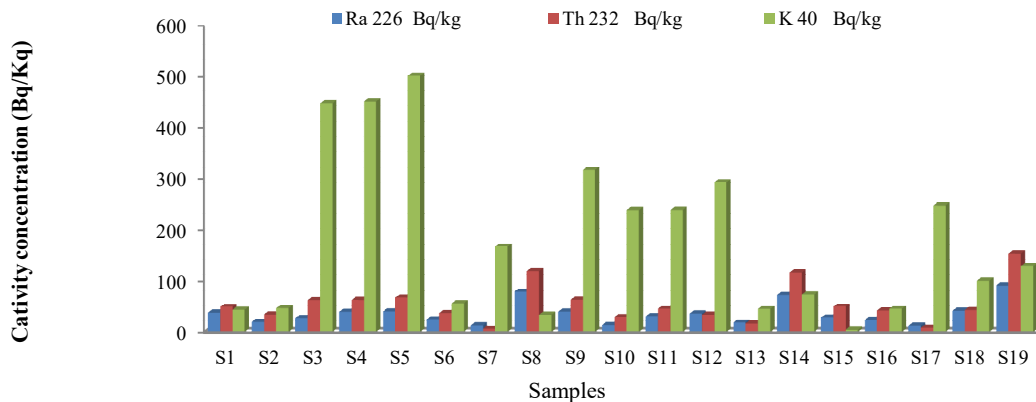


FIG. 5. Concentrations of natural radionuclides (^{226}Ra , ^{232}Th and ^{40}K) in (Bq.kg^{-1}) for each sample.

Table 2 presents the results of the radiological hazard indices. The value of radium equivalent due to the presence of ^{226}Ra , ^{232}Th and ^{40}K radionuclides in the samples ranged from (33.48) to (321.13) Bq.kg^{-1} with an overall mean value of (127.50) Bq.kg^{-1} . The values of Ra_{eq} were less than the recommended maximum level of 370 Bq.kg^{-1} in the soil. Thus, the soil in that area is

suitable for agricultural purposes [17]. The second column in Table 2 represents the average annual gonadal equivalent doses (AGED), exceeding by 57.89% the maximum contamination level limit which is 300 mSv/y in all the samples as shown in Fig. 7. These results are in good agreement with the values reported in [14].

TABLE 2. The calculated hazard indices at Erbil oil field.

S.No.	$\text{Ra}_{\text{eq}}(\text{Bq.kg}^{-1})$	AGED (mSv/y)	I_{γ}	D (nGy/h)	Hazard index		AEDE(mSv/y)		ELCR $\times 10^{-3}$	
					H_{ex}	H_{in}	AEDE _{out}	AEDE _{in}	ELCR _{out}	ELCR _{in}
S1	110.55	333.14	0.77	48.56	0.29	0.38	0.06	0.24	0.24	0.95
S2	70.34	212.80	0.49	30.87	0.19	0.29	0.04	0.15	0.15	0.60
S3	150.36	483.75	1.10	68.67	0.40	1.89	0.08	0.34	0.34	1.34
S4	163.06	523.21	1.19	74.55	0.44	1.96	0.09	0.37	0.37	1.46
S5	174.37	560.95	1.27	79.82	0.47	2.17	0.1	0.39	0.39	1.56
S6	80.53	244.41	0.56	35.48	0.22	0.35	0.04	0.17	0.17	0.69
S7	33.48	114.82	0.25	16.17	0.09	0.72	0.02	0.08	0.08	0.32
S8	251.55	751.45	1.74	109.69	0.68	0.58	0.14	0.54	0.54	2.15
S9	153.58	483.60	1.10	69.32	0.42	1.45	0.09	0.34	0.34	0.60
S10	72.36	234.88	0.53	33.27	0.20	0.1	0.04	0.16	0.16	1.34
S11	112.76	355.90	0.81	51.02	0.30	1.1	0.06	0.25	0.25	1.46
S12	105.75	341.08	0.77	48.76	0.29	1.33	0.06	0.24	0.24	1.56
S13	43.45	133.92	0.30	19.46	0.11	0.27	0.02	0.1	0.1	0.7
S14	244.83	734.34	1.70	106.97	0.66	0.70	0.13	0.53	0.52	0.32
S15	98.87	294	0.68	42.90	0.27	0.18	0.05	0.21	0.21	2.15
S16	85.17	256.72	0.59	37.29	0.23	0.30	0.05	0.18	0.18	0.73
S17	41.85	146.26	0.32	20.41	0.11	1.02	0.03	0.10	0.10	0.40
S18	108.55	332.96	0.76	48.38	0.29	0.61	0.06	0.24	0.24	0.95
S19	321.13	965.35	2.23	140.44	0.87	1.02	0.18	0.69	0.69	2.75
Mean	127.50	394.92	0.90	56.95	0.34	0.91	0.07	0.29	0.28	1.12
World Standard	370	300.00	1.00	60.00	1.00	1.00	1.00	1.00	0.29	0.29
S.D.	77.10	230.78	0.53	33.59	0.22	0.61	0.04	0.16	0.16	0.66
Max.	321.13	965.35	2.23	140.43	0.87	2.17	0.18	0.69	0.69	2.75
Min.	33.48	114.82	0.25	16.16	0.090	0.18	0.02	0.08	0.08	0.32

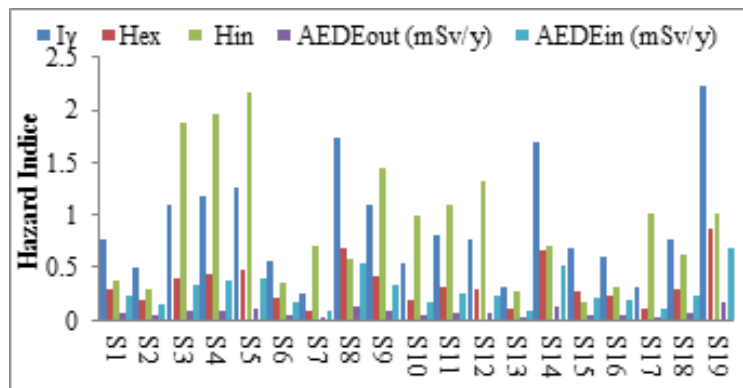


FIG. 6. The Radiological hazard indices: H_{ex} , H_{in} , I_{γ} , AEDE_{out} (mSv/y) and AEDE_{in} (mSv/y) for each sample.

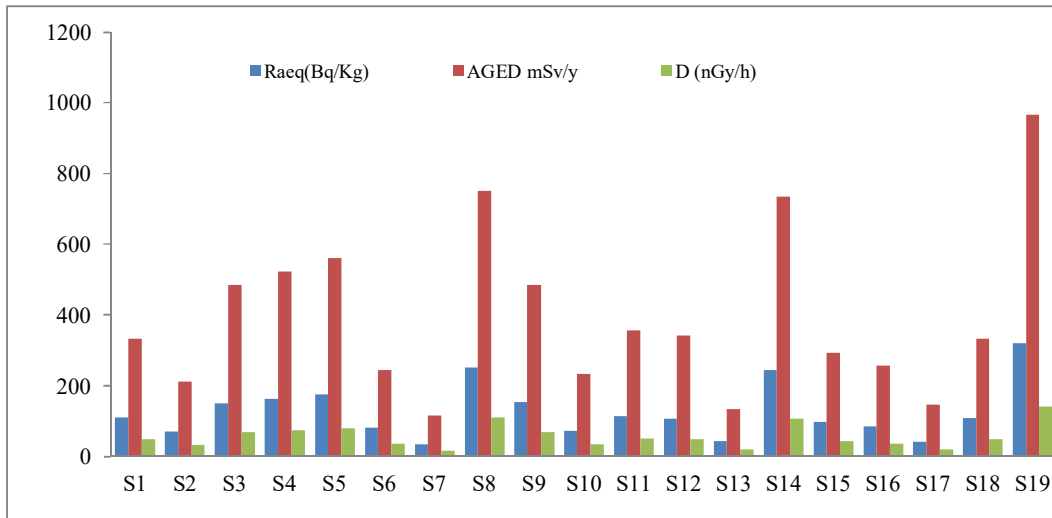


FIG. 7. Radium equivalent (Ra_{eq}), annual gonadal equivalent dose (AGED) and absorbed dose rate (D) for each sample.

The measured absorbed dose rate (D) ranged from (16.16 to 140.44) nGy/ h, with a mean value of (56.95) nGy/ h in the oil field, indicating that 36.8 % of the studied samples were with rates higher than the international recommended value of (60) nGy/h [11], while the mean value was less than that recommended level. The obtained external hazard index (H_{ex}) values ranged from (0.09) to (0.87), with a mean value of (0.34) in Erbil oil field. The measured mean value was lower than 1. The value of internal hazard index (H_{in}) varied from (0.18) to (2.7) with a mean value of (0.91). The results indicated that 42% of the studied samples were with values higher than the recommended value of (1) [11], but the mean value over all samples was lower than (1), as shown in Fig. 6.

The estimated values of I_{γ} for all the samples presented in Table 2 varied from (0.25) to (2.23) with a mean value of (0.90). The calculated values indicated that 31% of the studied samples were with values higher than the international value ($I_{\gamma} > 1$), but the mean value over all samples is lower than (1). The measured values of outdoor and indoor AEDE varied from (0.02) to (0.18) mSv/y and from (0.08) to (0.69) mSv/y, with mean values of (0.07) and (0.28) mSv/y for outdoor and indoor effective dose, respectively. The calculated values of $ELCR_{out}$ indicated that 42% of the studied samples were with values higher than the recommended value of (0.29). On the other hand, the values of $ELCR_{in}$ in all samples are higher than the maximum contamination level (0.29), as shown in Fig. 8.

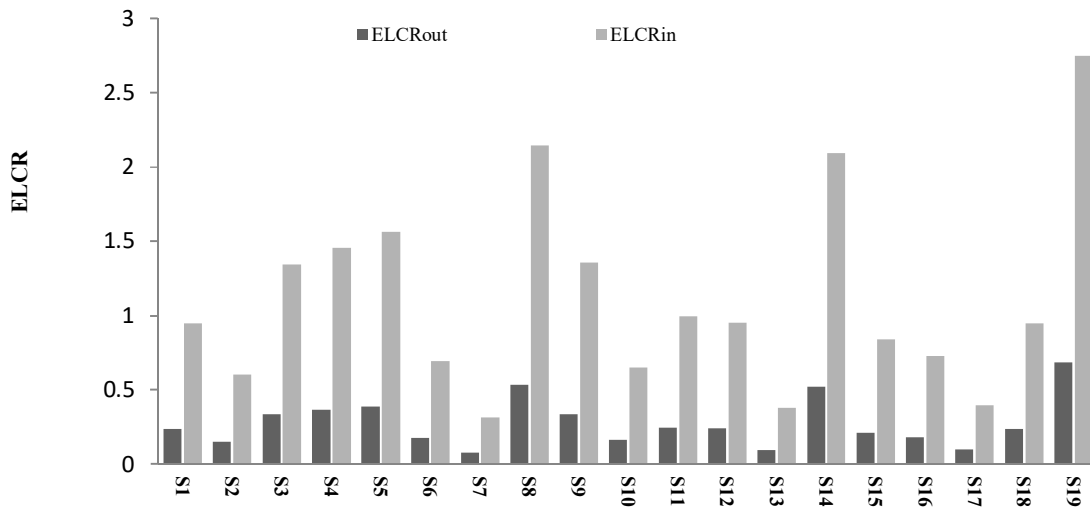


FIG. 8. Excess lifetime cancer risk for each sample.

Conclusions

The activity concentrations of ^{226}Ra and ^{232}Th radionuclides show highest values in the Surgelu sample due to its shale structure which contains high organic materials that accumulate heavy elements. Potassium-40 concentration was highest in the Butmah sample, which may refer to the high content of KCl compound in its rock structure. The evaluated radiological parameters and hazard indices show acceptable average values, except for the ELCR_{in} values which

exceed the permissible values for all samples. Although the measured hazard indices in the studied samples are lower than the permissible limits, they were still higher than the normal values. Hence, the oil and gas activities will influence negatively the radiological situation of the environment. It can be concluded that there are significant radiological hazards to the people in that area.

TABLE 3. Comparison of natural radioactivity levels in the samples to other countries.

Country	$^{40}\text{K}(\text{Bq. kg}^{-1})$	$^{226}\text{Ra}(\text{Bq. kg}^{-1})$	$^{132}\text{Th}(\text{Bq. kg}^{-1})$
Niger [8]	128.6	75.60	21.30
Yemen [18]	697.9	59.39	71.32
Cameroon [19]	186.96	34.52	16.67
Egypt [11]	320	17	18
USA [11]	370	35	40
Malaysia [11]	331	67	82
Spain [11]	470	32	33
Present work	158.73	22.50	38.47

References

- [1] United Nations Scientific Committee on the Effects of Atomic Radiation, (1988), Report to the UN General Assembly, with Annexes, United Nations.
- [2] Mettler, F.A., Sinclair, W.K., Anspaugh, L., Selby, P.B., Edington, C., Webster, E.W., Harley, J.H., Wyckoff, H.O. and Ricks, R.C., Health Phys., 58 (1990) 241.
- [3] Paschoa, A.S., "Radiological Impact Due to Oil and Gas Extraction", (Business Briefing: Exploration and Production, 2003), pp. 1-4.
- [4] Isinkaye, M.O. and Emelue, H.U., Journal of Radiation Research and Applied Sciences, 8 (2015) 459.
- [5] International Atomic Energy Agency (IAEA), A Guidebook, Technical Report Series No. 295, IAEA, Vienna (1989).
- [6] Pitman, J.K., Steinshour, D. and Lewan, M.D., GeoArabia, Gulf Petrolink, Bahrain, 9(4) (2004) 41.
- [7] Iraqi General Organization for Metrological Information, 2000. Climate Atlas of Iraq for the Years (1981-2000).
- [8] Jibiri, N.N. and Ajao, A.O., Journal of Environmental Radioactivity, 78 (2005) 105.
- [9] Beretka, J. and Mathew, P., Health Physics, 48 (1985) 87.
- [10] Avwiri, G.O., Agbalagba, E.O. and Chad-Umoreh, Y.E., Journal of Environmental Radioactivity, 109 (2012) 64.
- [11] UNSCEAR Report, United Nations Scientific Committee on the Effects of Atomic Radiation (Report to the General Assembly, with Annexes, 2000).
- [12] Hamzah, Z., Saat, A., Mashuri, N.H. and Redzuan, S.D., The Malaysian Journal of Analytical Sciences, 12(2) (2008) 419.
- [13] Cottens, E. and Radon, J. (Eds.), Proceedings of the Symposium on SRBII, Royal Society of Engineers and Industrials of Belgium, Brussels, (1990).
- [14] Ali, H., Laith, A. and Abbas, M., Journal of Radiation Research and Applied Sciences, 9 (3) (2016) 259.
- [15] UNSCEAR, (2010) Report to the UN General Assembly, with Scientific Annexes, Vol. 1 (United Nations, New York) 1-219.
- [16] Anekwe, U. and Avwiri, G., American Journal of Scientific and Industrial Research, 7(3) (2016) 50.

- [17] Shaban, H., Abd El-Hadi, K., Abd El-Bast, A., Imran, I. and Abdallah I., *Journal of Medical Physics*, 37(1) (2012) 1.
- [18] Harb, S., El-Kamel, A.H., Zahran, A.M., Abbady, A. and Ahmed, F.A., *International Journal of Recent Research in Physics and Chemical Sciences*, 1(1) (2014) 1.
- [19] Pascal, T., Thomas, B. and Robert, M., *J. Environmental Protection*, 3 (2012) 1571.

Optical and Structural Characterization of Dip Synthesized Al-B Co-doped ZnO Seeded Platforms for ZnO Nanostructures

A. A. Ahmad^a, A. M. Alsaad^a, Q. M. Al-Bataineh^a, A. A. Bani-Salameh^a,
H. M. Al-Khateeb^a and M. A. Al-Naafa^b

^aDepartment of Physical Sciences, Jordan University of Science & Technology, P.O. Box 3030, Irbid-22110, Jordan.

^bDepartment of Chemical Engineering, Ha'il University, Ha'il, Saudi Arabia.

Received on: 14/11/2016;

Accepted on: 27/2/2017

Abstract: Zinc oxide and aluminum-boron co-doped zinc oxide (Al-B:ZnO) thin films have been dip coated on glass substrates using Sol-Gel technique. The ZnO solution was prepared by using zinc acetate dihydrate (ZAD) as starting material. Ethanol and citric acid were used as solvent and solution stabilizer, respectively. Doping of Al-B was achieved by adding a proper molar ratio of aluminum nitrate ($\text{Al}(\text{NO}_3)_3 \cdot 9\text{H}_2\text{O}$) and boric acid (H_3BO_3) to the final ZnO solution. The optical properties for the films were investigated through the UV-Vis spectrophotometry technique. The transmittance of the undoped ZnO decreases while the concentration of boron increases and increases while the concentration of Al increases over the range of interest. The index of refraction was found to be between 1.73 and 2.43 for the undoped ZnO, which agrees well with that of the bulk ZnO. It increases while the B concentration increases and decreases while the concentration of Al increases. The structural properties were also investigated through XRD, SEM and EDAX measurements. The films acquired hexagonal structure after annealing. The films have been used as seeded platforms for growing ZnO nanostructures using hydrothermal technique and found to fit better for the ZnO platforms rather than the doped ones.

Keywords: Thin films, ZnO, Al-B co-doped ZnO, Sol gel process, Dip coating, Nanostructures, Optical properties, Structural properties.

PACS: 78, 81

Introduction

Zinc oxide (ZnO) thin films are considered the most important metal oxide semiconductors owing to the fact that they have unique features and a wide range of technological applications in various fields, such as solar cells, photovoltaic cells, gas sensors, light emitting devices, photocatalysts and cancer treatment [1]. They have n-type semiconducting property with large excitonic binding energy of around 60 meV and a wide band gap energy of around 3.37 eV at room temperature [2]. They have attracted much interest in the area of photo-electronic devices for high performance of light-emission properties. ZnO thin films have been deposited by various methods, such as magnetron sputtering [3, 4], metal organic chemical vapor

deposition [5-7], pulsed laser deposition [8], electrochemical deposition [6] and the sol-gel method [9, 10].

Zinc oxide plays an important role in a wide range of applications, such as microelectromechanical systems (MEMS), due to their good piezoelectric effect [11-13], transparent conducting electrodes in some devices, due to their good electrical conductivity [14], light emitting diodes, UV lasers, transparent field effect transistors and other optical coating applications [15]. ZnO films were usually doped by various doping materials in order to enhance their physical properties, including their optical and electrical characteristics. The physical properties of Al-B

co-doped ZnO thin films have different properties from ZnO thin films [3, 10, 16-18]. Boron and aluminum atoms are known by their low and high atomic numbers ($Z_B = 5$ and $Z_{Al} = 14$), respectively. They have small and large ionic (r_B^{+3} and r_{Al}^{+3}) radii (0.23 Å and 0.535 Å), respectively. Also, they possess large and low electron work functions (4.45 and 4.33 eV), respectively and high and low first ionization energies (8.298 and 5.986 eV) with $2p^1$ and $4s^2$ orbital levels, respectively [7, 19]. Comparing these values to the relevant values for Zn atom ($Z_{Zn} = 30$, r_{Zn}^{+2} radius = 0.23 Å, electron work function of 4.28 eV and first ionization energy of (9.394 eV)), one may recognize that either of the two doping elements (Al or B) will substitute Zn atom in the hexagonal platform [20, 21]. It is well known that the electron affinity for Al (≈ 42 kJ/mol) and that of B (≈ 27 kJ/mol) have larger values than that of Zn atom which has no stable negative ion state. This implies that both Al and B atoms have greater deal of affinity with O atom compared to that of Zn atom during the film growth. Aluminum has greater affinity with oxygen than boron which gives it the priority of substituting zinc with oxygen. Hence, deformed oxides are caused to appear in the films, distorting their physical properties. Post annealing treatment causes microstructural rearrangement, which improves the films' optical properties [22]. Our focus in this research was placed on optimizing the experimental conditions in order to produce ZnO films suitable for specific applications, such as photovoltaic cells, solar cells or optical coatings. The outcomes were obtained by co-doping the ZnO films with Al and B through adjusting their content ratios in order to produce the required characteristics. Our study was devoted to elaborate the effect of Al-B combination on the structural and optical properties of dip coated Al-B co-doped ZnO thin films via sol gel technique on glass substrates and treated with post annealing process. The feasibility of growing ZnO nanostructures on ZnO and Al-B co-doped ZnO seeded platforms was also investigated.

Experimental Procedure

Deposition of ZnO and Al-B Co-doped ZnO Thin Films

The glass substrates were cleaned with soap solution, rinsed with distilled water, dipped in ethanol for 15 minutes and finally dried in air. The undoped ZnO solution was prepared by

dissolving 4.38 g of zinc acetate dihydrated ($Zn(CH_3CO_2)_2 \cdot 2H_2O$ with purity of 99.5%) in 50 mL absolute ethanol (99.85%) to get 0.4 M in concentration. The solution (sol) was then mixed thoroughly using a magnetic stirrer for 50 minutes at room temperature until it turned milky (gel). The ethanolamine stabilizer of 1.7 mL was added to the solution in terms of drop by drop while stirring the solution to make it transparent. The resulting mixture was stirred for 40 minutes to get a homogeneous solution. The solution was filtered by paper-filter, 0.45 μm in dimension. The films were dip coated by dipping the substrate in the solution for 2 hours. The films were dried in oven for 15 minutes at 110 °C to evaporate the solvents and organic residues. Finally, ZnO films were annealed in air at 500 °C for 2 hours [23, 24]. Boric acid (H_3BO_3) and aluminum nitrate ($Al(NO_3)_3 \cdot 9H_2O$) were then added with the desired ratios to the undoped ZnO solution in order to prepare Al-B co-doped ZnO solution. The solution was then mixed by the magnetic stirrer for 30 minutes at room temperature to make it homogeneous. Again, the solution was then filtered by similar paper-filters. The Al-B co-doped ZnO solution was then deposited by dip coating technique for 2 hours on pre-cleaned glass substrates. The deposited Al-B co-doped ZnO films were then treated similar to the undoped ZnO film [24].

Hydrothermal Synthesis of ZnO Nanoparticles Technique

All the chemicals used in this work were of analytical reagent grade and used as received from the supplier without any further purification or post-treatment. In a typical procedure, stock solution of zinc acetate dihydrates $Zn(CH_3CO_2)_2 \cdot 2H_2O$ (5 mM) was prepared in 20 mL of ethanol under magnetic stirring. A volume of 20 mL of KOH, prepared by a percentage of 0.2 mM to 0.5 mM in ethanol, was added to the solution under stirring for 30 minutes. The solution was then transferred into a water bath and maintained at a certain temperature in the range of (65 - 82 °C) for 2-3 hours until it formed the roots of nanoparticles. The obtained ZnO nanoparticles (ZnO-NP) were washed three times with ethanol and distilled water in order to remove impurities and then dried in air at 50 °C for 24 hours [25].

Results and Discussion

Optical Properties of the Undoped and the Al-B Co-doped ZnO Thin Films

A dual channel spectrophotometer (Perkin Ellmer Lambda-9 series) was used to investigate the optical properties of the undoped and the Al-B co-doped ZnO thin films for various ratios of Al to B concentration in the solution. All the measurements were taken at room temperature. Fig. 1 shows the transmittance for the films deposited under various Al / B concentration ratios. It is clearly seen that the transmittance decreases over the whole range of interest as the concentration of B increases and increases as the concentration of Al increases. This observed fact agrees well with the findings of S. Ilican et al. [26], L. Yang et al. [27] and A. Sreedhar et al. [28]. The transmittance for the undoped ZnO (0.0% / 0.0%) film was found to almost vanish in the UV region (below 375 nm), while it increases much more than that for the Al / B doped ZnO films with 0.25% / 0.25%, 0.25% / 0.50%, 0.50% / 0.25% and 0.50% / 0.50%, respectively. The transmittance increases then abruptly near the band edge to become almost transparent in the visible region. The band gap energy (E_g), defined by the equivalent photon energy related to the average value of transmittance above the band edge and before the film turns transparent in the visible region, was found to be 3.333, 3.374, 3.369, 3.360 and 3.430 eV, respectively. As the Al and B contents were introduced to ZnO solution by small ratios (0.25% for each), no considerable changes have

been observed in the transmittance curve in the visible region. However, it increases slightly in the UV region (short dashed curve). E_g was increased to 3.374 eV compared to 3.333 eV for the undoped ZnO film. By introducing 0.50% of both Al and B contents to ZnO solution, the transmittance increases from 85% to around 90% in the visible region and increased much more in the UV region. E_g has increased to 3.430 eV accordingly. By increasing the Al content to 0.50% while fixing B at low ratio (0.25%), E_g increased to 3.360 eV, while the transmittance decreased below 75% in the visible region. However, increasing B ratio to 0.50% while fixing the Al ratio as low as 0.25% increases E_g to 3.3369 eV and the transmittance increases also to reach around 90% over the visible region. The value of the reflectance was measured by the spectrophotometry technique while using an integrated sphere to reduce the glass effect in the measurements. The argument applied to the transmittance spectra applies to the reflectance spectra as shown in Fig. 2. The reflectance for the undoped ZnO films ranges between 8% and 22% with an average of around 9% in the visible region and peaks at around 385 nm (3.222 eV). The average reflectance increases above that for the undoped ZnO as the B concentration increases to 0.25% or 0.50% while fixing the Al concentration at 25%. However, the average reflectance decreases below that of the undoped ZnO while increasing Al concentration to 25% or 50% at fixed Al concentration of 25%. All the reflectance curves acquire almost similar shape as that for the undoped spectra with varying peak positions and intensity ranges.

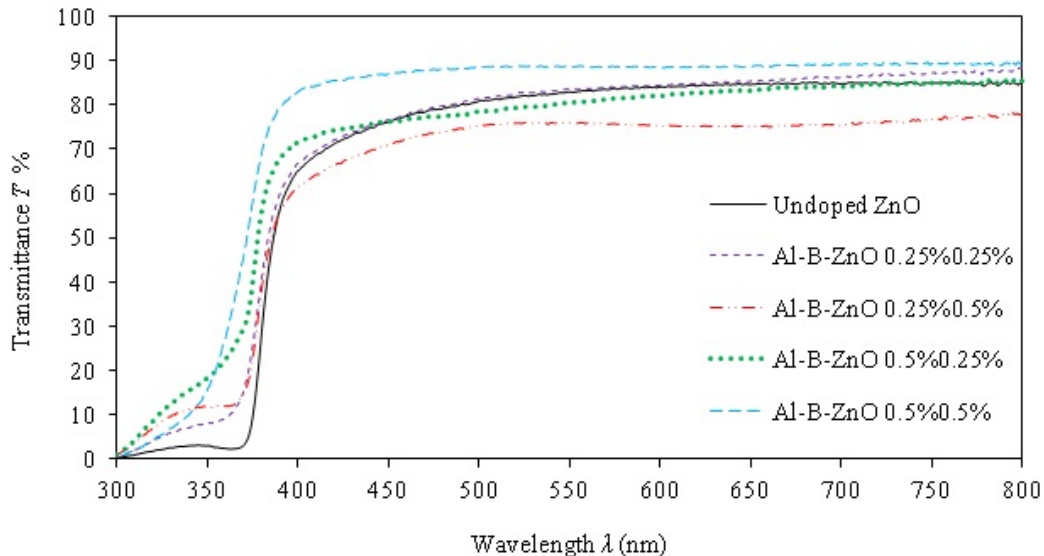


FIG. 1. The transmittance spectra of the undoped ZnO and Al-B co-doped ZnO thin films at various ratios.

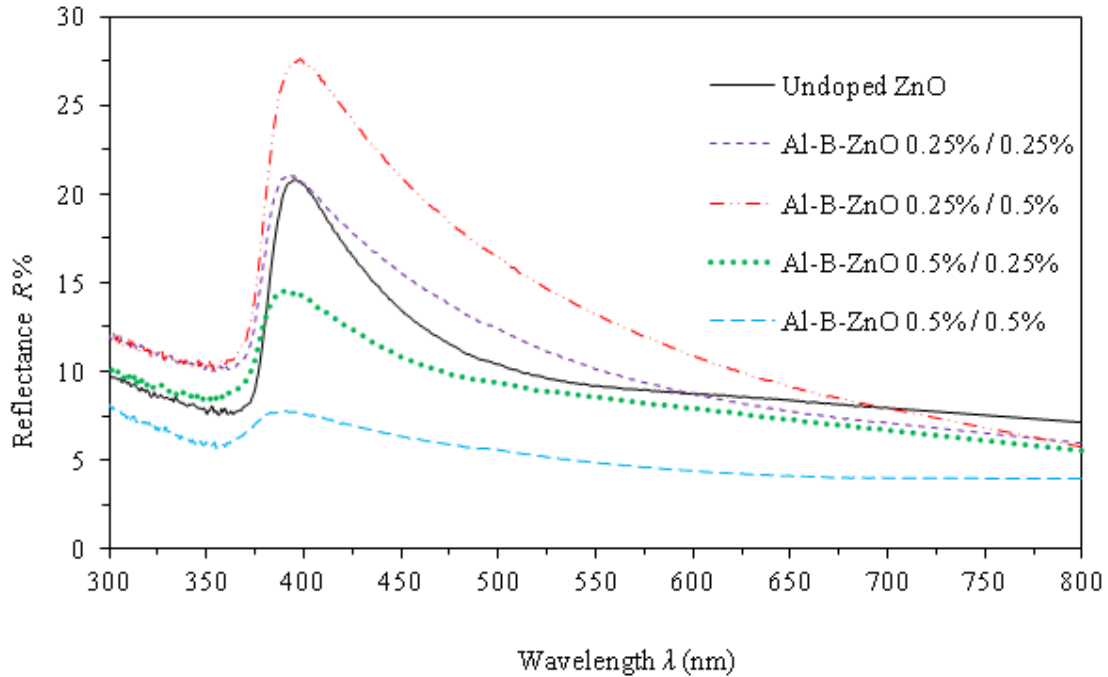


FIG. 2. The reflectance spectra of the undoped ZnO and Al-B co-doped ZnO thin films at various ratios.

In order to investigate the extinction coefficient (k) and the index of refraction (n) of the films, the average thickness was obtained to be about 500 nm by the Scanning Electron Microscopy (SEM) micrograph results. The film thickness was found by calibrated deposition rate which takes 2 hours of deposition to achieve this thickness with non-uniformity of around 2.2%. Fig. 3 shows the extinction coefficient (k) spectra for the films evaluated by $k = \alpha\lambda/4\pi$ over the range of interest, where α is the absorption coefficient [29]. The k values in the visible region increase as the B concentration increases and decrease as Al concentration increases. The curve features of k for the undoped ZnO film show a well-defined peak at around the band gap energy (at $\lambda = 368.5$ nm with equivalent $E_g = 3.365$ eV). When Al and B were introduced to the ZnO solution by 25% for each, the peak value decreased and showed no fine features. It acquires features showing that doping energy levels have been introduced to the band gap near the conduction band (short dashed curve). As the Al and B concentrations have been increased further to 50% for both dopants, the peak feature almost disappeared while the curve steepness has been increased (long dashed curve). Fixing the Al concentration low at 25% while increasing the B concentration up to 50% reduces the value of the peak while still maintaining the overall k curve (dash with two

dots) in the normal trend. However, fixing the B concentration low at 25% and increasing the Al concentration up to 50% cause the peak to decrease with lower k values in the UV region (dotted curve). The index of refraction (n) for the thin films has been evaluated from the values of the reflectance and the extinction coefficient as:

$$n = \left(\frac{1+R}{1-R} \right) + \sqrt{\left(\frac{4R}{1-R} \right)^2 - k^2}$$

[30-32]. The n value as a function of incident light wavelength is shown in Fig. 4 for all the Al-B co-coped ZnO films compared to that of the undoped ZnO film. The index of refraction for the undoped ZnO (solid line) exhibits values ranging between 1.63 and 2.43 with main peak feature appearing at the beginning of the visible region. As the Al and B concentrations were increased by 25% for both, n increased slightly in the visible region (short dashes). However, as B concentration increases to 50%, n curve increases extremely to reach its maximum value at 2.83 (long dashes with two dots). On the other hand, as Al concentration was increased to 50% while fixing B concentration at 25%, n curve decreased down below that for the undoped ZnO thin film (dotted curve) with an average value of around 1.80. In the case where Al and B contents have been increased to 50% for each, n values reduced between 1.50 and around 1.68 while losing the curve peak feature (long dashes).

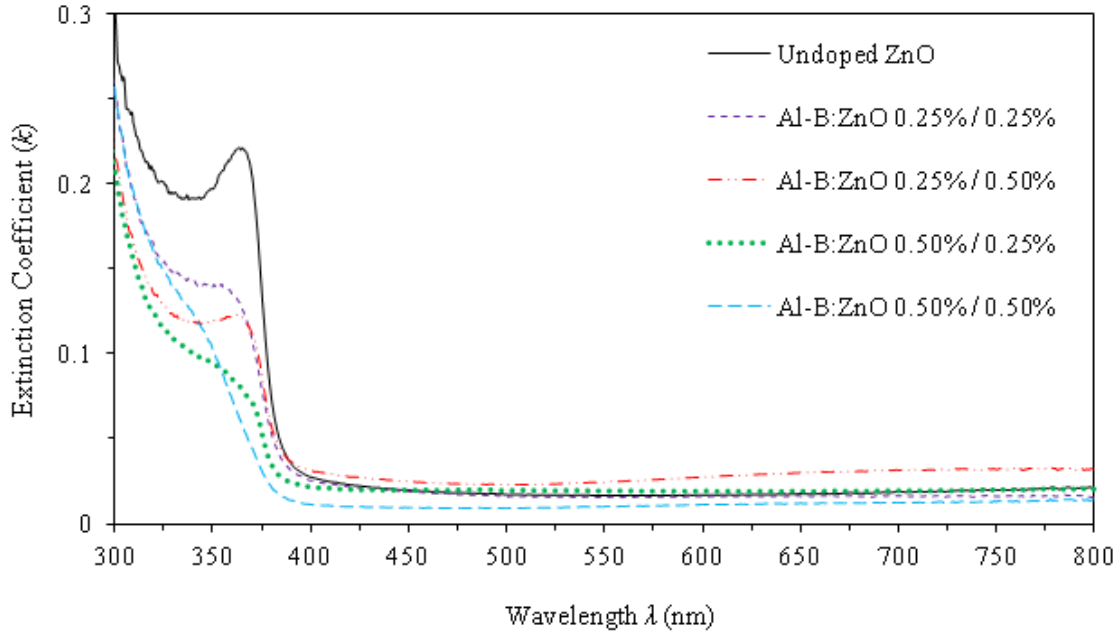


FIG. 3. The extinction coefficient (k) of undoped ZnO and Al-B co-doped ZnO thin films.

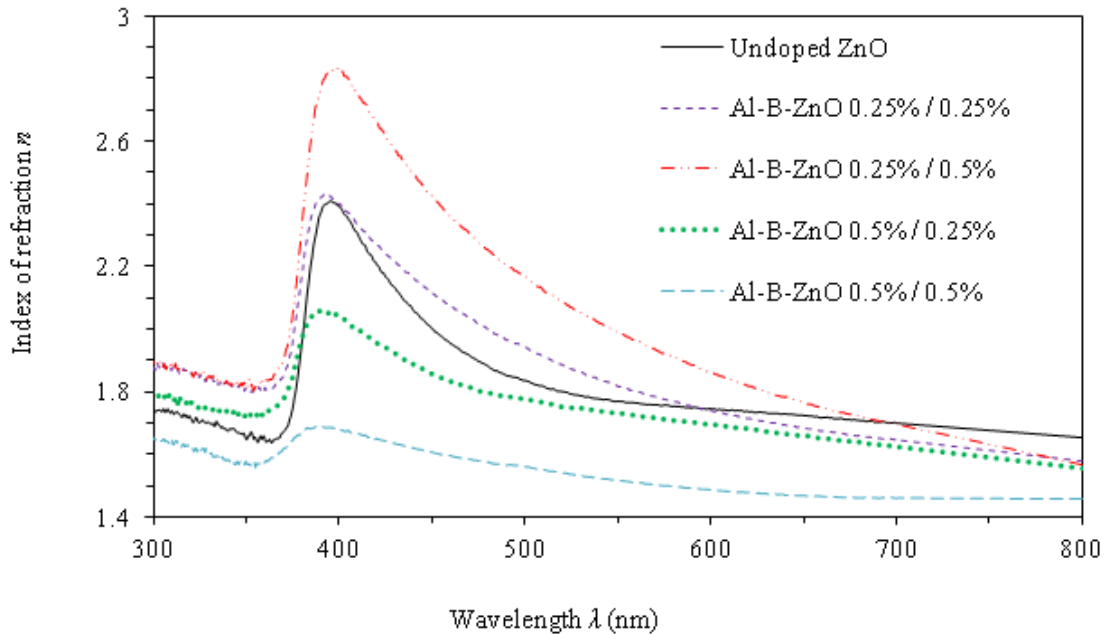


FIG. 4. The index of refraction (n) of undoped ZnO and Al-B co-doped ZnO thin films.

In order to find the film band gap energy (E_g), Tauc plots have been investigated by drawing the relationship between the incident photon energy ($h\nu$) and $(\alpha \times h\nu)^2$. The absorption coefficient α has been evaluated from the transmittance and the film thickness such that $\alpha = 1/d \ln(1/T)$. Fig. 5 shows Tauc plots for all the deposited films with various Al and B

concentrations. E_g was found by extrapolating the linear part of the relationship above the band edge along the incident photon energy axis where $E_g = h\nu$. Two main features in Tauc plot were observed while defining the band gap energy for the undoped ZnO film. One transition hub was found at a band gap energy of 3.255 eV, while the other transition feature shows the pronounced band gap energy at 3.362 eV. The

first hub feature indicates the presence of the known excitonic binding energy in ZnO near the band edge. The lower band gap energy (3.255 eV) is related to the donor's level in the pronounced optical band gap (3.362 eV) and the difference between them is related to the electron-hole pair excitonic energy (107 meV). This phenomenon has been observed in many metallic oxide semiconductors such as graphene oxides and tin oxides implanted with carbon ions in addition to ZnO due to the local atomic relaxations around the oxygen vacancies in the neutral, +1 charge and +2 charge states [33-36]. It is well known that the excitonic binding energy for pure crystalline ZnO is around 60 meV at room temperature. However, our films are polycrystalline and non-stoichiometric, which may explain the higher value of excitonic binding energy. Our values are comparable to the values given in the literature for similar deposition process. Table 1 shows all these values for all the deposited films. These features were found for the Al-B co-doped ZnO films with rather lower hub features. Given that the error in E_g is around $\pm 3.3 \times 10^{-3}$ eV, the main band gap energy found of the undoped ZnO through using the average transmittance value above the band edge was 3.362 eV as seen in Table 1. As Al and B concentrations become 0.25% for each, E_g decreases to 3.350 eV (3.374 eV from the average transmittance value), while the excitonic energy decreases to 95 meV. Fixing the Al concentration low at 0.25% and increasing the B concentration to 50%, E_g decreases to 3.340 eV (3.369 eV by the

transmittance value) and the excitonic energy decreases further to 85 meV. However, fixing the Al concentration high at 0.50% while decreasing the B concentration to 0.25%, E_g increases to 3.368 eV (3.360 eV by the transmittance value) which is around the value for the standard crystalline ZnO material (3.370 eV) [2] and the value of the excitonic binding energy becomes 118 meV. As Al and B concentrations were increased further to 0.50% for each, E_g increased to reach 3.420 eV (3.430 eV by the transmittance value) and the excitonic energy increased to 165 meV. This observation indicates that an increase in Al concentration (at fixed B value) leads to a decrease in the band gap energy, while an increase in B concentration (at fixed Al value) leads to an increase in E_g . This observation is expected, since the grain size increases by increasing the B concentration and decreasing the Al concentration. Our results are consistent with the results in [37, 38]. As mentioned in the introduction, due to the difference in the ionic radii, electron work function and electron affinities of the dopants (Al and B), partial substitutions of either ion (B^{+3} or Al^{+3}) incorporation into the crystalline lattice occur. It is expected that Al^{+3} incorporation occurs more than that of B^{+3} ions. This ultimately leads to domination of the influence of Al-doping on that of B-doping. Further investigation was needed to conclude the efficiency of co-doping ratios including the annealing temperatures and their ambient conditions in order to give an absolute conclusion.

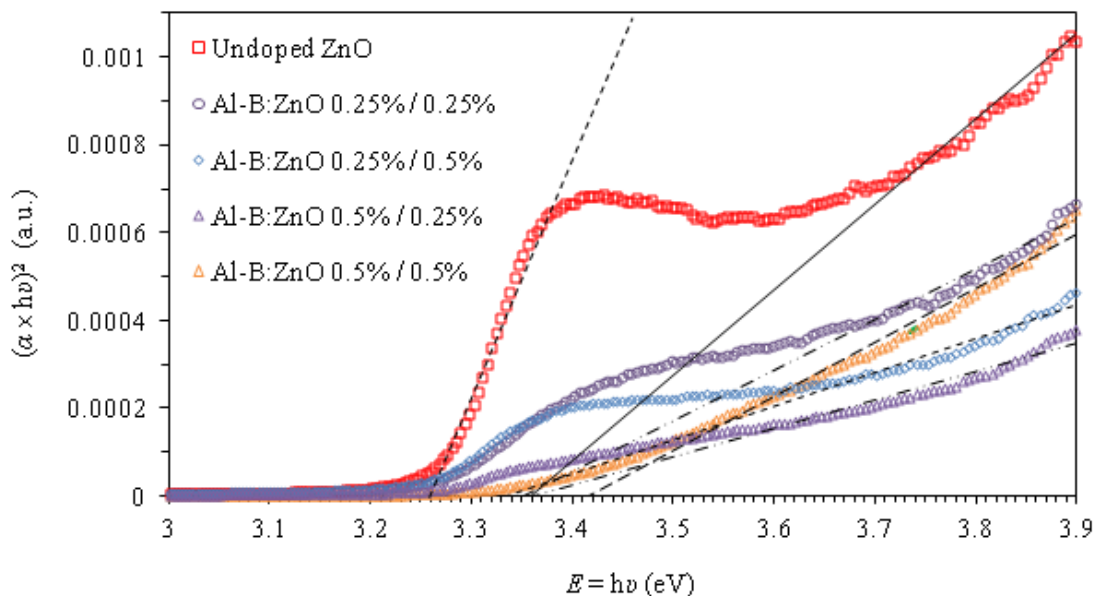


FIG. 5. Tauc optical band gap energy of the dip coated undoped and Al-B-doped ZnO thin films.

TABLE 1. The band gap energy obtained from Tauc plot with its approximated excitonic energy and from the average transmittance value above the band edge for all the samples.

Sample	Tauc E_g (eV)	Excitonic E (meV)	Transmittance E_g (eV)
Undoped ZnO	3.255, 3.362	107	3.333
Al-B:ZnO, 0.25% - 0.25 %	3.350	95	3.374
Al-B:ZnO, 0.25% - 0.50 %	3.340	85	3.369
Al-B:ZnO, 0.50% - 0.25 %	3.368	118	3.360
Al-B:ZnO, 0.50% - 0.50 %	3.420	165	3.430

Wemple-DiDomenico Model

S. H. Wemple and M. DiDomenico [39] have analyzed the refractive index dispersion data below the absorption edge for various covalent and ionic materials in a wide range of different solids and liquids. The analysis was made based on proposing a single effective oscillator model (Wemple and DiDomenico, 1971 [32, 39]), which is a semi-empirical dispersion relation for determining the refractive index n as a function of photon energy as seen in Eq. (1) [23, 30, 36]. The effective single oscillator is characterized by its average excitation energy for electronic transitions (E_o), dispersion energy (E_d) as a measure of the average strength of the optical inter-band transitions, average value of oscillator

strength (S_o), oscillator wavelength (λ_o) and the zero frequency or static refractive index (n_o). The index of refraction is defined as [23, 30, 36]:

$$n^2 - 1 = \frac{E_d E_o}{E_o^2 - E^2} \quad (1)$$

Plotting $(n^2-1)^{-1}$ against $(h\nu)^2$ gives the oscillator parameters by fitting the data to a straight line while extrapolating it to the zero frequency as seen in Fig. 6 for all the samples. The equations for the fitted lines are shown in the figure against each Al-B co-doping ratio, showing their intercepts with the vertical axis and their slopes.

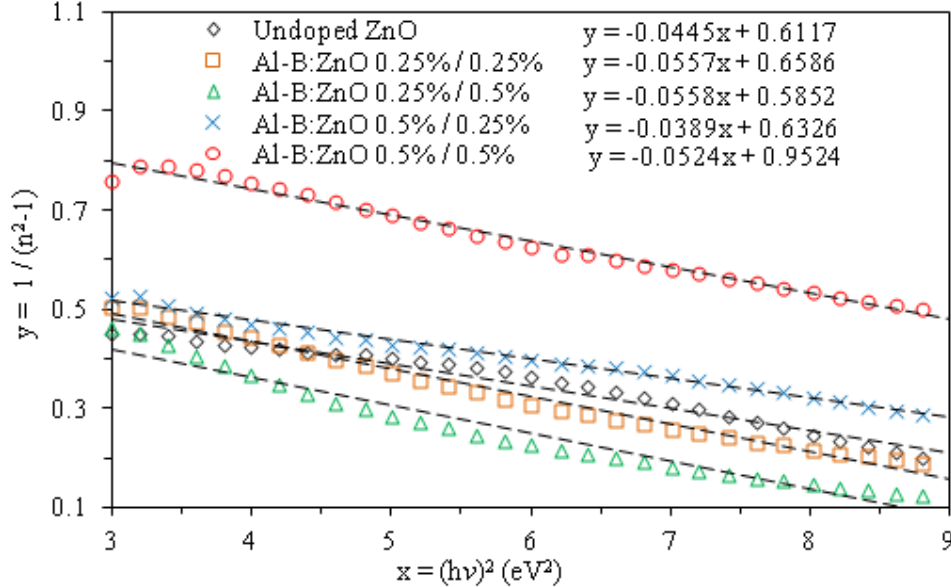


FIG. 6. The relationship between $(n^2-1)^{-1}$ and $(E = h\nu)^2$ of the single oscillator model for all the Al-B co-doping ratios compared to that for the undoped ZnO film.

The values of E_o and E_d can then be calculated from the slope $(E_o E_d)^{-1}$ and the intercept at the vertical axis (E_o/E_d). The average oscillator wavelength (λ_o) and the oscillator strength (S_o) parameters for all the samples were

also determined by the single oscillator model given by Eq. 2 as [23, 30, 36, 39]:

$$n^2 - 1 = \frac{S_o \lambda_o^2}{(1 - \lambda_o^2) / \lambda^2} \quad (2)$$

By plotting $(n^2-1)^{-1}$ against (λ^{-2}) , one can obtain the values of the oscillator parameters by fitting the data to a straight line at low frequencies and extrapolating it to the zero

frequency as seen in Fig. 7 for all the thin films. The values of S_o and λ_o were obtained from the slopes $(1/S_o)$ and the intercepts $(1/S_o\lambda_o^2)$ at the vertical axis.

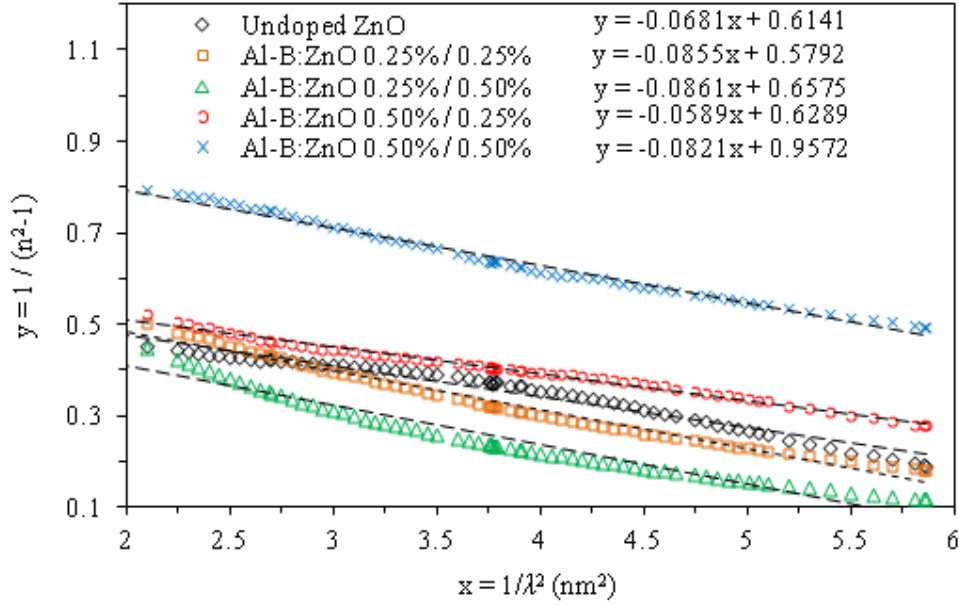


FIG. 7. The relationship between $(n^2-1)^{-1}$ and (λ^{-2}) of the single oscillator model for all the Al-B co-doping ratios compared to that for the undoped ZnO film.

The static refractive index (n_o) was calculated from Wemple-DiDomenico dispersion parameters (E_o and E_d) using Eq. (3) [23, 30, 36, 39]:

$$n_o = \sqrt{1 + (E_d/E_o)} \quad (3)$$

The parameters characterizing the average oscillator model proposed by Wemple and DiDomenico [39] representing the light-material interactions are shown in Table 2. It is clearly seen that the average oscillator energy (E_o) was found to be as high as 4.03 or 4.26 eV when Al content was made as high as 0.50% while B content was either 0.25% or 0.50%, respectively. However, E_o value was found to be as low as 3.44 or 3.18 eV when Al content was made as low as 0.25% while B content was made at 0.25% or 0.50%, respectively. E_o for the undoped ZnO film was found to be around the average value (3.73 eV) compared to the values obtained from the extreme values of Al content regardless of boron concentration. This indicates that increasing the Al content in the solution increases E_o , while increasing the B content decreases the value of E_o at low Al concentration (0.25%) and increases it at higher value (0.50%). The dispersion energy (E_d) was also found to be

at its minimum value (4.47 eV) when both concentrations for Al and B were maintained high at 0.50% and found to be the highest (6.37 eV) when the B concentration was lowered to (0.250%). However, E_d was found to be at almost the moderate value (5.22 or 5.30 eV) when boron concentration is lowered to 0.25% and Al content was made low (0.25%) or high (0.50%), respectively. E_d for the undoped ZnO film was found to be in between the extreme values (6.10 eV). The static index of refraction (n_o) was found to be at the highest value (1.65) when B concentration was higher (50%) and B concentration at the lowest value (0.25%). n_o was found to be minimum (1.43) when the doping concentration for both Al and B was made at the highest value (0.50%). It was found that n_o increases by decreasing boron at fixed aluminum ratio (0.50%) while it increases (1.59 to 1.65) by increasing B content from 0.25% to 0.50% at the minimum content of Al (0.25%). The oscillator strength S_o was found to be at the highest value ($16.98 \times 10^{-5} \text{ nm}^{-2}$) when the Al / B ratios are 0.50% / 0.25% and at the lowest value ($11.61 \times 10^{-5} \text{ nm}^{-2}$) when these ratios are reversed (i.e., 0.25% / 0.50%), while its value was found to be around the average of these

extremes ($14.68 \times 10^{-5} \text{ nm}^{-2}$) without co-doping. The average wavelength (λ_o) was found to be at the lowest value (8.58 nm) when Al concentration (0.50%) was made higher than B concentration (0.25%). It was found at its highest value (14.76 nm) when the ratios were reversed. Similarly, λ_o was found to be at around the average value (11.09 nm) of these extremes without co-doping. Our results of the undoped ZnO material were found to be consistent with the results seen in the literature for ZnO films as deposited with the DC sputtering at room temperature without annealing, but do not agree with the results found for the films when deposited at higher substrate temperature or treated with post-annealing [23]. Our results of E_o and E_d for the Al-B co-doped thin films were found to be much higher than the results

obtained for single doping with Al and comparable with the results obtained for films co-doped with Li-Mg [40, 41]. Our results were found to be comparable to those for ZnO thin films deposited with pure boron [42]. It is clearly seen that the co-doping process by Al and B controls the single oscillator's parameters above and below each corresponding parameter for the undoped ZnO film. From the material processing point of view, this indicates that the optical, and hence the electrical as well as the microstructural characteristics can be controlled. This achievement is due to the fact that controlling the co-doping ratios for Al and B controls the physical properties of the films. It shows that co-doping (by Al and B) gives the benefit over singular doping (by either Al or B) through better control of the film characteristics.

TABLE 2. The parameters obtained for the average single oscillator model proposed for Wemple-DiDomenico model representing the light-material interactions.

Sample	E_o (eV)	E_d (eV)	n_o	$S_o \times 10^{-5} (\text{nm}^{-2})$	λ_o (nm)
Undoped ZnO	3.73	6.10	1.62	14.68	11.09
Al-B:ZnO, 0.25% / 0.25 %	3.44	5.22	1.59	11.70	14.76
Al-B:ZnO, 0.25% / 0.5 %	3.18	5.30	1.65	11.61	13.10
Al-B:ZnO, 0.50% / 0.25 %	4.03	6.37	1.61	16.98	9.36
Al-B:ZnO, 0.50% / 0.50 %	4.26	4.47	1.43	12.18	8.58

Structural Properties for the Un-doped and the Al-B Co-doped ZnO Thin Films

It was found that annealing the films under atmospheric pressure at 500 °C for two hours produces the best crystalline features [24]. All samples were treated similarly. Fig. 8 shows the X-ray diffraction patterns for the undoped and the Al-B co-doped ZnO thin films. It shows the X-ray diffraction patterns with the peaks observed at Bragg's angles for the undoped ZnO film at 31.496° , 34.173° and 35.994° which belong to the hexagonal crystalline orientations for Miller indices of (100), (002) and (101) planes, respectively. The lattice parameters for ZnO thin films evaluated by XRD patterns (see Table 3) are in good agreement with standard values for the ZnO thin films reported by the Joint Committee on Powder Diffraction

Standards (JCPDS 36-1451) [43]. The crystallinity was improved in favor of the (002) orientation when B concentration was made dominant (50%) in the ZnO solution, while the Al concentration was made low at 25%. It was found that the most crystalline features occur preferring the (002) orientation when Al concentration was dominant (50%) while B concentration was low (25%). It is worth mentioning that small peaks have appeared, mainly in the non-doped ZnO film, in relevance to the planes defined by the Miller indices (102), (110), (103) and (112), respectively. These peaks indicate that the materials deposited under our experimental conditions were polycrystalline in nature. They gradually weakened by varying the co-doping ratios until they disappeared at higher concentrations of Al and B (0.50% for each).

TABLE 3. The lattice parameters of ZnO thin film annealed at 500 °C for 2 hours.

a (Å)		c (Å)	
Calculated	Standard	Calculated	Standard
3.279	3.250	5.246	5.207

Table 4 shows the lattice constants and the structural parameters for all samples. Low concentrations (25%) for both dopants (Al and B) did not change the grain size, the dislocation and the strain compared to those for undoped ZnO film. The grain size was found to increase (21.872 nm), while the dislocation and strain were found to decrease to 20.903×10^{14} (lines/m²) and 1.611×10^{-3} , respectively when B concentration was dominant (50%) while Al concentration was low (25%). However, the grain size was found to decrease (17.895 nm),

while the dislocation and strain were found to increase to 31.226×10^{14} (lines/m²) and 1.969×10^{-3} when Al concentration was dominant (50%) and B concentration was low (25%). The rough decrease in the grain size (16.404 nm), the huge increase in the dislocation (37.161×10^{14} (lines/m²)) and the rough increase in strain (2.148×10^{-3}), respectively occur when both dopants (Al and B) were increased in ratios to 50% for each. One can recognize the changes in strain causes relevant changes in the lattice parameters, accordingly.

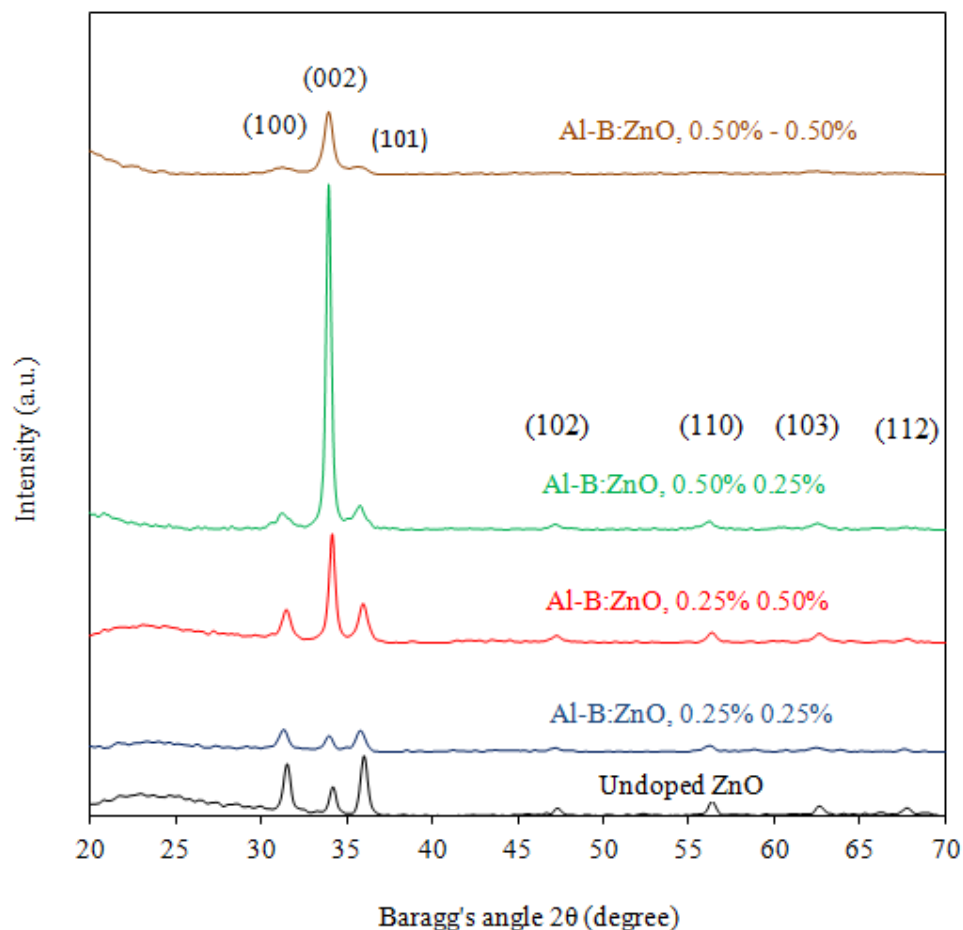


FIG. 8: The X-ray diffraction patterns of thin films with various concentrations of Al and B.

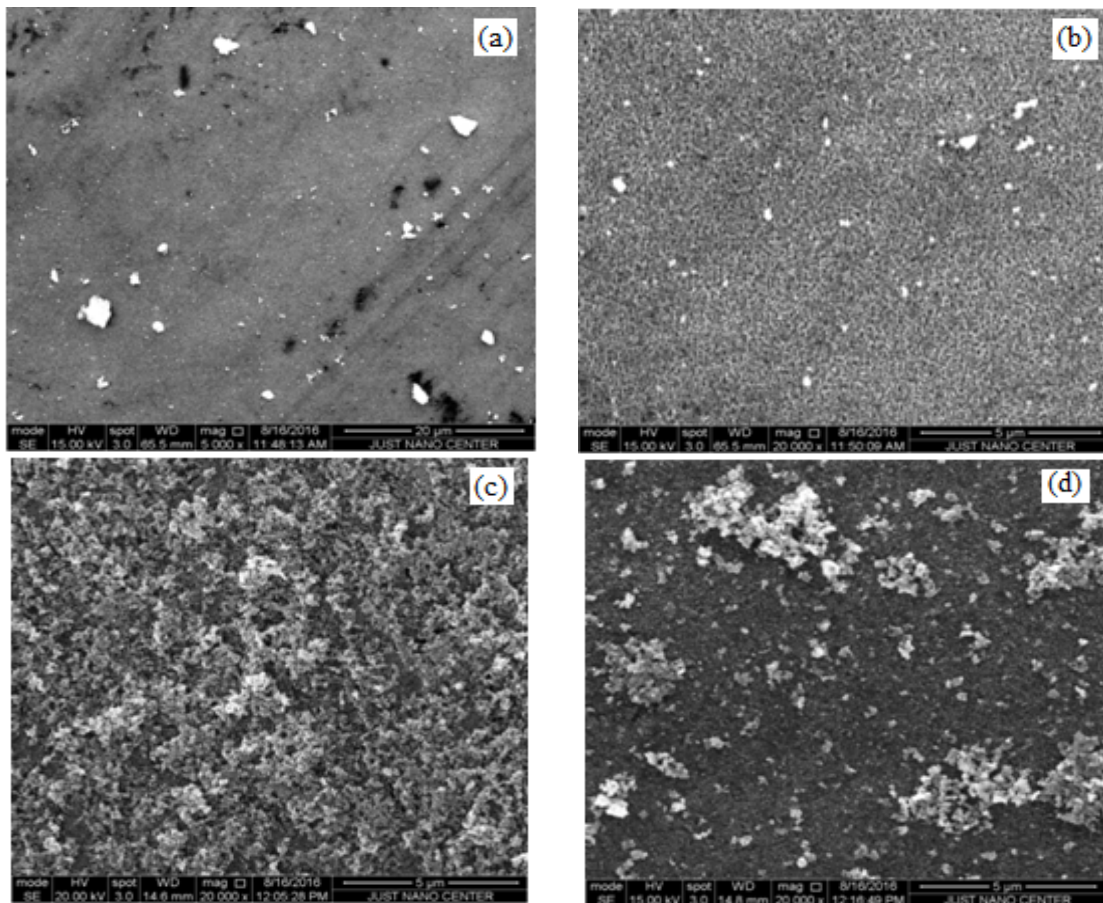
TABLE 4. The lattice parameters and structural parameters for thin films annealed at 500 °C for 2 hours.

Sample	Lattice Parameters		Grain size D (nm)	The dislocation density δ ($\times 10^{14}$) (lines/m ²)	Strain ϵ ($\times 10^{-3}$)
	a (Å)	c (Å)			
Undoped ZnO	3.279	5.246	19.684	25.806	1.790
Al-B:ZnO, 0.25 - 0.25	3.299	5.279	19.684	25.806	1.790
Al-B:ZnO, 0.25 - 0.50	3.283	5.252	21.872	20.903	1.611
Al-B:ZnO, 0.50 - 0.25	3.246	5.283	17.895	31.226	1.969
Al-B:ZnO, 0.50 - 0.50	3.307	5.283	16.404	37.161	2.148

SEM Micrographs

The Scanning Electron Microscope micrographs have been used to investigate the surface morphologies of the films for the undoped ZnO and the Al-B co-doped ZnO films. Fig. 9 shows the SEM micrographs for the undoped ZnO and the Al-B co-doped ZnO (0.25% / 0.25%, 0.25% / 0.50%, 0.50% / 0.25% and 0.50% / 0.50% of Al-B contents, respectively) thin films. Undoped ZnO film exhibits a smooth surface with very small crystalline grains as seen in the large-scale micrograph (20 μm scale) of Fig. 9(a). The grain features were found to be so fine and they look very uniform as seen on the short-range scale (5 μm scale) of Fig. 9(b). As Al and B were introduced to the film, the micrograph of the film surface varied accordingly. Fig. 9 (c) shows the micrograph for the film surface for low

concentrations of both Al and B (25%). It is clearly seen that big clusters of ZnO oxides (white colors) are observed on the surface with no much regularity. As B concentration becomes dominant (50%), the clusters were observed to disseminate, forming a solid surface of Al-B co-doped beneath rough grains (black color) as seen in Fig. 9(d). As Al becomes dominant (50%), Al-B co-doped ZnO grains become finer and clear (as seen in Fig. 9(e)) with even shorter scale (500 nm). This agrees well with the X-ray diffraction patterns, where the grain size increases as B content increases, while it decreases as Al content increases. Finally, when both of Al and B contents increase to 50% for each, the film surface looks fine and almost completely compensated from the residuals of zinc and oxides by the additives of Al and B as seen in Fig. 9(f).



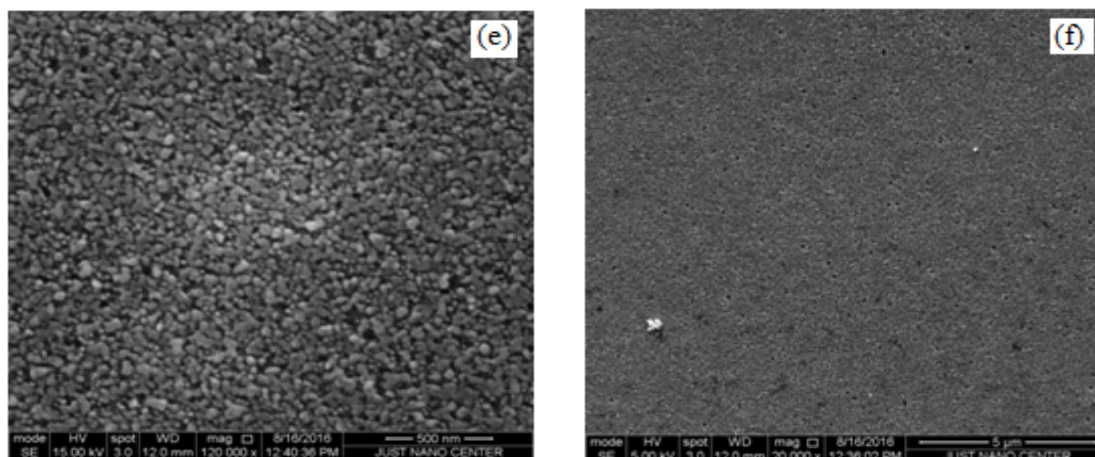


FIG. 9. The SEM micrographs of the undoped ZnO with (a) large scale (20 μm) and (b) short scale (5 μm) in addition to Al-B co-doped ZnO thin film with (c) 0.25% - 0.25%, (d) 0.25% - 0.50%, (e) 0.50% - 0.25% and (f) 0.50% - 0.50% concentrations, respectively.

Deposition of ZnO Nanoparticles on Seeding Platforms by Hydrothermal Deposition

ZnO nanoparticles (NP) were grown on undoped or Al-B co-doped ZnO thin films used as host seeded-platforms. The platforms were deposited on glass substrates as discussed in the previous sections. The ZnO-NPs were grown by hydrothermal process. Figs. 10(a) and (b) show the surface of small sizes (around 50 nm) of aggregated ZnO-NPs grown on undoped ZnO thin film in large-scale (1 μm) and in short-scale (500 nm) micrographs, respectively. The films were found to be suitable for growing the ZnO-NPs with uniform morphology. Attempts of growing ZnO-NPs on Al-B co-doped ZnO seeded platforms with 0.25% for each doping element produce cloudy diffused clustered-forms of NPs ranging from 100 nm to 250 nm as seen in Fig. 10(c). When B content becomes the

dominant doping element (0.50%), the cloudy nanostructures diffuse into fine and soft dissociated NPs as seen in Fig. 10(d). However, as Al becomes the dominant doping element (0.50%), small sizes of hexagonal shape NPs (around 100 nm) were observed to aggregate on the surface as seen in Fig. 10(e). It is worth mentioning that this combination of co-doping produces the best films of hexagonal crystalline microstructure with (002) preferred orientation as seen in the X-ray diffraction (XRD) patterns (Fig. 8). It is clearly seen that this form of Al-B co-doped ZnO seeded platforms showed the best combination in hosting good growth of NPs. As the platform becomes rich with both Al and B (50% for each), the grown nanostructure becomes nonuniformly cloudy with no distinct homogeneous structure as seen in Fig. 10 (f).

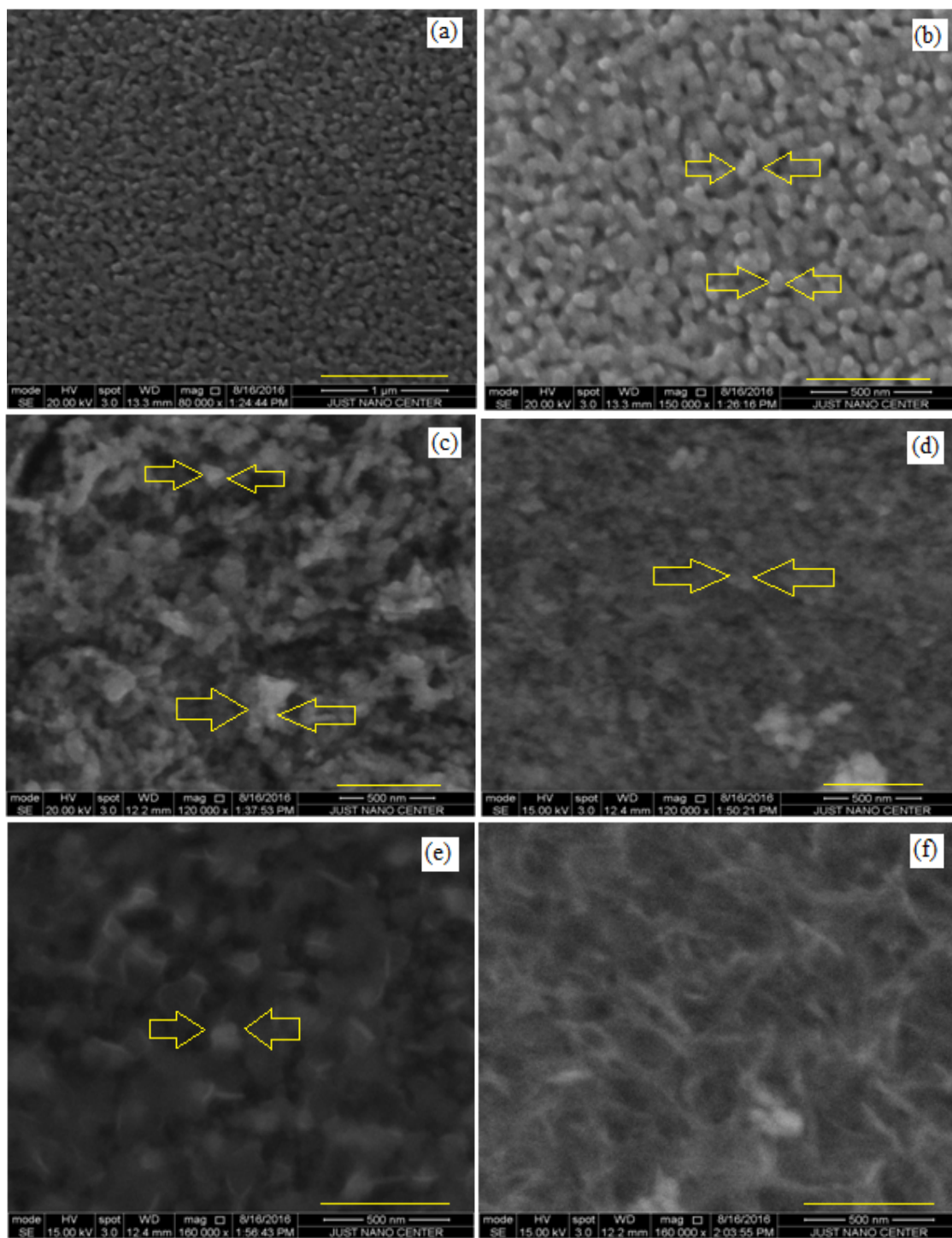


FIG. 10. The SEM micrographs of ZnO-NPs on seeded undoped ZnO platforms in (a) large scale (1 μ m) and (b) short scale (500 nm) and Al-B co-doped platforms with (c) 0.25% - 0.25%, (d) 0.25% - 0.5%, (e) 0.50% - 0.25% and (f) 0.50% - 0.50% concentrations, respectively.

Conclusions

Undoped ZnO thin films have been prepared by sol gel using dip coating technique. The zinc acetate dihydrate ($\text{Zn}(\text{CH}_3\text{CO}_2)_2 \cdot 2\text{H}_2\text{O}$) with 99.5% of purity was used as a starting material dissolved with ethanol, while monoethanolamine was used as a stabilizer. Al-B co-doped ZnO thin films have been prepared by using the ZnO solution in addition to boric acid (H_3BO_3) and aluminum nitrate ($\text{Al}(\text{NO}_3)_3 \cdot 9\text{H}_2\text{O}$) to form the final ZnO solvent. The various molar ratios of boric acid / aluminum nitrate used in the solutions were 0.0% / 0.0%, 0.25% / 0.25%, 0.25% / 0.50%, 0.50% / 0.25% and 0.50% / 0.5%, respectively.

The transmittance and reflectance were investigated and the index of refraction, extinction coefficient and optical band gap energy have been evaluated accordingly. The average transmittance of the undoped ZnO thin film was found to be around (>80%) in the visible region. The transmittance reduces, in a curve-trend measure, by increasing the B concentration and increases by decreasing the Al concentration. The relevant optical properties were also affected accordingly. The index of refraction was found to range between 1.63 and 2.43 for the undoped ZnO films. The optical band gap energy for the undoped deposited ZnO thin film was found to be about 3.362 eV (3.333 eV from the transmittance). These values agree well with that for the bulk ZnO (3.40 eV) and for the thin films (3.37 eV). The E_g value was found to decrease while increasing the concentration of Al and decrease while increasing the B content in the solution. This fact supports the prediction that the optical band gap energy decreases while the grain size increases in the films. As the film becomes rich with both Al and B, E_g increases to 3.430 eV, indicating that complete compensation for zinc and oxygen vacancies has been almost achieved by the presence of Al and B. The higher partial ionic substitution of Al^{+3} incorporation in the lattice structure, compared to that of B^{+3} ion, leads to domination of its influence on the optical and structural properties of the co-doped thin films with still minor influence of B on the microstructure. However,

further investigation is needed to conclude the efficiency of co-doping ratios including the annealing temperatures and their ambient conditions.

The films' microstructure has been investigated using XRD. The analysis revealed a polycrystalline microstructure before being treated with post-annealing, while the microstructure has been enhanced to almost single orientation by proper annealing temperature (500 °C) for a proper period of time (2 hours). Undoped ZnO thin film demonstrated a hexagonal wurtzite structure. The lattice constants were calculated and found to agree well with that for the bulk ZnO material. The crystalline grain size for the undoped ZnO film was found to be around 20 nm. The grain size increases by increasing the concentration of B and decreases by increasing the content of Al in the films. This fact confirms the predicted result of increasing the grain size being associated with decreasing the optical band gap energy. The SEM micrographs indicate that the morphology of the film surface depends on the B and Al concentrations. It was found that using the undoped ZnO thin film as the host seeded platform to grow fine and uniform ZnO-NPs is feasible with an average particle size of around 20 nm. However, introducing boron to the ZnO platform disturbs the regularity of the NPs aggregation. Low ratio of boron concentration leads to the formation of huge clusters, while increasing the boron ratio diffuses the clusters' density while bowing the size to form irregular nanoclouds at higher boron concentration. Aluminum-rich seeded platforms produce hexagonal NPs with an average size of 100 nm.

Acknowledgments

The authors would like to thank Jordan University of Science and Technology for the support provided by the Deanship of Scientific Research. The authors would also like to thank Prof. Borhan Albiss and Prof. M-Ali Al-Akhras for their help in using the facilities of the Center of Nanotechnology and the Lab. of Biomedical Physics.

References

- [1] Shampa, M., "Preparation of Undoped and Some Doped ZnO Thin Films by Silar and Their Characterization", (Department of Physics, University of Bardhaman, Bardhaman, India, 2014).
- [2] Karpina, V., Lazorenko, V., Lashkarev, C., Dobrowolski, V., Kopylova, L., Baturin, V., Pustovoytov, S., Karpenko, A.J., Eremin, S. and Lytvyn, P., *Crystal Research and Technology*, 39 (2004) 980.
- [3] Wong, L.H. and Lai, Y.S., *Thin Solid Films*, 583 (2015) 205.
- [4] Wen, B., Liu, C., Wang, N., Wang, H., Liu, S., Jiang, W., Ding, W., Fei, W. and Chai, W., *Applied Physics A*, 121 (2015) 1147.
- [5] Liu, Y., Li, Y. and Zeng, H., *Journal of Nanomaterials*, 2013 (2013).
- [6] Tsin, F., Venerosy, A.L., Vidal, J., Collin, S.P., Clatot, J., Lombez, L., Paire, M., Borensztajn, S., Broussillou, C.D., Grand, P.P., Jaime, S., Lincotm D. and Rousset, J., "Electrodeposition of Zno Window Layer for an All-Atmospheric Fabrication Process of Chalcogenide Solar Cell", *Scientific Reports*, The Author(s), (2015) p. 8961.
- [7] Lee, J.H. and Park, B.O., *Thin Solid Films*, 426 (2003) 94.
- [8] Kaur, G., Mitra, A. and Yadav, K., *Progress in Natural Science: Materials International*, 25 (2015) 12.
- [9] Kim, S., Yoon, H., Kim, D.Y., Kim, S.O. and Leem, J.Y., *Optical Materials*, 35 (2013) 2418.
- [10] Wen, B., Liu, C.Q., Wang, N., Wang, H.L., Liu, S.M., Jiang, W.W., Ding, W.Y., Fei, W.D. and Chai, W.P., *Chinese Journal of Chemical Physics*, 29 (2016) 229.
- [11] Minne, S., Manalis, S. and Quate, C., *Applied Physics Letters*, 67 (1995) 3918.
- [12] Liu, C., Yu, A., Peng, M., Song, M., Liu, W., Zhang, Y. and Zhai, J., *The Journal of Physical Chemistry C*, 120 (2016) 6971.
- [13] Li, Y., Gao, Z., Qin, W., Wen, Q. and Jun, M., *Biochem. Anal. Biochem.*, 5 (2016) 2161.
- [14] Eberspacher, C., Fahrenbruch, A.L. and Bube, R.H., *Thin Solid Films*, 136 (1986) 1.
- [15] Natsume, Y. and Sakata, H., *Thin Solid Films*, 372 (2000) 30.
- [16] Kumar, V., Singh, R., Purohit, L. and Mehra, R., *Journal of Materials' Science & Technology*, 27 (2011) 481.
- [17] Ammaih, Y., Lfakir, A., Hartiti, B., Ridah, A., Thevenin, P. and Siadat, M., *Optical and Quantum Electronics*, 46 (2014) 229.
- [18] Jagadamma, L.K., Al-Senani, M., El-Labban, A., Gereige, I., Ndjawa, N., Guy, O., Faria, J.C., Kim, T., Zhao, K. and Cruciani, F., *Advanced Energy Materials*, 5 (2015).
- [19] Chen, J., Chen, D. and Chen, Z., *Science in China, Series E: Technological Sciences*, 52 (2009) 88.
- [20] K.B.P.T.o.E.-S.b.I.R. *Environmental Chemistry.com*, <http://EnvironmentalChemistry.com/yogi/periodic/ionicradius.html> (1995 - 2017).
- [21] Boundless, *Boundless Chemistry*, <https://www.boundless.com/chemistry/textbooks/boundless-chemistry-textbook/atoms-molecules-and-ions-2/the-periodic-table-35/the-periodic-table-203-3515/>.
- [22] Gupta, C.A., Mangal, S. and Singh, U.P., *Applied Surface Science*, 288 (2014) 411.
- [23] Al-Sanableh, A., "Structural and Optical Properties of ZnO Thin Films Deposited by Sol Gel Coating Technique", (Physics Department, Jordan Univesity of Science and Technology, Irbid, 2006).
- [24] Bataineh, Q.M., "Optical and Structural Characterization of Sol-Gel B-ZnO and ZnO Thin Films Used As Seeded Platform for Nanostructured ZnO", (Physics Department, Jordaon Univesity of Science and Technology, 2016).
- [25] Sreedhar, A., Kwon, J.H., Yi, J. and Gwag, J.S., *Ceramics International*, 42 (2016) 14456.

- [26] Ilican, S., Yakuphanoglu, F., Caglar, M. and Caglar, Y., *Journal of Alloys and Compounds*, 509 (2011) 5290.
- [27] Yang, L., Zhang, Y.P., Xu, J.W. and Wang, H., *Applied Mechanics and Materials*, Trans. Tech. Publ., (2014) 1280.
- [28] Sreedhar, A., Kwon, J.H., Yi, J. and Gwag, J.S., *Ceramics International* (2016).
- [29] Ahmad, A.A. and Omari, A.M., *International Conference on Advanced Materials (ICAM 2015)* IOP Publishing, IOP Conf. Series: Materials Science and Engineering, 92, 012024, IOP Publishing, Irbid, Jordan, 2015, p. 012024.
- [30] Ahmad, A.A., Alsaad, A.M., Albiss, B.A., Al-Akhras, M.A., El-Nasser, H.M. and Qattan, I.A., *Physica B: Condensed Matter*, 470 (2016) 21.
- [31] Ahmad, A. and Alsaad, A., *The European Physical Journal B-Condensed Matter and Complex Systems*, 52 (2006) 41.
- [32] Ahmad, A.A., Albiss, B.A., Al-Akhras, M.A., El-Nasser, H.M. and Qattan, I.A., *Thin Solid Films*, 606 (2016) 133.
- [33] Hsu, H.C., Shown, I., Wei, H.Y., Chang, Y.C., Du, H.Y., Lin, Y.G., Tseng, C.A., Wang, C.H., Chen, L.C. and Lin, Y.C., *Nanoscale*, 5 (2013) 262.
- [34] Janotti, A. and Van de Walle, C.G., *Reports on Progress in Physics*, 72 (2009) 126501.
- [35] Impellizzeri, G., Scuderi, V., Romano, L., Napolitani, E., Sanz, R., Carles, R. and Privitera, V., *Journal of Applied Physics*, 117 (2015) 105308.
- [36] Ahmad, A.A., Ianno, N.J., Snyder, P.G., Welipitiya, D., Byun, D. and Dowben, P.A., *Journal of Applied Physics*, 79 (1996) 8643.
- [37] Guillen, C. and Herrero, J., *Vacuum*, 84 (2010) 924.
- [38] Elizabeth, U., Uno, E.O., Sobechukwu, M.C., Olusunle, S.O.O. and Okwuego, E.C., *American Journal of Energy Science*, 3(4) (2016) 21.
- [39] Wemple, S. and DiDomenico Jr, M., *Physical Review B*, 3 (1971) 1338.
- [40] Kim, M.S., Yim, K.G., Son, J.S. and Leem, J.Y., *Bulletin of the Korean Chemical Society*, 33 (2012) 1235.
- [41] Aksoy, S., Caglar, Y., Ilican, S. and Caglar, M., *Journal of Alloys and Compounds*, 512 (2012) 171.
- [42] Hasan, N.A., Abbas, A.A. and Mohammed, J.S., *Diyala Journal for Pure Sciences*, 12 (2016) 70.
- [43] Sarma, H. and Sarma, K.C., *Int. J. Sci. Res. Publ.*, 4 (2014) 1.

Jordan Journal of Physics

Communication

Size-Fractionated Number and Mass Concentrations in the Urban Background Atmosphere during Spring 2014 in Amman – Jordan

Tareq Hussein and Ala'a Betar

Department of Physics, The University of Jordan, Amman 11942, Jordan.

Received on: 10/12/2016;

Accepted on: 5/2/2017

Abstract: The number size distribution of urban aerosols was never measured in Amman, Jordan. In this study, we aim at investigating the mean number size distribution (optical diameter 0.3–10 μm) and size-fractionated particle number and mass concentrations during spring 2014 in the urban background atmosphere of Amman, Jordan. The overall mean particle number concentration of coarse particles (PN_{10-1}) was $1.8\pm 2.9\text{ cm}^{-3}$ and the corresponding mass concentration PM_{10-1} was $22.1\pm 44.3\text{ }\mu\text{g/m}^3$. The overall mean submicron particle number concentration ($PN_{1-0.01}$) was $26800\pm 12800\text{ cm}^{-3}$ and the corresponding mass concentration $PM_{1-0.01}$ was $4.7\pm 1.9\text{ }\mu\text{g/m}^3$. The calculated 24-hour PM_{10} concentrations were 3.7–126.4 $\mu\text{g/m}^3$. According to the Jordanian 24-hour PM_{10} concentrations limit value (120 $\mu\text{g/m}^3$), there was only one exceedance that observed on April 16th. The mean particle number size distribution during that period was characterized by three main lognormal modes: ultrafine, accumulation and coarse modes. The geometric mean diameters (D_{pg}) were 0.05 μm , 0.125 μm and 1.7 μm , respectively for the ultrafine mode, accumulation mode and coarse mode. The corresponding mode number concentrations were 12000 cm^{-3} , 300 cm^{-3} and 2.6 cm^{-3} .

Keywords: *Particle distribution, Multi-lognormal fitting, Portable aerosol instruments.*

Introduction

Urban aerosols have a complex dynamic behavior, because they are a mixture of regionally transported aerosols and a wide range of locally emitted aerosols [1]. Besides being externally mixed, their composition can vary depending on the source type, geographical region and state of development and dynamic processes involved in their transformation. Urban aerosols do not only impact the local air quality (e.g. loss of visibility), but they also have a large spatial-scale effect, because they are likely transported over large distances, where they affect air quality and climate. Exposure to urban aerosols might lead to serious health effects [2–5]. As stated by the WHO, health effects of urban aerosols are usually assessed by monitoring exposure to certain particulate matter classes (such as PM_{10} and $PM_{2.5}$), in addition to some gaseous pollutants (such as carbon oxides, nitrogen oxides, ... etc.).

The aerosol research in the Middle East and North Africa (MENA) region has been limited to PM concentrations, some gaseous pollutants, elemental and chemical analysis, long-range transport, mineral dust and dust episodes and optical depth [6–48]. Studies focused on particle number concentrations and particle number size distributions are very rare in the MENA region [49, 50]. It is worth to mention two studies that presented an Enhanced Particulate Matter Surveillance Program; this program aimed at providing scientifically founded information on the physical and chemical properties of dust collected during a period of approximately 1 year in Djibouti, Afghanistan, Qatar, United Arab Emirates, Iraq and Kuwait [51, 52]. It was shown that air quality of coastal regions in North Egypt is affected by the flow bringing long-range transported anthropogenic air pollution from Europe towards North Africa as well as the flow of desert dust from North Africa towards Europe [53].

According to our knowledge, there are less than ten articles published about PM, some gaseous pollutants and limited chemical analysis in Jordan [54–61]. For instance, Al-Momani *et al.* [56] and Gharaibeh *et al.* [57] focused on heavy metals and elemental analysis of aerosol samples in Al-Hashimya and Irbid, respectively. Soleiman *et al.* [61] indicated that high ozone concentrations in Jordan are due to transboundary transport of ozone precursors from East Mediterranean coast into Jordan. Hamasha and Arnott [58] reported black carbon concentrations at six sites in Irbid city. Abu Allaban *et al.* [55] focused on dust re-suspension from limestone quarries nearby a town located north east of Amman and reported PM_{10} concentrations as high as $600 \mu\text{g}/\text{m}^3$ with most of the airborne PM in the coarse fraction. However, there are only two studies which focused on fine particle number concentrations in Jordan, specifically in Amman city [62, 63].

The main objective of this study is to present, for the first time, the size-fractionated particle number and mass concentrations in Amman during the spring season of the year 2014. We also presented, for the first time, the mean particle number size distribution by merging two aerosol data-sets: (1) submicron particle number concentration and (2) particle number size distributions (diameter 0.3–10 μm).

Materials and Methods

Site Description

The campus of the University of Jordan [32.0129N, 35.8738E] is situated in the northern part of Amman, Jordan. It is about 10 km far from the city center (Fig. 1a). The campus is surrounded by a populated residential area with a small road network. One of the main highways is parallel to the western side of the campus. The main source of air pollution at this site is traffic emissions and small scale combustion processes from restaurants in and around the campus. The Department of Physics, where the aerosol measurements took place, is located in the middle of the campus (Fig. 1b).

Aerosol Measurement

The aerosol measurement was performed with an Optical Particle Counter (OPS, TSI model 3330) and a portable Condensation Particle Counter (CPC, TSI model 3007). The OPS was located inside a laboratory in the second floor, whereas the CPC was located inside an office in the first floor. The aerosol

inlets of both instruments were led through the windows to sample the outdoor air from the southern side of the Department of Physics (Fig. 1c). The height from the ground of the sampling inlet used for the OPS was about 10 meters, whereas that for the CPC was about 5 meters. Both instruments were calibrated prior to the measurement campaign.

The OPS measurement was conducted continuously during March 6 – April 30, 2014. The OPS 3330 measures the particle number size distribution (optical diameter 0.3–10 μm , 13 size-bins). The OPS was set to measure the particle number size distributions with the dead-time correction applied. The sampling time resolution and flow rate were 5 minutes and 1 L/min, respectively. A diffusion drier was used in the aerosol tubing of the OPS. The penetration efficiency through the tubing and the diffusion drier was experimentally determined.

The CPC measurement was conducted in two parts: March 6–17 and April 14–30, 2014. The instrument was operating somewhere else during March 18 – April 13. The CPC 3007 is capable of recording the submicron particle number concentration in the diameter range 0.01–1 μm . We operated the CPC with a 5-minute averaging time resolution. The sampling inlet was about 1 meter copper tube (4 mm inner diameter). The use of a short sampling line would have minimal effects on the nominal flow rate, cut-off size and particle losses. The penetration efficiency through the tubing was experimentally determined.

Weather Conditions

We obtained the weather data from the Jordan Meteorological Department (JMD). It was recorded at Amman Civil Airport, which is located in Marka about 11.5 km south-east of the University of Jordan campus. The weather data base included hourly averages of the ambient temperature, relative humidity, wind direction and speed, precipitation and pressure.

During the measurement campaign, the wind speed was as high as 11.6 m/s (median ~ 2.7 m/s and average ~ 3 m/s). The prevailing wind direction was mainly between -135° and $+45^\circ$. The median value of the temperature was ~ 18.3 $^\circ\text{C}$ (maximum value did not exceed 33 $^\circ\text{C}$ and minimum value was as low as 4 $^\circ\text{C}$). The relative humidity varied between 7% and 91% (average $\sim 40\%$ and median $\sim 36\%$). The mean pressure was around 925 mbar.



FIG. 1. (a) A map of Amman showing the campus of the University of Jordan (shaded), (b) the campus of the University of Jordan and (c) the sampling site at the Department of Physics.

Data Handling

The aerosol data-base in this study consisted of: (1) submicron particle number concentrations in the diameter range $0.01\text{--}1\ \mu\text{m}$ and (2) particle number size distributions ($0.3\text{--}10\ \mu\text{m}$, 13 size-bins). The aerosol data-base was first corrected for tubing particle losses. Then, we processed it to calculate hourly averages. We merged the particle number size distributions ($0.3\text{--}10\ \mu\text{m}$, 13 size-bins) and the submicron particle number concentrations ($0.01\text{--}1\ \mu\text{m}$) to form a particle number size distribution in the particle diameter range $0.01\text{--}10\ \mu\text{m}$. In that sense, we created an additional particle size-bin ($0.01\text{--}0.3\ \mu\text{m}$) with an assumed geometric mean particle diameter set at $0.06\ \mu\text{m}$. The number concentration in that

particle size-bin ($0.01\text{--}0.3\ \mu\text{m}$) was obtained as follows:

$$PN_{0.3-0.01} = PN_{1-0.01} - PN_{1-0.3} \quad (1)$$

where $PN_{1-0.01}$ is the particle number concentration measured with the CPC and $N_{1-0.3}$ is the particle number concentration in the particle diameter range $0.3\text{--}1\ \mu\text{m}$ measured with the OPS, which is calculated by integrating the particle number size distribution in that particle diameter range:

$$PN_{1-0.3} = \int_{0.3}^1 n_N^0 d \log_{10}(D_p) \quad (2)$$

where $n_N^0 = dN/d \log_{10}(D_p)$ is the particle number size distribution and D_p is the particle diameter.

The particulate mass concentrations can be also calculated by assuming spherical particles and integrating the particle number size distribution as follows:

$$PM_{D_{p2}-D_{p1}} = \int_{D_{p1}}^{D_{p2}} \frac{\pi}{6} D_p^3 \rho_p n_N^0 d \log_{10}(D_p) \quad (3)$$

where ρ_p is the particle density. In this article, we summed spherical particles with unit density.

Multi-lognormal Fitting

The particle number size distribution $dN/d\log(D_p)$ can be mathematically described with the multi-lognormal distribution function [64, 65], which is the sum of several log-normal modes,

$$\left. \frac{dN}{d \log_{10}(D_p)} = \sum_{i=1}^m \frac{N_i}{\sqrt{2\pi \log_{10}(\sigma_{g,i})}} \times \exp\left(-\frac{1}{2} \left[\frac{\log_{10}(D_p/D_{pg,i})}{\log_{10}(\sigma_{g,i})}\right]^2\right) \right\} \quad (4)$$

where the left hand side is the normalized particle number concentration, i is an index for mode number with a number concentration N_i , a geometric mean diameter $D_{pg,i}$ and a standard deviation $\sigma_{p,i}$.

We used Eq. (4) to fit the particle number size distribution by assuming three main modes: an ultrafine mode, an accumulation mode and a coarse mode. In general, and as assumed by Hussein et al. [66], the fine particles can have three main modes (i.e., the ultrafine mode consists of a nucleation mode and an Aitken mode). In this study, we can't assume anything about these two ultrafine modes, because the first particle size-bin spans over the range 0.01–0.3 μm . In general, it is sometimes enough to a single mode for ultrafine particles (e.g. Whitby, 1978).

Results and Discussion

Average Concentrations

The instruments used in this study provide particle number size distribution (optical diameter 0.3–10 μm) measured with the OPS and submicron particle number concentration (diameter 0.01–1 μm) measured with the CPC (Figs. 2 and 3). Based on the hourly averaged data-base, the mean number concentration of particles in the diameter range 0.3–10 μm (i.e., $PN_{10-0.3}$) was about $41.1 \pm 25.9 \text{ cm}^{-3}$ (median value $\sim 35.7 \text{ cm}^{-3}$) with a maximum as high as 204 cm^{-3} (Fig. 2a). The corresponding particle mass concentration was about $23.6 \pm 44.7 \mu\text{g}/\text{m}^3$ (median $\sim 11.0 \mu\text{g}/\text{m}^3$) with a maximum of about $907.1 \mu\text{g}/\text{m}^3$ (Fig. 2b). It is important to mention here that the maximum $PN_{10-0.3}$ and $PM_{10-0.3}$ were not observed at the same time. For instance, the maximum $PN_{10-0.3}$ was observed during the nighttime on March 25, whereas the maximum $PM_{10-0.3}$ was observed during the morning on April 20.

The interesting part here is to consider the concentrations for micron and submicron particles separately (Fig. 4). The overall mean number concentration of coarse particles (PN_{10-1}) was about $1.8 \pm 2.9 \text{ cm}^{-3}$ (median value $\sim 0.9 \text{ cm}^{-3}$) with a maximum as high as 41.3 cm^{-3} (Fig. 4a). The corresponding mass concentration PM_{10-1} was about $22.1 \pm 44.3 \mu\text{g}/\text{m}^3$ (median value $9.7 \mu\text{g}/\text{m}^3$) with a maximum as high as $903.9 \mu\text{g}/\text{m}^3$ (Fig. 4b).

The overall mean submicron particle number concentration ($PN_{1-0.01}$) was about $26800 \pm 12800 \text{ cm}^{-3}$ (median $\sim 26100 \text{ cm}^{-3}$) and the maximum as high as 89500 cm^{-3} , which was recorded on March 16 (Fig. 4a). The corresponding mass concentration $PM_{1-0.01}$ was about $4.7 \pm 1.9 \mu\text{g}/\text{m}^3$ (median value $4.6 \mu\text{g}/\text{m}^3$) with a maximum as high as $13.9 \mu\text{g}/\text{m}^3$ (Fig. 4b). We could also give an estimate for the 24-hour PM_{10} concentrations. In total, we had 29 days for that (March 6–17 and April 14–30). The 24-hour PM_{10} concentrations varied between $3.7 \mu\text{g}/\text{m}^3$ and $126.4 \mu\text{g}/\text{m}^3$. According to the Jordanian 24-hour PM_{10} concentrations limit value ($120 \mu\text{g}/\text{m}^3$), there was only one exceedance which was on April 16th. Based on the hourly average, the PM_{10} concentrations were 0.6 – $465.5 \mu\text{g}/\text{m}^3$ (average $36.2 \pm 46.5 \mu\text{g}/\text{m}^3$ and median $22.6 \mu\text{g}/\text{m}^3$).

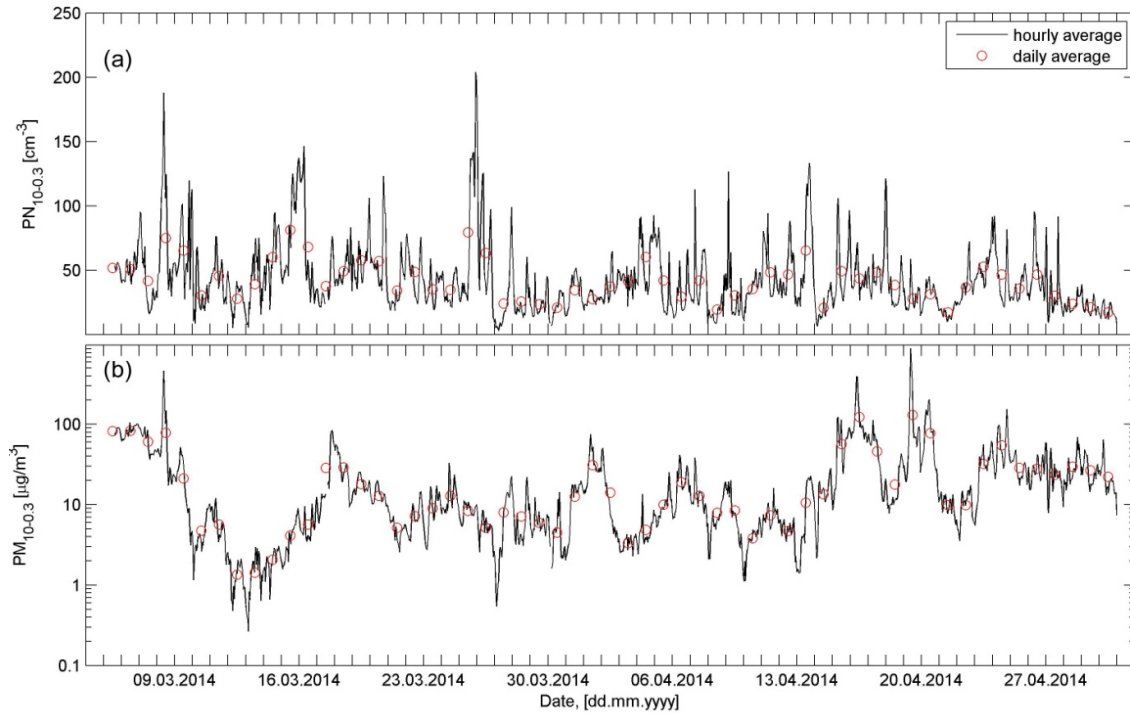


FIG. 2. Aerosol particle concentrations in the diameter range 0.3–10 μm measured with the Optical Particle Counter (a) number concentration and (b) mass concentration calculated by assuming spherical particles with unit density.

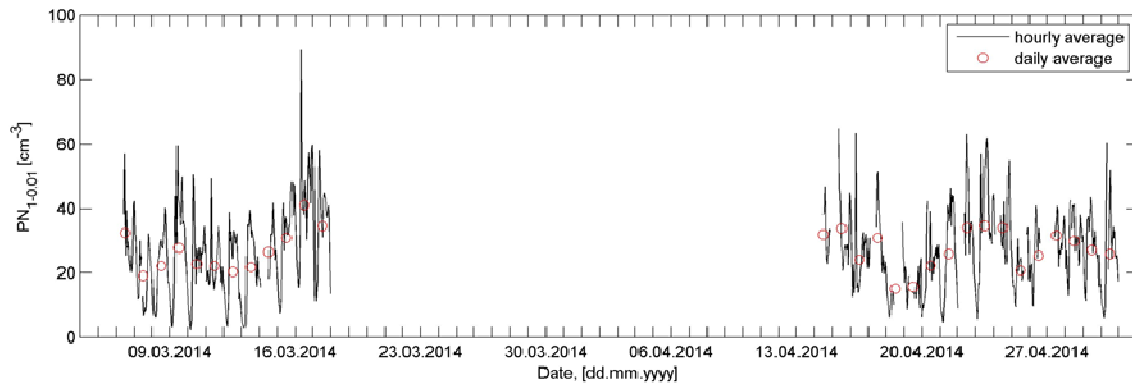


FIG. 3. Submicron particle number concentrations measured with the Condensation Particle Counter.

Average Particle Number Size Distribution

As explained before in the data handling section, we can generate the particle number size distribution by adding an additional particle size bin for particles in the diameter range 10–300 nm. The appropriate geometric mean diameter for this particle size bin is 60 nm. This is based on urban particle number size distributions measured elsewhere (e.g. Hussein *et al.*, 2004). The overall mean particle number size distribution is shown in Fig. 5 and the corresponding particle mass distribution is shown in Fig. 6.

As described in the multi-lognormal fitting section, we performed the multi-lognormal fitting according to Hussein *et al.* (2005) by assuming three major modes: ultrafine, accumulation and coarse modes. The multi-lognormal fitting was also performed for the particle surface area and mass distributions as an additional control check on the fitting quality. With the particle size resolution, we can't assume more than two fine particle modes (i.e., ultrafine mode and accumulation mode). Usually, the ultrafine particles have two main modes: nucleation mode and Aitken mode.

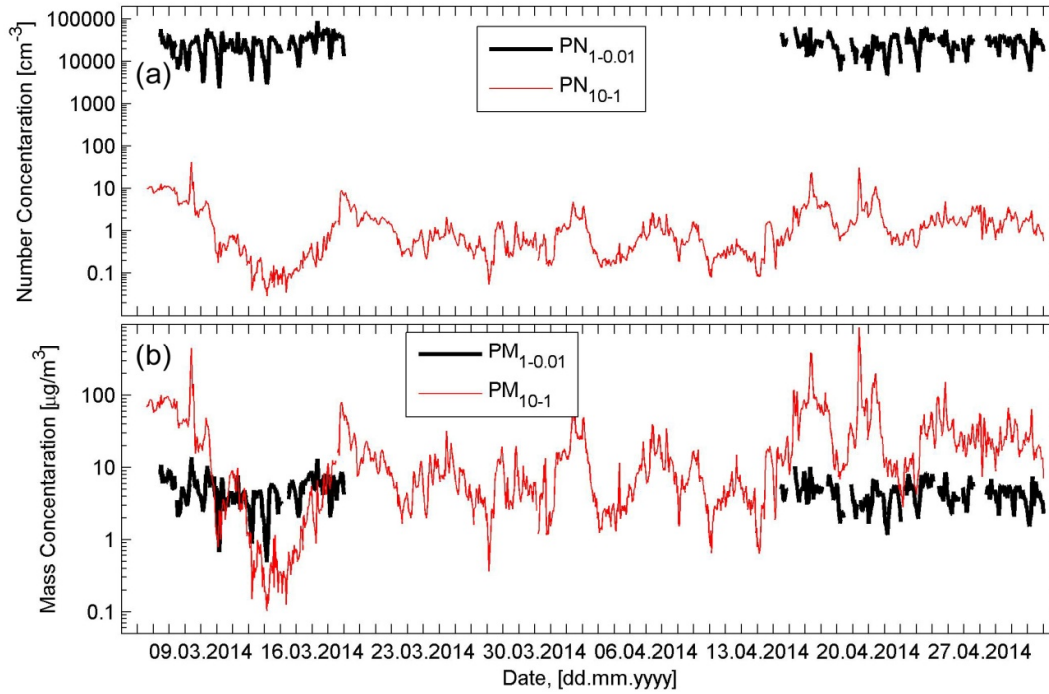


FIG. 4. Aerosol particle concentrations in two main fractions (submicron and coarse): (a) number concentrations and (b) mass concentrations.

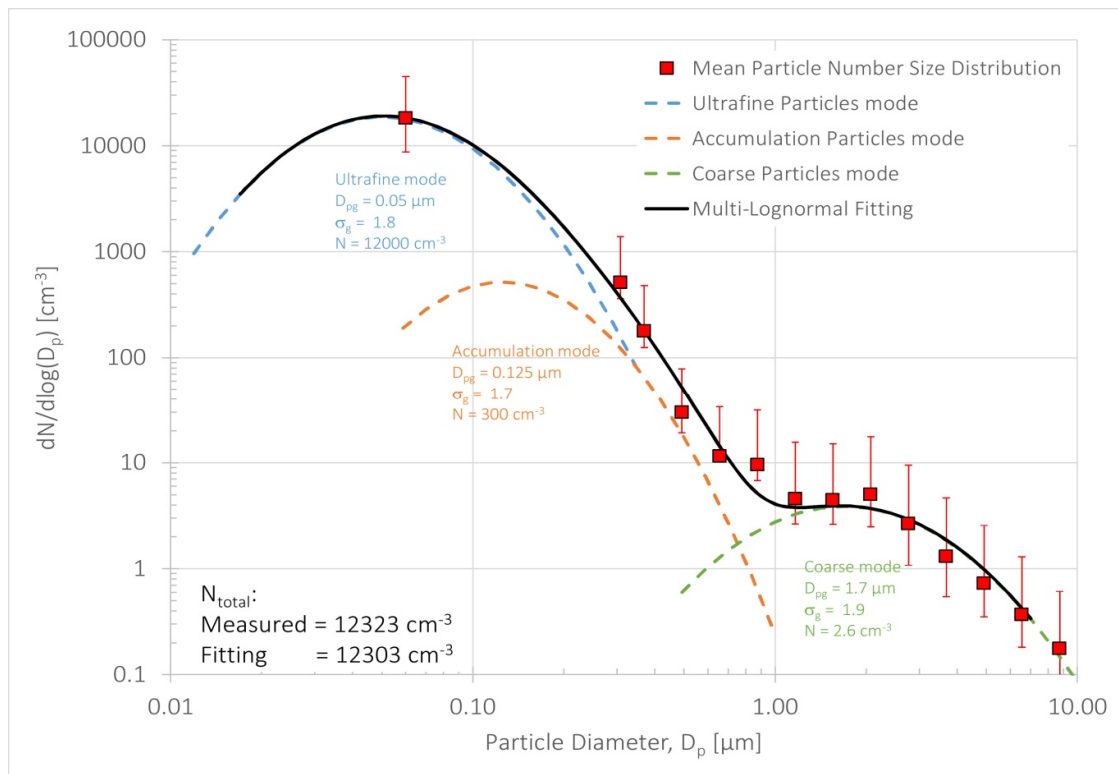


FIG. 5. Average particle number size distribution and its multi-lognormal fitting showing the modal structure. The particle number size distribution was obtained by merging the Optical Particle Counter (OPS) and the Condensation Particle Counter (CPC) data-sets.

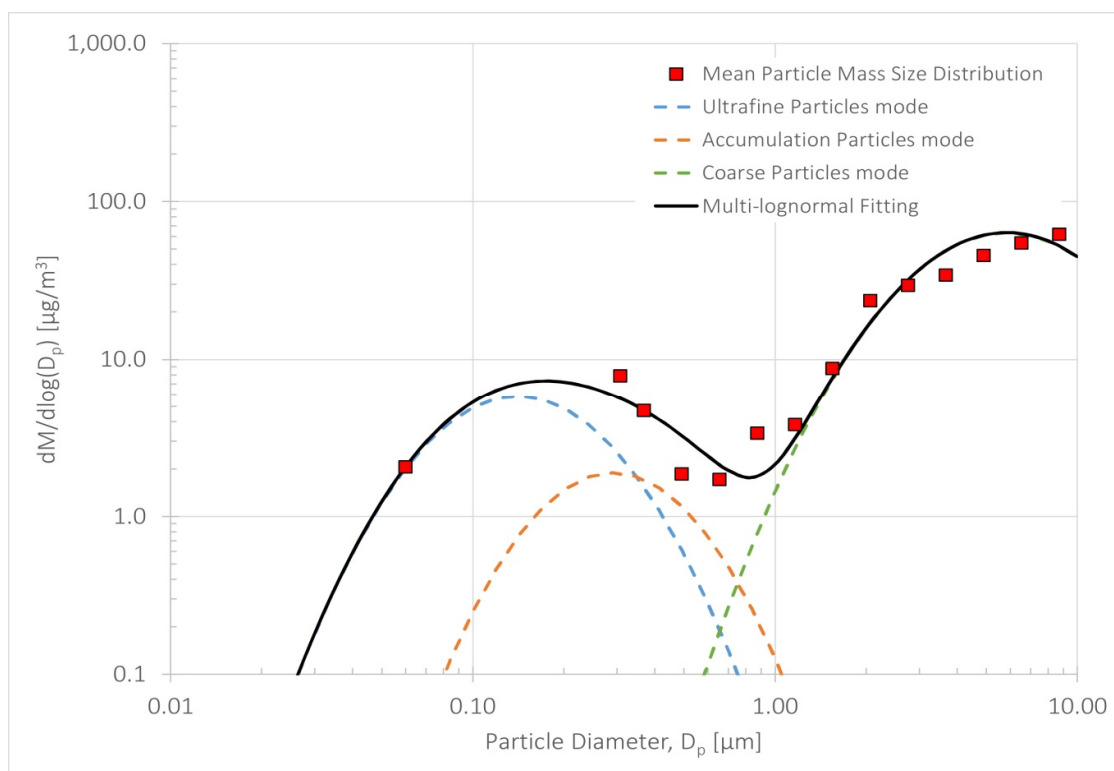


FIG. 6. Average particle mass distribution converted from the average particle number size distribution (Fig. 5) by assuming spherical particles with unit density.

According to the best multi-lognormal fitting, the mode geometric mean diameters (D_{pg}) were about 0.05 μm , 0.125 μm and 1.7 μm for the ultrafine mode, accumulation mode and coarse mode; respectively. The corresponding mode number concentrations were 12000 cm^{-3} , 300 cm^{-3} and 2.6 cm^{-3} . The difference in the total number concentration between the fitting and the measurement was very small (Fig. 5).

Conclusions

Most of the aerosol research in Jordan was focused on particulate matter concentration (PM), some gaseous pollutants and limited chemical analysis. In general, the aerosol research on particle number concentrations and particle size distributions has not been given enough attention in the Middle East and North Africa (MENA) region. Therefore, we defined the main objectives of this study to present the size-fractionated particle number and mass concentrations in Amman during the Spring season of 2014. We also presented, for the first time, the mean particle number size distribution by merging two aerosol data-sets: (1) submicron

particle number concentration and (2) particle number size distributions (diameter 0.3–10 μm).

In this study, we measured the particle number size distributions (optical diameter 0.3–10 μm) and utilized submicron particle number concentrations investigated in one of our previous studies (Hussein *et al.*, 2015). We calculated the size-fractionated particle number concentrations in two main ranges: submicron (diameter 0.01–1 μm) and coarse (diameter 1–10 μm). We also derived the particle number size distributions by merging the measured size distribution data-set (0.3–10 μm) with the submicron particle concentration data-set. We also calculated the corresponding particle mass size distribution by assuming spherical particles with unit density. This also enabled us to obtain the size-fractionated mass concentrations in the above-mentioned particle diameter ranges (i.e., submicron and coarse).

The overall mean particle number concentration of coarse particles (PN_{10-1}) was $1.8 \pm 2.9 \text{ cm}^{-3}$ with a median value $\sim 0.9 \text{ cm}^{-3}$ and a maximum as high as 41.3 cm^{-3} . The corresponding mean mass concentration (PM_{10-1}) was $22.1 \pm 44.3 \text{ µg/m}^3$ (median $\sim 9.7 \text{ µg/m}^3$ and

maximum 903.9 $\mu\text{g}/\text{m}^3$). The overall mean submicron particle number concentration ($PN_{1-0.01}$) was $26800 \pm 12800 \text{ cm}^{-3}$ with a median value $\sim 26100 \text{ cm}^{-3}$ and a maximum as high as 89500 cm^{-3} . The corresponding mean particle mass concentration ($PM_{1-0.01}$) was $4.7 \pm 1.9 \mu\text{g}/\text{m}^3$ (median $\sim 4.6 \mu\text{g}/\text{m}^3$ and maximum $13.9 \mu\text{g}/\text{m}^3$).

We also calculated the PM_{10} concentrations. Based on the hourly average, the PM_{10} concentrations were $0.6\text{--}465.5 \mu\text{g}/\text{m}^3$ (average $36.2 \pm 46.5 \mu\text{g}/\text{m}^3$ and median $22.6 \mu\text{g}/\text{m}^3$). The 24-hour PM_{10} concentrations were $3.7\text{--}126.4 \mu\text{g}/\text{m}^3$. According to the Jordanian concentrations limit value 24-hour PM_{10} ($120 \mu\text{g}/\text{m}^3$), there was only one exceedance that was observed on April 16th.

The mean particle number size distribution in the diameter range $0.01\text{--}10 \mu\text{m}$ was characterized by three main lognormal modes: ultrafine, accumulation and coarse modes. The geometric mean diameters (D_{pg}) were $0.05 \mu\text{m}$, $0.125 \mu\text{m}$ and $1.7 \mu\text{m}$, respectively for the ultrafine mode, accumulation mode and coarse mode. The mode number concentrations were 12000 cm^{-3} , 300 cm^{-3} and 2.6 cm^{-3} ; respectively.

Acknowledgments

This study was supported by the Deanship of Academic Research (DAR, project number 1516) at the University of Jordan. We would like to thank the crew at the Jordan Meteorological Department for providing the local weather information at Amman Civil Airport.

References

- [1] Hussein, T., Mølgaard, B., Hannuniemi, H., Martikainen, J., Järvi, L., Wegner, T., Ripamonti, G., Weber, S., Vesala, T. and Hämeri, K., *Boreal Environ. Res.*, 19 (2014) 1.
- [2] Curtis, L., Rea, W., Smith-Willis, P., Fenyves, E. and Pan, Y., *Environ. Intern.*, 32 (2006) 815.
- [3] Peters, A., Wiclumann, H.E., Tuch, T., Heinrich, J. and Heyder, J., *Am. J. Resp. Crit. Care Med.*, 155 (1997) 1376.
- [4] Pope, C.A.III, Burnett, R.T., Thun, M.J., Calle, E.E., Krewski, D., Ito, K. and Thurnston, G.D., *Am. Med. Assoc.*, 287 (2002) 1132.
- [5] Samet, J., Rappold, A., Graff, D., Cascio, W., Berntsen, J., Huang, Y-C., Herbst, M., Bassett, M., Montilla I., Hazuch M., Bromberg, Ph. and Devlin, R., *Am. J. Resp. Crit. Care Med.*, 179 (2009) 1034.
- [6] Ahmed, A.A., *J. Aerosol Sci.*, 20 (1989) 1115.
- [7] Alam, K., Trautmann, T., Blaschke, T. and Subhan, F., *Remote Sens. Environ.*, 143 (2014) 216.
- [8] Alghamdi, M.A., Almazroui, M., Shamy, M., Redal, M.A., Alkhalaf, A.K., Hussein, M.A. and Khoder, M.I., *Aerosol Air Qual. Res.*, 15 (2015) 440.
- [9] Alghamdi, M.A., Khoder, M., Abdelmaksoud, A.S., Harrison, R.M., Hussein, T., Lihavainen, H., Al-Jeelani, H., Goknil, M.H., Shabbaj, I.I., Almeahadi, F.M., Hyvärinen, A.-P. and Hämeri, K., *Air Quality Atmos. Health*, 7 (2014) 467.
- [10] Alghamdi, M.A., Khoder, M., Harrison, R.M., Hyvärinen, A.-P., Hussein, T., Al-Jeelani, H., Abdelmaksoud, A.S., Goknil, M.H., Shabbaj, I.I., Almeahadi, F.M., Lihavainen, H. and Hämeri, K., *Atmos. Environ.*, 48 (2014) 0409.
- [11] Basha, G., Phanikumar, D.V., Kumar, K.N., Ouarda, T.B.M.J. and Marpu, P.R., *Remote Sen. Environ.*, 169 (2015) 404.
- [12] Boman, J., Shaltout, A.A., Abozied, A.M. and Hassan, S.K., *X-Ray Spectrometry*, 42 (2013) 276.
- [13] Bonazza, A., Sabbioni, C., Ghedini, N., Hermosin, B., Jurado, V., Gonzalez, J.M. and Saiz-Jimenez, C., *Environ. Sci. Technol.*, 41 (2007) 2378.
- [14] Dada, L., Mrad, R., Siffert, S. and Saliba, N.A., *J. Aerosol Sci.*, 66 (2013) 187.
- [15] Daher, N., Saliba, N.A., Shihadeh, A.I., Jaafar, M., Baalbaki, R. and Sioutas, C., *Atmos. Environ.*, 80 (2013) 96.

- [16] Daum, P.H., Al-Sunaid, A., Busness, K.M., Hales, J.M. and Mazurek, M., *J. Geophys. Res.*, 98 (1993) 16809.
- [17] Dobrzinsky, N., Krugly, E., Kliucininkas, L., Prasauskas, T., Kireitseu, M., Zerrath, A. and Martuzevicius, D., *Aerosol Air Qual. Res.*, 12 (2012) 1209.
- [18] El-Araby, E.H., Abd El-Wahab, M., Diab, H.M., El-Desouky, T.M. and Mohsen, M., *App. Rad. Isotopes*, 69 (2011) 1506.
- [19] El-Askary, H. and Kafatos, M., *Int. J. Remote Sens.*, 29 (2008) 7199.
- [20] El-Metwally, M. and Alfaro, A.C., *Atmos. Res.*, 132-133 (2013) 76.
- [21] Elminir, H.K., *Sci. Tot. Environ.*, 350 (2005) 225.
- [22] Engelbrecht, J.P. and Jayanty, R.K.M., *Aeolian Res.*, 9 (2013) 153.
- [23] Gherboudj, I. and Ghedira, H., *Int. J. Climatol.*, 34 (2014) 3321.
- [24] Habeebullah, T.M., *Environ. Asia*, 2 (2013) 11.
- [25] Hamad, A.H., Schauer, J.J., Heo, J. and Kadhimd, A.K.H., *Atmos. Res.*, 156 (2015) 80.
- [26] Hassan, S.K., El-Abssawy, A.A., Abd El-Maksoud, A.S., Abdou, M.H. and Khoder, M.I., *Aerosol Air Qual. Res.*, 13 (2013) 1552.
- [27] Herring, J.A., Ferek, R.J. and Hobbs, P.V., *J. Geophys. Res.*, 101 (1996) 14451.
- [28] Hindy, K.T. and Farag, S.A., *Environ. Pollut. B: Chem. Phys.*, 5 (1983) 247.
- [29] Hussein, T., Alghamdi, M.A., Khoder, M., Abd El-Maksoud, A.S., Al-Jeelani, H., Goknil, M.K., Shabbaj, I.I., Almeahadi, F.M., Hyvärinen, A., Lihavainen, H. and Hämeri, K., *Aerosol Air Qual. Res.*, 14 (2014) 1383.
- [30] Jaafar, M., Baalbaki, R., Mrad, R., Daher, N., Shihadeh, A., Sioutas, C. and Saliba, N.A., *Sci. Tot. Environ.*, 496 (2014) 75.
- [31] Khodeir, M., Shamy, M., Alghamdi, M., Zhong, M., Sun, H., Costa, M., Chen, L.-C. and Maciejczyk, P., *Atmos. Pollut. Res.*, 3 (2012) 331.
- [32] Kouyoumdjian, H. and Saliba, N.A., *Atmos. Chem. Phys.*, 6 (2006) 1865.
- [33] Lowenthal, D.H., Borys, R.D., Chow, J.C., Rogers, F. and Shaw, G.E., *J. Geophys. Res.*, 97 (1992) 14573.
- [34] Mahmoud, K.F., Alfaro, S.C., Favez, O., Abdel Wahab, M.M. and Sciare, J., *Atmos. Res.*, 89 (2008) 161.
- [35] Munir, S., Habeebullah, T.M., Seroji, A.R., Gabr, S.S., Mohammed, A.M.F. and Morsy, E.A., *Atmos. Environ.*, 77 (2013) 647.
- [36] Munir, S., Habeebullah, T.M., Seroji, A.R., Gabr, S.S., Mohammed, A.M.F., Abu Saud, W., Abdou, A.E.A. and Awad, A.H., *Aerosol Air Qual. Res.*, 13 (2013) 901.
- [37] Reid, J.S., Reid, E.A., Walker, A., Piketh, S., Cliff, S., Al Mandoos, A., Tsay, S.-C. and Eck, T.F., *J. Geophys. Res.*, 113 (2008) D14212.
- [38] Rudich, Y., *J. Geophysical Research*, 108(D15) (2003) 4478.
- [39] Rushdi, A.I., Al-Mutlaq, K.F., Al-Otaibi, M., El-Mubarak, A.H. and Simoneit, B.R.T., *Arab. J. Geosci.*, 6 (2013) 585.
- [40] Saeed, T.M., Al-Dashti, H. and Spyrou, C., *Atmos. Chem. Phys.*, 14 (2014) 3751.
- [41] Saliba, N.A., El Jam, F., El Tayar, G., Obeid, W. and Roumie, M., *Atmos. Res.*, 97 (2010) 106.
- [42] Saliba, N.A., Kouyoumdjian, H. and Roumie, M., *Atmos. Environ.*, 41 (2007) 6497.
- [43] Satheesh, S.K., Deepshikha, S. and Srinivasan, J., *Int. J. Remote Sens.*, 27 (2006) 1691.
- [44] Shaka', H. and Saliba, N.A., *Atmos. Environ.*, 38 (2004) 523.
- [45] Shaltout, A.A., Boman, J., Al-Malawi, D.-A.R. and Shehadeh, Z.F., *Aerosol. Air Qual. Res.*, 13 (2013) 1356.
- [46] Tazaki, K., Wakimoto, R., Minami, Y., Yamamoto, M., Miyata, K., Sato, K., Saji, I., Chaerun, S.K., Zhou, G., Morishita, T., Asada, R., Segawa, H., Imanishi, H., Kato, R., Otani, Y. and Watanabe, T., *Atmos. Environ.*, 38 (2004) 2091.
- [47] Waked, A., Afif, C., Brioude, J., Formenti, P., Chevaillier, S., El Haddad, I., Doussin, J.-F., Borbon, A. and Seigneur, C., *Aerosol Sci. Technol.*, 47 (2013) 1258.

- [48] Waked, A., Seigneur, C., Couvidat, F., Kim, Y., Sartelet, K., Afif, C., Borbon, A., Formenti, P. and Sauvage, S., *Atmos. Chem. Phys.*, 13 (2013) 5873.
- [49] Moustafa, M., Mohamed, A., Ahmed, A.-R. and Nazmy, H., *J. Adv. Res.*, 6 (2015) 827.
- [50] Tadros, M.T.Y., Madkour, M. and Elmetwally, M., *Renew. Energy*, 17 (1999) 339.
- [51] Engelbrecht, J.P., McDonald, E.V., Gillies, J.A., Jayanty, R.K.M., Casuccio, G. and Gertler, A.W., *Inhal. Toxicol.*, 21 (2009) 297.
- [52] Engelbrecht, J.P., McDonald, E.V., Gillies, J.A., Jayanty, R.K.M., Casuccio, G. and Gertler, A.W., *Inhal. Toxicol.*, 21 (2009) 327.
- [53] El-Askary, H., Farouk, R., Ichoku, C. and Kafatos, M., *Ann. Geophys.*, 27 (2009) 2869.
- [54] Abdeen, Z., Qasrawi, R., Heo, J., Wu, B., Shpund, J., Vanger, A., Sharf, G., Moise, T., Brenner, S., Nassar, K., Saleh, R., Al-Mahasneh, Q., Sarnat, J. and Schauer, J., *The Middle East Consortium for Aerosol Research Study* (2014) ID 878704.
- [55] Abu-Allaban, M., Hamasha, S. and Gertler, A., *J. Air Waste Manag. Assoc.*, 56 (2006) 1440.
- [56] Al-Momani, F., Daradkeh, A., Haj-Hussein, A., Yousef, Y., Jaradat, K. and Momani, K., *Atmos. Res.*, 73 (2005) 87.
- [57] Gharaibeh, A., El-Rjoob, A. and Harb, M., *Environ. Monit. Assess.*, 160 (2010) 425.
- [58] Hamasha, K. and Arnott, W., *Environ. Monit. Assess.*, 166 (2010) 485.
- [59] Roumie, M., Chiari, M., Srour, A., Sa'adeh, H., Reslan, A., Sultan, M., Ahmad, M., Calzolari, G., Nava, S., Zubaidi, Th., Rihawi, S., Hussein, T., Arafah, D.-E., Karydas, A. G., Simon, A. and Nsouli, *Nuclear Instrum. Methods, Phys. Res. B*, 371 (2016) 381.
- [60] Schneidmesser, E., Zhou, J., Stone, E., Schauer, J., Qasrawi, R., Abdeen, Z., Shapund, J., Vanger, A., Shraf, G., Moise, T., Brenner, S., Nassar, K., Al-Mahasneh, Q. and Sarnat, J., *Atmos. Environ.*, 44 (2010) 3669.
- [61] Soleiman, A., Abu-Allaban, M., Bornstein, B., Luria, M. and Gertler, A., 11th Conference on Atmospheric Chemistry (2009).
- [62] Hussein, T., Abu Al-Ruz, R., Petaja, T., Junninen, H., Arafah, D., Hämeri, K. and Kulmala, M., *Aerosol Air Qual. Res.*, 11 (2011) 109.
- [63] Hussein, T., Halayka, M., Abu Al-Ruz, R., Abdullah, H., Mølgaard, B. and Petäjä, T., *Jordan J. Phys.*, 9 (2016) 31.
- [64] Hussein, T., Dal Maso, M., Petäjä, T., Koponen, I. K., Paatero, P., Aalto, P. P., Hämeri, K. and Kulmala, M., *Boreal Environ. Res.*, 10 (2005) 337.
- [65] Whitby, K. H., *Atmos. Environ.*, 12 (1978) 135.
- [66] Hussein, T., Puustinen, A., Aalto, P. P., Mäkelä, J. M., Hämeri, K. and Kulmala, M., *Atmos. Chem. Phys.*, 4 (2004) 391.

Authors Index

A. A. Ahmad.....	33
A. A. Bani-Salameh.....	33
A. AlTaani.....	1
A. Betar.....	49
A. Bitar.....	1
A. H. Ahmed.....	23
A. I. Samad.....	23
A. M. Alsaad.....	33
A. Maougal.....	11
H. Berrehal.....	11
H. M. Al-Khateeb.....	33
M. A. Al-Naafa.....	33
M. Nahili.....	1
Q. M. Al-Bataineh.....	33
R. S. Ababneh.....	17
S. K. Ezzulddin.....	23
T. Hussein.....	49

Subject Index

$^{226}\text{Ra-Be}$	1
Al-B co-doped ZnO	33
Dip coating	33
Fat-water separation.....	17
Free breathing.....	17
Hazard indices	23
Homotopy perturbation method (HPM).....	11
MCNP5 code	1
Multi-lognormal fitting	49
NaI(Tl) detector	23
Nanostructures	33
Neutron irradiator	1
Nonlinear differential equation.....	11
Oil field	23
Optical properties.....	33
Particle distribution.....	49
Portable aerosol instruments.....	49
Radioactivity.....	23
Sol gel process	33
Stack-of-stars	17
Structural properties.....	33
Thermoluminescent dosimeter.....	1
Thin films	33
TrueFISP	17
ZnO	33

المراجع: يجب طباعة المراجع بأسطر مزدوجة ومرقمة حسب تسلسلها في النص. وتكتب المراجع في النص بين قوسين مربعين. ويتم اعتماد اختصارات الدوريات حسب نظام Wordlist of Scientific Reviewers.

الجدول: تعطى الجداول أرقاماً متسلسلة يشار إليها في النص. ويجب طباعة كل جدول على صفحة منفصلة مع عنوان فوق الجدول. أما الحواشي التفسيرية، التي يشار إليها بحرف فوقي، فتكتب أسفل الجدول.

الرسوم التوضيحية: يتم ترقيم الأشكال والرسومات والرسومات البيانية (المخططات) والصور، بصورة متسلسلة كما وردت في النص.

تقبل الرسوم التوضيحية المستخرجة من الحاسوب والصور الرقمية ذات النوعية الجيدة بالأبيض والأسود، على أن تكون أصيلة وليست نسخة عنها، وكل منها على ورقة منفصلة ومعرفة برقمها بالمقابل. ويجب تزويد المجلة بالرسومات بحجمها الأصلي بحيث لا تحتاج إلى معالجة لاحقة، وألا تقل الحروف عن الحجم 8 من نوع Times New Roman، وألا تقل سماكة الخطوط عن 0.5 وبكثافة متجانسة. ويجب إزالة جميع الألوان من الرسومات ما عدا تلك التي ستُنشر ملونة. وفي حالة إرسال الرسومات بصورة رقمية، يجب أن تتوافق مع متطلبات الحد الأدنى من التمايز (1200 dpi Resolution) لرسومات الأبيض والأسود الخطية، و 600 dpi للرسومات باللون الرمادي، و 300 dpi للرسومات الملونة. ويجب تخزين جميع ملفات الرسومات على شكل (jpg)، وأن ترسل الرسوم التوضيحية بالحجم الفعلي الذي سيظهر في المجلة. وسواء أرسل المخطوط بالبريد أو عن طريق الشبكة (Online)، يجب إرسال نسخة ورقية أصلية ذات نوعية جيدة للرسومات التوضيحية.

مواد إضافية: تشجع المجلة الباحثين على إرفاق جميع المواد الإضافية التي يمكن أن تسهل عملية التحكيم. وتشمل المواد الإضافية أي اشتقاقات رياضية مفصلة لا تظهر في المخطوط.

المخطوط المنقح (المعدل) والأقراص المدمجة: بعد قبول البحث للنشر وإجراء جميع التعديلات المطلوبة، فعلى الباحثين تقديم نسخة أصلية ونسخة أخرى مطابقة للأصلية مطبوعة بأسطر مزدوجة، وكذلك تقديم نسخة إلكترونية تحتوي على المخطوط كاملاً مكتوباً على Microsoft Word for Windows 2000 أو ما هو استجد منه. ويجب إرفاق الأشكال الأصلية مع المخطوط النهائي المعدل حتى لو تم تقديم الأشكال إلكترونياً. وتخزن جميع ملفات الرسومات على شكل (jpg)، وتقدم جميع الرسومات التوضيحية بالحجم الحقيقي الذي ستظهر به في المجلة. ويجب إرفاق قائمة ببرامج الحاسوب التي استعملت في كتابة النص، وأسماء الملفات على قرص مدمج، حيث يعلم القرص بالاسم الأخير للباحث، وبالرقم المرجعي للمخطوط والمراسلة، وعنوان المقالة، والتاريخ. ويحفظ في مغلف واقٍ.

حقوق الطبع

يُشكّل تقديم مخطوط البحث للمجلة اعترافاً صريحاً من الباحثين بأن مخطوط البحث لم يُنشر ولم يُقدّم للنشر لدى أي جهة أخرى كانت وبأي صيغة ورقية أو إلكترونية أو غيرها. ويشتترط على الباحثين ملء نموذج يُنصّ على نقل حقوق الطبع لتصبح ملكاً لجامعة البيروك قبل الموافقة على نشر المخطوط. ويقوم رئيس التحرير بتزويد الباحثين بإنموذج نقل حقوق الطبع مع النسخة المرسلة للتفتيح. كما ويُمنع إعادة إنتاج أي جزء من الأعمال المنشورة في المجلة من دون إذن خطي مُسبق من رئيس التحرير.

إخلاء المسؤولية

إن ما ورد في هذه المجلة يعبر عن آراء المؤلفين، ولا يعكس بالضرورة آراء هيئة التحرير أو الجامعة أو سياسة اللجنة العليا للبحث العلمي أو وزارة التعليم العالي والبحث العلمي. ولا يتحمل ناشر المجلة أي تبعات مادية أو معنوية أو مسؤوليات عن استعمال المعلومات المنشورة في المجلة أو سوء استعمالها.

الفهرسة: المجلة مفهرسة في:

1- Emerging Sources Citation Index (ESCI)



2-

معلومات عامة

المجلة الأردنية للفيزياء هي مجلة بحوث علمية عالمية متخصصة مُحكمة تصدر بدعم من صندوق دعم البحث العلمي، وزارة التعليم العالي والبحث العلمي، عمان، الأردن. وتقوم بنشر المجلة عمادة البحث العلمي والدراسات العليا في جامعة اليرموك، إربد، الأردن. وتُنشر البحوث العلمية الأصلية، إضافة إلى المراسلات القصيرة Short Communications، والملاحظات الفنية Technical Notes، والمقالات الخاصة Feature Articles، ومقالات المراجعة Review Articles، في مجالات الفيزياء النظرية والتجريبية، باللغتين العربية والإنجليزية.

تقديم مخطوط البحث

تقدم البحوث عن طريق إرسالها إلى البريد الإلكتروني : jjp@yu.edu.jo

تقديم المخطوطات إلكترونياً: اتبع التعليمات في موقع المجلة على الشبكة العنكبوتية.

ويجري تحكيم البحوث الأصلية والمراسلات القصيرة والملاحظات الفنية من جانب مُحكمين اثنين في الأقل من ذوي الاختصاص والخبرة. وتُشجّع المجلة الباحثين على اقتراح أسماء المحكمين. أما نشر المقالات الخاصة في المجالات الفيزيائية النشطة، فيتم بدعوة من هيئة التحرير، ويُشار إليها كذلك عند النشر. ويُطلب من كاتب المقال الخاص تقديم تقرير واضح يتسم بالدقة والإيجاز عن مجال البحث تمهيداً للمقال. وتُنشر المجلة أيضاً مقالات المراجعة في الحقول الفيزيائية النشطة سريعة التغير، وتُشجّع كاتبي مقالات المراجعة أو مُستكثبيها على إرسال مقترح من صفحتين إلى رئيس التحرير. ويُرفق مع البحث المكتوب باللغة العربية ملخص (Abstract) وكلمات دالة (Keywords) باللغة الإنجليزية.

ترتيب مخطوط البحث

يجب أن تتم طباعة مخطوط البحث بنظ 12 نوعه Times New Roman، وبسطر مزدوج، على وجه واحد من ورق A4 (21.6 × 27.9 سم) مع حواشي 3.71 سم، باستخدام معالج كلمات ميكروسوفت وورد 2000 أو ما استُجد منه. ويجري تنظيم أجزاء المخطوط وفق الترتيب التالي: صفحة العنوان، الملخص، رموز التصنيف (PACS)، المقدمة، طرق البحث، النتائج، المناقشة، الخلاصة، الشكر والعرفان، المراجع، الجداول، قائمة بدليل الأشكال والصور والإيضاحات، ثم الأشكال والصور والإيضاحات. وتُكتب العناوين الرئيسية بخط غامق، بينما تُكتب العناوين الفرعية بخط مانس.

صفحة العنوان: وتشمل عنوان المقالة، أسماء الباحثين الكاملة وعناوين العمل كاملة. ويكتب الباحث المسؤول عن المراسلات اسمه مشاراً إليه بنجمة، والبريد الإلكتروني الخاص به. ويجب أن يكون عنوان المقالة موجزاً وواضحاً ومعبراً عن فحوى (محتوى) المخطوط، وذلك لأهمية هذا العنوان لأغراض استرجاع المعلومات.

الملخص: المطلوب كتابة فقرة واحدة لا تزيد على مائتي كلمة، موضحة هدف البحث، والمنهج المتبع فيه والنتائج وأهم ما توصل إليه الباحثون.

الكلمات الدالة: يجب أن يلي الملخص قائمة من 4-6 كلمات دالة تعبر عن المحتوى الدقيق للمخطوط لأغراض الفهرسة.

PACS: يجب إرفاق الرموز التصنيفية، وهي متوافرة في الموقع <http://www.aip.org/pacs/pacs06/pacs06-toc.html>.

المقدمة: يجب أن توضّح الهدف من الدراسة وعلاقتها بالأعمال السابقة في المجال، لا أن تكون مراجعة مكثفة لما نشر (لا تزيد المقدمة عن صفحة ونصف الصفحة مطبوعة).

طرائق البحث (التجريبية / النظرية): يجب أن تكون هذه الطرائق موضحة بتفصيل كاف لإتاحة إعادة إجرائها بكفاءة، ولكن باختصار مناسب، حتى لا تكون تكراراً للطرائق المنشورة سابقاً.

النتائج: يستحسن عرض النتائج على صورة جداول وأشكال حيثما أمكن، مع شرح قليل في النص ومن دون مناقشة تفصيلية.

المناقشة: يجب أن تكون موجزة وتركز على تفسير النتائج.

الاستنتاج: يجب أن يكون وصفاً موجزاً لأهم ما توصلت إليه الدراسة ولا يزيد عن صفحة مطبوعة واحدة.

الشكر والعرفان: الشكر والإشارة إلى مصدر المنح والدعم المالي يكتبان في فقرة واحدة تسبق المراجع مباشرة.

Subscription Form

Jordan Journal of
PHYSICS

An International Peer-Reviewed Research Journal issued by the
Support of the Scientific Research Support Fund

Published by the Deanship of Research & Graduate Studies, Yarmouk University, Irbid, Jordan

Name: الأسم:
Specialty:..... التخصص:
Address: العنوان:
P.O. Box:..... صندوق البريد:
City & Postal Code: المدينة/الرمز البريدي:
Country: الدولة:
Phone: رقم الهاتف:
Fax No:..... رقم الفاكس:
E-mail:..... البريد الإلكتروني:
No. of Subscription: عدد الاشتراكات:
Method of Payment:..... طريقة الدفع:
Amount Enclosed:..... المبلغ المرفق:
Signature: التوقيع:

Cheques should be paid to Deanship of Research and Graduate Studies - Yarmouk University.

I would like to subscribe to the Journal
For

- One Year
 Two Years
 Three Years

One Year Subscription Rates

	Inside Jordan	Outside Jordan
Individuals	JD 8	€ 40
Students	JD 4	€ 20
Institutions	JD 12	€ 60

Correspondence

Subscriptions and Sales:

Prof. Ibrahim O. Abu Al-Jarayesh
Deanship of Research and Graduate Studies
Yarmouk University
Irbid – Jordan
Telephone: 00 962 2 711111 Ext. 2075
Fax No.: 00 962 2 7211121



جامعة اليرموك



المملكة الأردنية الهاشمية

المجلة الأردنية

للفيزياء

مجلة بحوث علمية عالمية متخصصة محكمة
تصدر بدعم من صندوق دعم البحث العلمي

المجلة الأردنية
للفيزياء
مجلة بحوث علمية عالمية محكمة

المجلد (10)، العدد (1)، نيسان 2017م / شعبان 1438هـ

المجلة الأردنية للفيزياء: مجلة علمية عالمية متخصصة محكمة تصدر بدعم من صندوق دعم البحث العلمي، وزارة التعليم العالي والبحث العلمي، الأردن، وتصدر عن عمادة البحث العلمي والدراسات العليا، جامعة اليرموك، إربد، الأردن.

رئيس التحرير:

ابراهيم عثمان أبو الجرايش
قسم الفيزياء، جامعة اليرموك، إربد، الأردن.
ijaraysh@yu.edu.jo

هيئة التحرير:

ضياء الدين محمود عرفة
رئيس جامعة آل البيت، المفرق، الأردن.
darafah@ju.edu.jo
نبيل يوسف أيوب
رئيس الجامعة الأمريكية في مادبا، مادبا، الأردن.
nabil.ayoub@gju.edu.jo
جميل محمود خليفة
قسم الفيزياء، الجامعة الأردنية، عمان، الأردن.
jkalifa@ju.edu.jo
سامي حسين محمود
قسم الفيزياء، الجامعة الأردنية، عمان، الأردن.
s.mahmood@ju.edu.jo
مروان سليمان موسى
قسم الفيزياء، جامعة مؤتة، الكرك، الأردن.
mmousa@mutah.edu.jo
أكرم عبد المجيد الروسان
قسم الفيزياء التطبيقية، جامعة العلوم والتكنولوجيا الأردنية، إربد، الأردن.
akram@just.edu.jo
محمد خالد الصغير
قسم الفيزياء، الجامعة الهاشمية، الزرقاء، الأردن.
msugh@hu.edu.jo

سكرتير التحرير: مجدي الشناق

ترسل البحوث إلى العنوان التالي:

الأستاذ الدكتور نهاد محمد طشطوش
رئيس تحرير المجلة الأردنية للفيزياء
عمادة البحث العلمي والدراسات العليا، جامعة اليرموك
إربد، الأردن

هاتف 00 962 2 7211111 فرعي 2075

E-mail: jzp@yu.edu.jo Website: <http://Journals.yu.edu.jo/jzp>